Hydrodynamic analysis of suspension feeding in recent and fossil crinoids

Dissertation

der Mathematisch-Naturwissenschaftlichen Fakultät

der Eberhard Karls Universität Tübingen

zur Erlangung des Grades eines

Doktors der Naturwissenschaften

(Dr. rer. nat.)

vorgelegt von

Dipl. Geol. Janina Friederike Dynowski

aus Siegen

Tübingen

2014

Tag der mündlichen Qualifikation:	24.02.2015
Dekan:	Prof. Dr. Wolfgang Rosenstiel
1. Berichterstatter:	Prof. Dr. James H. Nebelsick
2. Berichterstatter:	Prof. Dr. Oliver Betz

Danksagung

Mein besonderer Dank gilt meinen Betreuern Prof. Dr. James H. Nebelsick und PD Dr. Anita Roth-Nebelsick für die Vergabe und gemeinsame Entwicklung dieses spannenden Themas, und die sehr gute Betreuung während der Doktorarbeit, im Zuge derer mir sehr viel Raum und Freiheit für die Realisierung des Projektes gelassen wurde. Mein Dank gilt außerdem Prof. Dr. Oliver Betz für die Begutachtung der Dissertation und PD Dr. Dr. Wilfried Konrad für anregende Diskussionen und viele konstruktive Hinweise.

Weiterhin möchte ich Prof. Dr. Horst Bleckmann und Dr. Adrian Klein für die Kooperation und tatkräftige Unterstützung während und nach der Durchführung der PIV-Messungen im Strömungskanal des Instituts für Zoologie der Rheinischen Friedrich-Wilhelms-Universität Bonn danken. Besonderer Dank gilt auch Christiane Schott und Matthias Boller für die Hilfe beim Bau der Strömungskanalmodelle, sowie allen weiteren Kollegen am Staatlichen Museum für Naturkunde Stuttgart und der Arbeitsgruppe Invertebratenpaläontologie und Paläoklimatologie der Universität Tübingen.

Mein Dank gilt außerdem dem Team des ZDV Tübingen für die Unterstützung bei der Nutzung der HPC-Ressourcen der bwGRiD-Initiative und des bwUniClusters, der DFG und dem DAAD für die finanzielle Förderung dieses Forschungsprojektes, sowie der Paläontologischen Gesellschaft für die Würdigung meiner Arbeit durch die Auszeichnung mit dem „Zukunfspreis für junge Paläontologen/innen“ auf der Jahrestagung 2011 in Wien.

Für die unschätzbar wertvolle Unterstützung während der ganzen letzten Jahre möchte ich mich außerdem ganz besonders bedanken bei Marek Dynowski und Marília Kaphan Freitas de Campos, Jan-Peter Friedrich, Katja Nellmann, Franziska Göhringer, Maika Meisner und natürlich bei meinen Eltern Monika und Hans-Joachim Dynowski!

Kurzfassung

Gestielte Crinoiden leben heute, bis auf wenige Ausnahmen, nur noch in der Tiefsee. Sie weisen einen weit zurückreichenden Fossilbericht auf, mit den ersten sicheren Vertretern im Ordovizium. Während des Paläozoikums und Mesozoikums waren sie zeitweise sehr weit verbreitet und besiedelten ausgedehnte Areale in Flachwasserbereichen. Rezente Crinoiden gehören zu den passiven Filtrierern und biegen ihre Arme entgegen der Strömungsrichtung in eine charakteristische Filtrierposition, den parabolischen Filtrationsfächer. Zahlreiche fossile Formen unterscheiden sich morphologisch jedoch stark von den heutigen, so dass für diese Crinoiden andere Filtrierpositionen angenommen werden können.

In der vorliegenden Studie wurde die Umströmung handgefertigter Modelle der rezenten Crinoide *Hyocrinus* sp. und der fossilen Crinoide *Encrinus liliiformis* in einem Strömungskanal mittels Particle Image Velocimetry (PIV) gemessen. Parallel hierzu erfolgte die Analyse von 3D Modellen mithilfe von Computersimulationen unter Anwendung von Computational Fluid Dynamics (CFD). Die Resultate beider Methoden wurden miteinander verglichen, und CFD im Folgenden angewendet, um erweiterte Modelle zu untersuchen. Diese umfassen die komplexer aufgebaute rezente Crinoide *Neocrinus decorus*, ein Submodell eines Arms mit meheren Pinnulae und Ambulakralfüßchen, sowie verschiedene Strömungsbedingungen und Filtrierpositionen von *E. liliiformis*.

Die Resultate der Strömungsanalyse der rezenten Crinoiden, die den parabolischen Filtrationsfächer bilden, zeigten eine gerade Durchströmung der Arme und Pinnulae. Die Krone führt zu einer Verlangsamung des Wassers und der darin enthaltenen Nahrungspartikel, die so von den ausgestreckten Ambulakralfüßchen eingefangen werden können. Die Analyse des Submodelles ließ erkennen, dass sich hinter den Ambulakralfüßchen engbegrenzte Rezirkulationszonen ausbilden, die allerdings kaum Partikel transportieren.

Für die fossile Seelilie *E. liliiformis*, die ihre Arme wahrscheinlich nicht wie die heutigen Crinoiden biegen konnte, unterstützten die Untersuchungen eine andere Filtrierposition, bei der die Krone eine Tropfenform bildet. Bei einer aboralen Anströmung mit Geschwindigkeiten über 0.01 m/s führt diese Position zur Entstehung einer Rezirkulation des Wassers in die Krone. Die „Particle Tracking“-Simulationen ergaben, dass Nahrungspartikel so zur Filteroberfläche zurücktransportiert werden. Ein Öffnen der Arme verstärkt die rezirkulierende Strömung, das Fehlen dreier Armteile schwächt die Rezirkulation deutlich ab. Bei einer Anströmung aus lateraler oder oraler Richtung können die Partikel direkt aus der Strömung eingefangen werden. Die vorgestellte Filtrierposition von *E. liliiformis* erweist sich daher als funktionstüchtig unter sich ändernden Strömungsbedingungen, wie sie typischerweise in den Flachwasserhabitaten im Muschelkalk der Mitteltrias auftraten.

Abstract

Recent stalked crinoids live primarily in the deep sea. First representatives are known from the Ordovician, and were very abundant during several time intervals of the Palaeozoic and Mesozoic era. Living crinoids are passive suspension feeders and typically arrange their body in the so-called parabolic filtration fan, where the arms are bent backwards into the incoming flow. The fossil record provides representatives that differ significantly in their morphology from that of the living forms and were very abundant in shallow water habitats. For those crinoids, different feeding positions have to be assumed.

In the presented study, physical models of the recent *Hyocrinus* sp. and the fossil *Encrinus liliiformis* were studied in a recirculating flow tank using Particle Image Velocimetry (PIV) to investigate the flow patterns forming around the crowns. In addition, 3D models of the crinoids were analysed with computer simulations applying Computational Fluid Dynamics (CFD). PIV and CFD results were validated against each other, and CFD was then used to investigate additional models including the more complex recent crinoid *Neocrinus decorus*, a submodel of part of an arm with several pinnules and tube feet, as well as different flow conditions and feeding positions of *E. liliiformis*.

Results for the recent crinoids adopting the parabolic filtration fan showed straight flow of the water through the arms and pinnules. The crown induces a baffling effect such that nutritive particles are slowed down and can be caught by the extended tube feet. The submodel including the finer morphological structures leads to the development of local, small scale recirculation behind the tube feet, but almost no particles are transported back to the oral surface in this current.

For the fossil crinoid *E. liliiformis*, which was probably not able to bend its arms to such an extant as living crinoids, both PIV and CFD results supported a different filtering position, where the crown forms a tearshape. With an aboral inflow and velocities of more than 0.01 m/s, this feeding position results in a recirculation of water into the crown. Particle tracking simulations showed that nutritive particles are then transported onto the oral surface. An opening of the arms increases the strength of the recirculation current, whereas the absence of parts of three arms decreases the recirculation considerably. Inflow from the lateral as well as oral side enables direct catchment of plankton out of the water. The postulated feeding position of *E. liliiformis* thus worked effectively under varying flow conditions that typically occured in the shallow water habitats of the Middle Triassic Muschelkalk, which this crinoid inhabited.

Table of contents

List of figures

List of tables

List of symbols

A = cross sectional area

g = gravitational acceleration

l = characteristic length

μ = dynamic viscosity

ν = kinematic viscosity

p = pressure

p_{dyn} = dynamic pressure

p_{stat} = static pressure

Re = Reynolds number

ρ = fluid density

u = velocity component u, parallel to X axis

u_{recirc} = recirculation velocity

V = total velocity

V_{init} = inlet velocity

v = velocity component v, parallel to Z axis

w = velocity component w, parallel to Y axis

z = elevation above a reference plane

1 Introduction

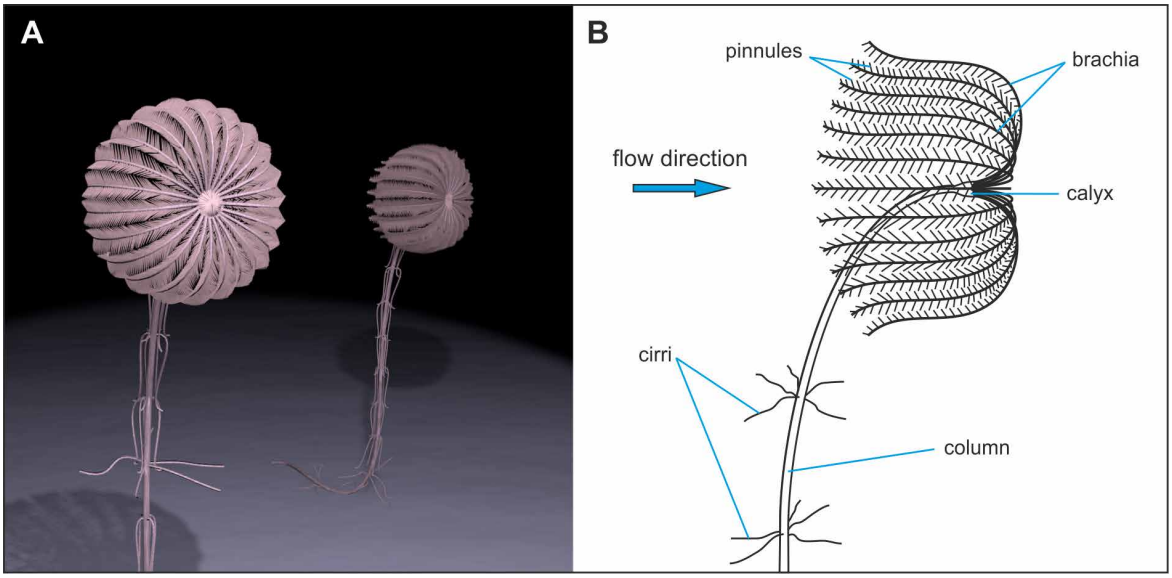

Figure 1: Example of a recent stalked crinoid. A: 3D reconstruction of a typical crinoid, forming the parabolic filtration fan for feeding with the arms bent backwards into the incoming flow (created with Blender); B: Schematic illustration of general morphologic features and flow direction while feeding.

Crinoids belong to the phylum Echinodermata, an animal group that today includes the echinoids (sea urchins), asteroids (sea stars), ophiuroids (brittle stars), crinoids (sea lilies and feather stars) and holothuroids (sea cucumbers). All classes share some very special characters including, besides others, a Mg-calcitic skeleton build up of numerous single ossicles, a typical microscopic structure of the skeleton called stereom, an ambulacral system for locomotion and feeding, and a primary pentameric body symmetry (Ziegler, 1998; Pawson, 2007). They are known since the early Palaeozoic and comprise very abundant and characteristic fossils throughout earth history. Because of the peculiar nature of the skeleton, most echinoderms have a relatively high preservation potential and often are found to form mass accumulations (e.g. Nebelsick and Kroh, 2002; Radwański, 2002; Meyer et al., 2002). A very special facies type are the so called encrinites, which are almost solely build up of crinoid ossicles and can reach thicknesses of several meters (Ausich, 1997). The Trochitenkalk of the Middle Triassic Upper Muschelkalk is one of these encrinites, where successions of up to 15 m are made up mostly of columnals (stem ossicles) of *Encrinus liliiformis*.

Within the class Crinoidea, generally two groups are differentiated: the sessile sea lilies, which possess a stalk to raise their crown above the sea floor, and the mobile feather stars, which lack a stalk (Breimer, 1978). Sea lilies today are restricted to deep sea habitats. They first occurred in the Ordovician (480 Ma ago), and were very diverse and abundant throughout the Palaeozoic and Mesozoic era, also populating shallow water habitats. In the course of the Mesozoic Marine Revolution, major evolutionary changes can be found in

marine communities, including the appearance of the mobile unstalked crinoids (Baumiller et al., 2010). Feather stars today live in a wide variety of environments, including shallow water as well as deep water settings. This group evolved during the Mesozoic era and shows a rapid radiation from the Jurassic onwards. Concurrent, sea lilies show decreasing general abundance and an increasing restriction to deep water environments. While shallow water feather stars are often easy to access and their life habits are relatively well known, knowledge on deep sea crinoids is sparse and mostly based on submersible observations, investigation of dredged material, theoretical considerations or transferred from their shallow water, unstalked relatives (e.g. Meyer, 1973; Macurda and Meyer, 1974; Conan et al., 1981; Roux, 1987). Baumiller et al. (1991) and Kitazawa and Oji (2010) provide some general observations of specimens that were successfully transferred to high pressure water tanks.

The body of a typical stalked crinoid (Fig.1) consists of the column (stem or stalk), which lifts the animal above the ground and either is attached to the substrate permanently, or bears whorls of root-like cirri to grasp objects for anchorage, and a crown comprising the calyx with the main body volume and the brachia (arms) for food collection and reproduction. The calyx consists of a characteristic set of plates, in most cases serving for systematic identification. The mouth and anus are located on the tegmen that covers the body cavity formed by the calyx. The arms can branch in various patterns, leading to different numbers of endings, ranging from 5 to more than 200 (Breimer, 1978). They are covered with numerous appendages, called pinnules, which are divided into the oral pinnules located near the mouth for food manipulation, the genital pinnules which bear the gonads, and the distal pinnules which bear triads of tube feet along a centrally extending food groove and serve for plankton collection (Lawrence, 1987; Heinzeller and Welsch, 1994). The tube feet are covered with small papillae that contain mucus glands and produce a secretion, to which the nutritive particles adhere. The triads of tube feet consist of a large sized primary, a medium sized secondary and a small sized tertiary tube foot, which transfer the captured plankton particles into the food groove, where the food is carried towards the mouth by ciliary movement.

Crinoids are passive suspension feeders thus relying solely on the movement of the surrounding water (Baumiller, 2008). Their main diet consists of miscellaneous diatoms, with diameters typically ranging between 20 und 150 micrometers (Kitazawa et al., 2007). Sea lilies show a characteristic feeding position with the arms bent into the incoming water flow, thus creating a simple but effective three-dimensional filter, the so called parabolic filtration fan (Macurda and Meyer, 1974). This posture, where the concave opening of the filter apparatus faces the current directly, is interpreted to act as a baffle, leading to a decelaration of the flow and the contained nutritive particles which can then be caught by the extended tube feet (Welch, 1978; Meyer, 1982). It was also proposed that small scale turbulent currents

form behind the crown, increasing the drag of the crinoid (Roux, 1987).

The parabolic filtration fan is confined to special flow conditions, including unidirectional flow with approximate velocities ranging between 0.01 m/s and 0.25 m/s (Macurda and Meyer, 1974; Conan et al., 1981, Jørgensen, 1983). Below 0.01 m/s, it is assumed that an insufficient number of particles would reach the sticky surface of the tube feet to compensate the energy needed for catching them (Jørgensen, 1983; Baumiller, 1993). In slack currents, crinoids show a typical upright position with the oral surface facing upwards, resembling a wilted flower (Macurda and Meyer, 1974; Messing, 1985; Baumiller et al., 1991). In high flow velocities, crinoids close their arms and form a tear shape, the so called survival posture (Haugh, 1978; Roux, 1987). This shape decreases drag forces acting on the animal, and thus the strain on the stalk, which reduces the risk of being detached from the ocean floor.

In order to understand the flow field developing around crinoids, some basic mechanisms of fluid dynamics have to be considered. In general, an object, for example a circular cylinder (Fig. 2), that is exposed to a moving fluid affects the flow field upstream as well as downstream (the wake) of the object. According to the principle of continuity, the same volume of fluid, that enters a domain, has to leave this domain, in the same time interval (Vogel, 1996; Hucho, 2011). The principle of continuity can be expressed as:

$$A_1 V_1 = A_2 V_2 \tag{1}$$

with A = cross sectional area and V = velocity. From equation 1 it can be concluded that a change in cross sectional area is concurrent with a change in velocity, thus a decrease in A leads to an increase in V while an increase in A causes a decrease in V. Applied to the example of the cylinder, this means that the object itself decreases the cross sectional area of the fluid so that the velocity is increased when the fluid passes the cylinder. Velocity is a vector quantity, possessing a magnitude and a direction (Anderson, 2011). In a three-dimensional cartesian coordinate system, this vector can be divided into three components u, v and w, running parallel along the principal axes (Fig. 2A) with the relation:

$$V = \sqrt{u^2 + v^2 + w^2} \tag{2}$$

In the example of the cylinder, velocity component u is parallel to the inflow of the water and called the axial velocity. Negative values of u indicate a backflow of water, thus the recirculation velocity is herein defined as the minimum reached negative value of u, denominated u_{recirc}. At the inlet of the domain, the initial velocity V_{init} is specified, with V = 0.3 m/s and the direction 1/0/0 (parallel to the X axis) such that here only velocity component u

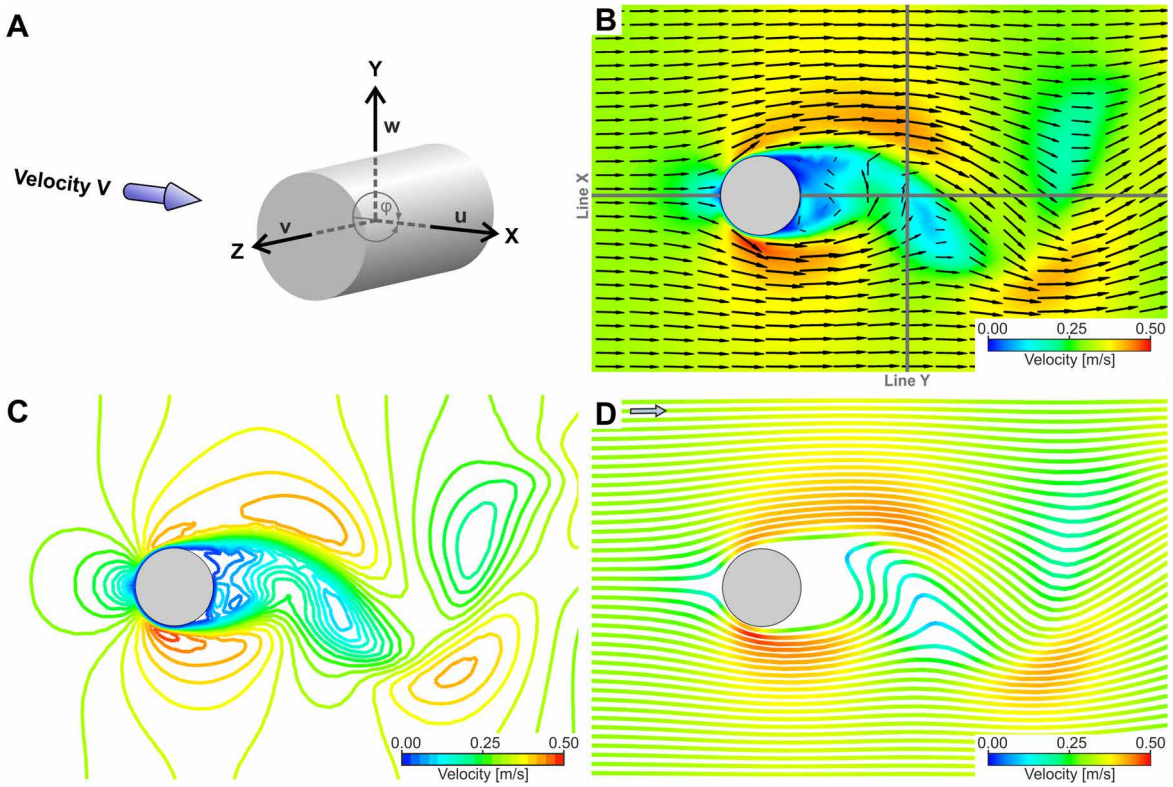

Figure 2: Flow field of a circular cylinder at Re = 277. A: general setup with flow direction and coordinate system in perspective view; B: combined contour-vector plot on XY plane with tangential projection of the vectors; C: contour plot on XY plane; D: streamline plot in sideview.

contributes to the flow, while v = 0 m/s and w = 0 m/s. The cylinder itself is defined as a so called “no slip wall”, which implies that the water has zero velocity at the surface of the object. Starting at the wall with V = 0 m/s, the freestream velocity is reached at a characteristic distance, presenting a peculiar zone that is described as the boundary layer (Schlichting and Gersten, 1997).

For the visualisation of the general flow pattern, several graphical tools exist (Fig. 2B-D). The terms upper/lower (above/below) used in the following are related to the local coordinate system and orientation of the shown example, but in other setups could as well be replaced by left and right or other positional terms. In Figure 2B, the flow field is depicted as a combined contour-vector plot. The black vectors display the direction of the flow, as well as the velocity magnitude, which is indicated by the length of the arrows. The vectors are superimposed on a coloured contour plot, where the colours indicate the values of the total velocity in m/s. In the presented cylinder example, red colours represent an increase in velocity (on the upper and lower surface of the cylinder, due to the decrease in cross sectional area), and blue colours (behind the cylinder) a decrease in relation to the inflow velocity. Figure 2C displays the total velocity as coloured contour lines, connecting points of equal velocity. In Figure 2D, the flow field is illustrated as a coloured streamline plot. A streamline is defined as a line which is tangential to the local flow direction in every point thus illustrating the path a

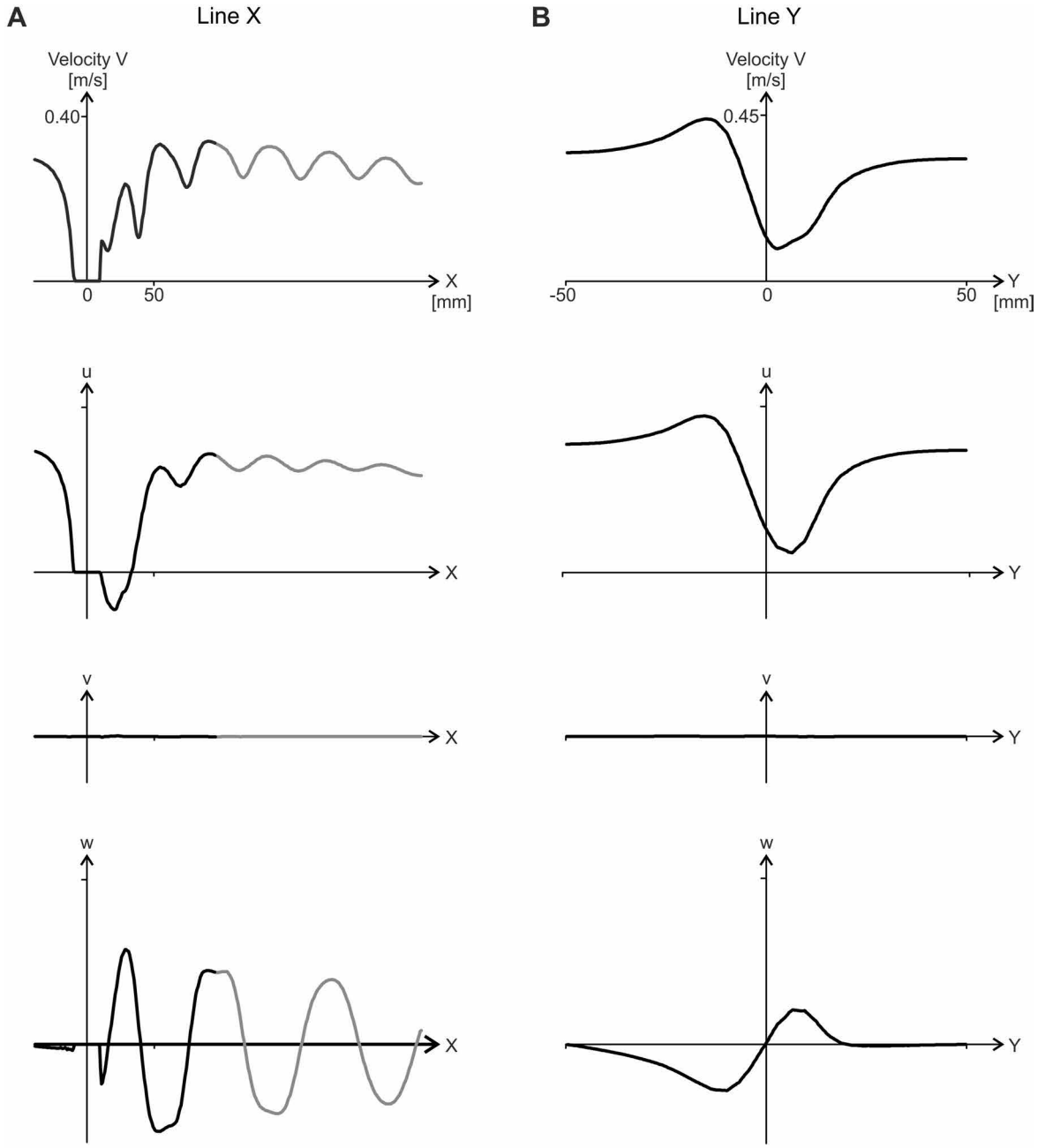

Figure 3: Line graph plots of total velocity and individual velocity components along lines indicated in Fig. 2B (black parts corresponding to section displayed in Fig. 2B). A: Line X; B: Line Y.

fluid element would follow in the given flow field (Vogel, 1996; Anderson, 2011). Accordingly, particle trajectories or pathlines describe the path injected particles would travel, which differ from fluid parcels due to density differences and particle diameters. Converging lines in a streamline plot indicate an increase in velocity (relative to the inflow velocity), diverging lines a decrease in velocity.

For a more detailed analysis of the flow field, the individual velocity values can be plotted as line graphs along specified locations (Fig. 3). In Figure 2B, two lines are depicted, one along the X axis, one along the Y axis (30 mm behind the end of the cylinder in its wake).

At these lines, the total velocity V and the three components u, v and w were extracted and plotted against the X (Fig. 3A), respectively Y coordinates (Fig. 3B). At line X, V decreases in front of the cylinder and takes a value of V = 0 m/s at the object itself. Behind the cylinder, V increases showing an oscillating pattern. Velocity component u reaches negative values behind the cylinder, indicating recirculation of the flow, followed by an increase in u with similar but weaker fluctuations as in V. Velocity component v, in contrast, does not deviate much from the initial value of v = 0 m/s defined at the inlet, which in this case is a result of the simulation setup, where the Z dimension of the geometry is very limited almost representing a 2D case. Velocity component w, again shows considerable oscillations in the wake of the cylinder, indicating a motion of the water along the Y axis (in this example representing an upward and downward movement). At Line Y, two peaks are recognizable, one reaching V = 0.44 m/s, representing an increase in velocity in relation to V_{init} of 47 %, the other peak with a minimum value of V = 0.09 m/s, representing a decrease of 71 % in relation to V_{init}. Velocity component u shows an almost similar curve progression, component v again does not vary, and component w likewise reaches two peaks at the same Y positions as V and u, with values of w = -0.13 m/s and w = 0.09 m/s.

The conspicuous flow pattern apparent in the presented example of the cylinder is a consequence of alternating vortices forming behind the cylinder, the so called Kármán vortex street. This typical flow field occurs only in a special flow regime, which can be characterized by the dimensionless Reynolds number Re:

$$\mathrm{Re} = \frac{\rho \mathrm{l} \mathrm{V}}{\mu} = \frac{\mathrm{l} \mathrm{V}}{\nu} \tag{3}$$

with l = characteristic length, μ = dynamic viscosity, and ν = kinematic viscosity. Re describes a ratio of the inertial forces to the viscous forces and can be used to define the flow type as being either laminar or turbulent (Vogel, 1996).

Furthermore, for a given shape, equal values of Re mean similar physical character of the flow. The consequence of this relationship is that objects can be resized, e.g. for wind tunnel experiments, as long as velocity or viscosity are changed accordingly to keep Re equivalent. Experimental setups can thus be simplified by scaling down objects and obtaining the same flow results as for the original sized ones, by increasing the flow velocity. For the case of the flow around the circular cylinder, various ranges of Re can be distinguished, where typical flow phenomena occur. In a range of Re = 40...100 000, the shape of the cylinder leads to the characteristic shedding of alternating vortices. In the presented example of Figure 2, Re = 277, and the velocity distribution depicted in Figure 3 with regular fluctuations along the X axis and two peaks at line Y is a result of vortex shedding. Since this is a time dependant

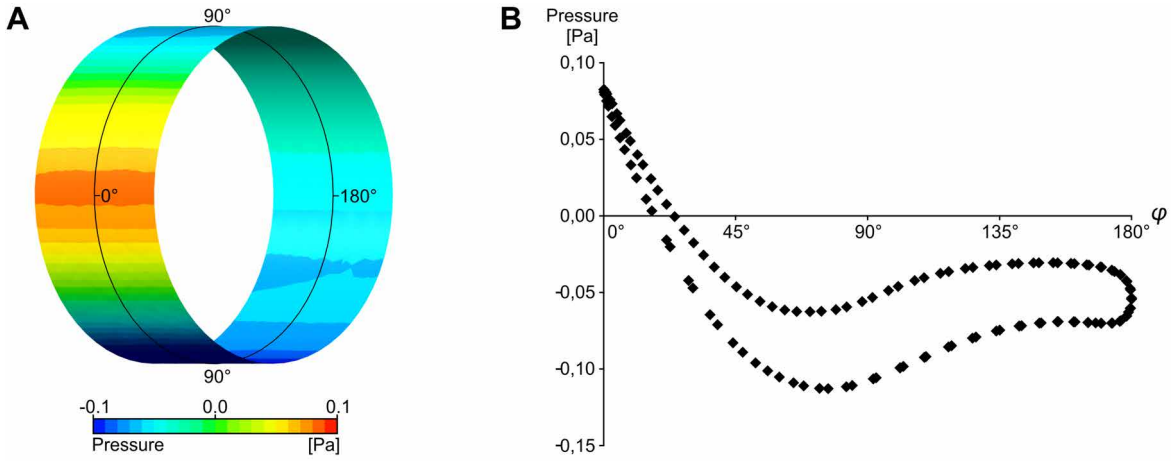

Figure 4: Pressure distribution on the cylinder surface (section of Fig. 2A). A: contour plot in perspective view; B: line graph plot of p_{stat} plotted against φ (position indicated by black line in A).

case, a transient solution is necessary in order to resolve the flow behaviour over a defined time period. The plots shown in Figures 2 and 3 are snap-shots of one time step.

In addition to the velocity field, the pressure distribution is of high importance for many biological as well as technical applications. The combination of the principle of continuity (equation 1, p. 3), with Bernoulli's principle for frictionless flow:

$$p + \rho g z + \frac{\rho V^2}{2} = \text{const.} \tag{4}$$

with p = pressure of the fluid, ρ = fluid density, g = gravitational acceleration, and z = elevation above a reference plane, enables the reconstruction of the pressure distribution: an increase in V results in a decrease in p (as long as z and ρ stay constant). This relation is valid only for frictionless or inviscid flow, implying that viscous forces are small and inertial forces the main contributor, such that friction is negligible (for further explanation see Schlichting and Gersten, 1997; Spurk and Aksel, 2007; Zierep and Bühler, 2010; Anderson, 2011). This is only true for flow regions with small velocity gradients, where no flow separation occurs, and thus can not be transferred to the region behind the cylinder, where the flow separates on the lower and upper surface of the cylinder (Hucho, 2011).

Pressure in moving fluids is composed of two components: static pressure p_{stat}, which is related to water depth and can only be determined experimentally respectively computationally, and dynamic pressure, p_{dyn}, which is related to fluid velocity and can be calculated as:

$$p_{dyn} = \frac{1}{2}\rho V^2 \tag{5}$$

Figure 4 illustrates the static pressure distribution on the cylinder surface shown in Figure 2A along a line following the whole circumference, where the angle φ specifies the spatial

coordinate (cf. Fig. 2A). The highest pressure values occur at the stagnation point on the front side at $\varphi = 0°$ (maximum of p_{stat} = 0.08 Pa), while negative pressure values can be found on the lower surface (minimum of p_{stat} = -0.11 Pa), and the upper surface (minimum of p_{stat} = -0.06 Pa), where the vortices detach, and on the back side of the cylinder (at $\varphi = 180°$ p_{stat} = -0.05 Pa). Plotting the static pressure against angle φ reveals that both vortices separate from the cylinder slightly ahead of the maximum diameter at $\varphi = 90°$, which is a consequence of the low Re range of the presented example (subcritical flow, see Hucho, 2011).

Understanding the pressure distribution of a fluid dynamic problem enables the investigation of the developing lift and drag forces that a body exposed to a moving fluid encounters. While lift is mainly created by a pressure difference below and above the body and largely dependant on the angle of attack, drag is a function of the pressure difference in front and behind the body in question (Hucho, 2011). Because the cylinder is a symmetric object, the pressure difference between the upper and lower surface and thus the lift is zero in a steady flow. In the presented example, however, the alternating vortices produce alternating pressure values on the lower and upper surfaces, resulting in alternating upward and downward facing lift forces, which would, in a non-fixed cylinder, produce an upward-downward movement of the object. This effect is called vortex induced vibration and is of interest in a wide range of engineering applications (Williamson and Govardhan, 2004). The drag of the cylinder is generally high, which is due to its bluff body shape that creates a wide and turbulent wake with high pressure differences in front of and behind the object.

In the presented study, the hydrodynamics of feeding in recent and fossil crinoids are analysed, for the first time applying Particle Image Velocimetry (PIV), a laseroptical experimental method, and Computational Fluid Dynamics (CFD), a numerical simulation method. The crinoids serving as models include two recent stalked crinoids, both adopting the characteristic parabolic filtration fan for feeding: the five-armed *Hyocrinus* sp., and the multi-armed *Neocrinus decorus* (in the presented study possessing a total of 20 arm endings); one recent unstalked feather star *Oxycomanthus bennetti* serving as orientation for a tube feet submodel; and one fossil stalked crinoid: *Encrinus liliiformis* that lived during the middle Triassic Muschelkalk (243–235 Ma) and had 10 relatively short and stiff arms and probably was not as flexible as to form the parabolic filtration fan. For this crinoid, a feeding position without a backward bending of the arms is supposed and analysed under varying flow conditions. *E. liliiformis* was reconstructed as an active suspension feeder by Jefferies (1989), a feeding strategy not known from recent crinoids. From the results of the presented study, however, it is concluded that a feeding position, where the crown forms a tear shape, was sufficient for the crinoid to use passive suspension feeding as the main strategy.

2 Motivation

Filter mechanisms of all kinds are of high interest to scientists in different fields of research. Scientific studies of filtering processes include a large range of feeding strategies of many living and fossil organisms as well as different technical applications. Since filter feeding is widely utilized in aquatic organisms, it is of high ecological relevance and thus very important to understand the biology of organims and their interrelationships within ecosystems (LaBarbera, 1984; Vogel, 1996; Riisgard and Larsen, 2010).

Crinoids today are typical animals of deep water settings and have a long and extensive fossil record, often being preserved in shallow water sediments. Due to their remote habitat in the deep sea, living stalked crinoids are difficult to study in their natural environment. Keeping them in high pressure water tanks is very costly and even then experiments under controlled conditions are difficult to realize. The knowledge on the feeding behaviour of fossil sea lilies is even scarcer due to the lack of three-dimensionally specimens preserved in their feeding position. Many reconstructions thus are based on their living counterparts. Because, however, the parabolic filtration fan seems to be adapted to the constant flow conditions of the deep sea, it is unclear how this shape could have functioned effectively in shallow water settings typical for many facies in which various fossil crinoids are found. In addition, the fossil record provides numerous sea lilies with differing morphology that were not able to adopt the parabolic filtration fan, and probably showed a different feeding position.

The presented study applies modern flow tank experiments and computer simulations to investigate the feeding habits of extant and extinct crinoids and includes the following objectives:

1. Evaluate the potential of flow tank experiments and computer simulations to investigate biological filter systems;
2. Provide insights into the hydrodynamics of living stalked crinoids and expand our knowledge of passive suspension feeding in the deep sea;
3. Draw conclusions regarding feeding strategies of fossil crinoids and reconstruct palaeoenvironments.

In addition, biological filter strategies are expected to contribute biomimetic concepts to technical filtering systems. The feeding apparatus of typical crinoids represents a complex three-dimensional passive filter, which is build up of simple elements and very effective in catching plankton particles out of the water. The presented study is thus a first attempt to evaluate crinoid feeding in order to find new concepts which might be interesting for further systematic studies to be transferred to biomimetically inspired industrial grade filters.

3 Materials and methods

3.1 Model crinoids

The presented study investigates the flow around four different crinoid inspired morphologies. As models, the following stalked crinoids were chosen: the five-armed *Hyocrinus* sp. (THOMSON, 1876), a recent crinoid with a relatively simple crown morphology (Fig. 5A); the multi-armed *Neocrinus decorus* (THOMSON, 1864), a living crinoid with a more complex branching pattern (Fig. 5B); and *Encrinus liliiformis* (LAMARCK, 1801) from the Middle Triassic Muschelkalk, with ten stout arms that were probably not flexible enough to form a parabolic filtration fan (Fig. 5C). In order to evaluate the small scale flow around the tube feet, an additional computer model of part of an arm was created, based in parts on the unstalked feather star *Oxycomanthus bennetti* (MÜLLER, 1841). Figure 5D illustrates a close up of an exemplary single crinoid arm including the primary tube feet.

Hyocrinus sp. was chosen because of its relatively simple filter architecture, which is suitable for resin model creation for flow tank experiments. It has five unbranching arms and lives in the deep sea attached permanently to the sea floor by a cementing hold fast. The second recent crinoid, *N. decorus*, represents a sea lily with 10 primary arms that typically bifurcate, in the analysed model one time, thus resulting in a total of 20 arm endings. It is not fixed permanently to the sea floor, but has root cirri on the stalk with which it can actively anchor itself to the substrate. This enables a change of its location as a reaction to disturbance or unfavourable flow conditions, as was observed for other crinoids (Baumiller and Messing, 2007). This more complicated morphology was only realized as a 3D computer model to analyse the water flow around a branching crinoid filter architecture.

For the flow analysis around the smaller structures, a submodel was created, including part of an arm with several pinnules, covered by primary tube feet. The dimensions of the CFD model are based, in parts, on morphological data of the comatulid *O. bennetti* (*Comanthus bennetti* in Meyer, 1979), where the mean spacing of the tube feet is given as 7.26 per mm, with a length of 0.56 mm and a width of 50 µm. Due to meshing restrictions, the computer model was realized with a tube feet spacing of 7.2 per mm, a length of 0.56 mm and width of 100 µm. Following the photographic images published by Meyer (1979), the tube feet are not kept in a straight but rather a slightly bent postion, so that the tube feet of the computer model were rotated by an angle of 30° to imitate a more natural posture.

The extinct crinoid *E. liliiformis* lived during the Anisian to lower Carnian in Central Europe (Hess, 2011). It had 10 short, biserial arms, a low bowl shaped calyx and a long stem consisting of cylindrical columnals. Jefferies (1989) reconstructed *E. liliiformis* as an active filter feeder, based on the occurrence of distinct grooves on the pinnular plates. In contrast

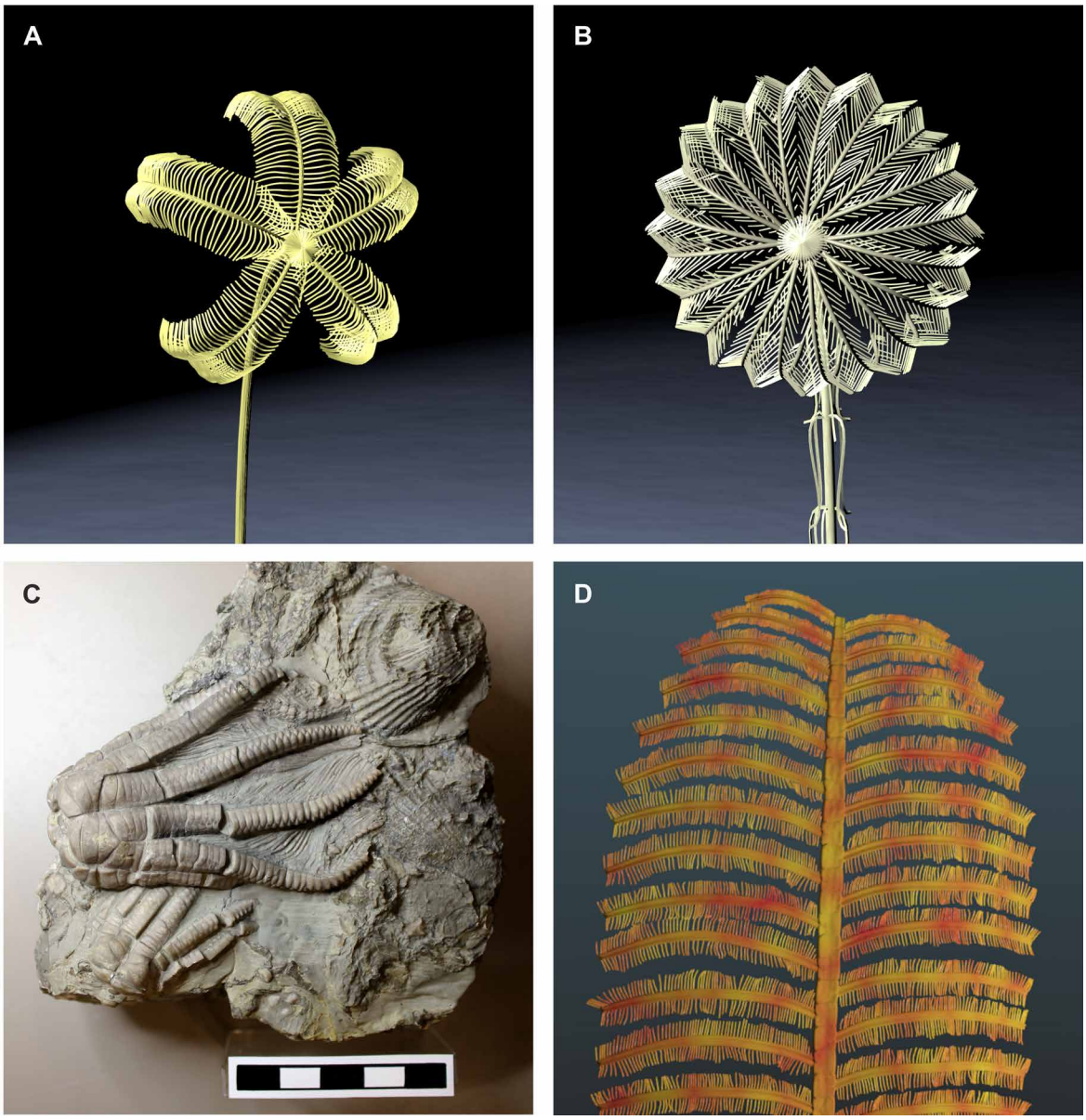

Figure 5: Model crinoids. A: 3D reconstruction of the five-armed *Hyocrinus* sp.; B: 3D reconstruction of a 20-armed *Neocrinus decorus*; C: crown of *Encrinus liliiformis* in typical preservation position with the arms opened to a relatively small degree (SMNS21859); D: 3D reconstruction of a close up of one crinoid arm with pinnules and primary tube feet. 3D models created with Blender.

to today's sea lilies, this crinoid possessed only a low number of muscular articulations in its crown, occurring between the radial plate of the cup and the first arm plate, the second and third arm plate and the articulations of the first pinnular plate to the corresponding arm plate (Jefferies, 1989). Muscular articulations are crucial for active bending of the arms. All other articulations were composed of ligaments, which did not allow for active movement and represented rigid connections between the ossicles. Thus, it is concluded that the arms were not as flexible as to bend them backwards to form the parabolic filtration fan, and a different feeding position is assumed, where the arms formed a tear shape, similar to the survival posture living stalked crinoids adopt in high flow velocities.

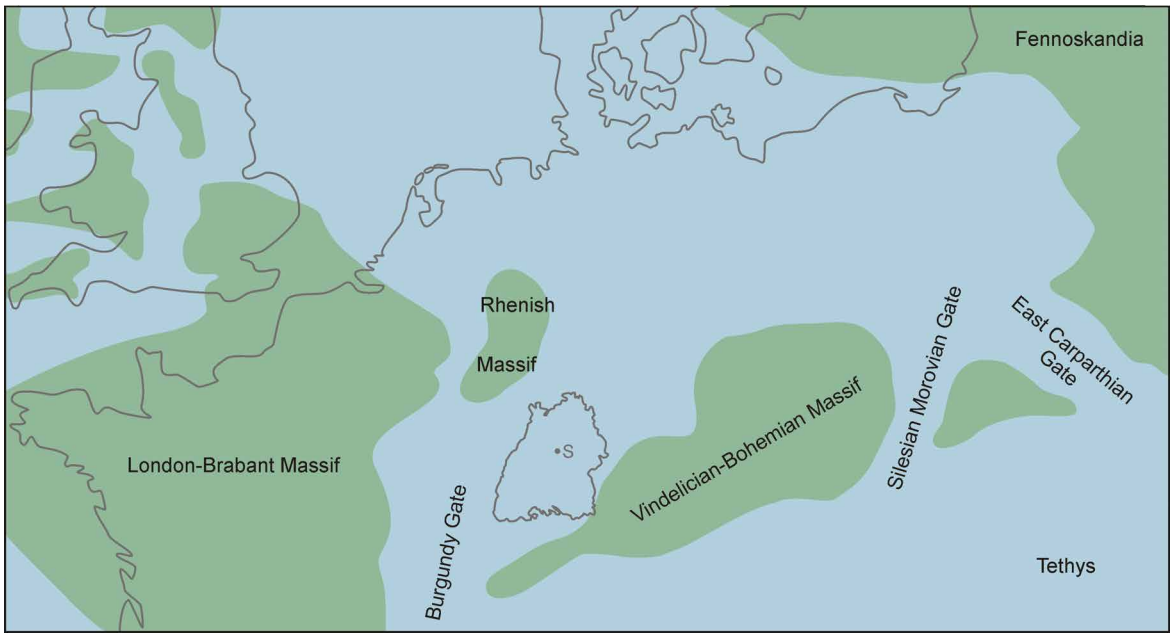

Figure 6: Palaeogeography of the Central European Basin during the upper Muschelkalk, following Hagdorn (1999) and Geyer et al. (2011). S: Stuttgart, Germany.

The Triassic period in Central Europe is characterized by complex tectonic activities, which led to the formation of the Central European Basin (Feist-Burkhardt et al., 2008). During the middle Triassic Muschelkalk (Anisian to early Ladinian), marine carbonates were deposited in this basin due to a transgression of the Tethys Ocean. Large parts of Germany were covered by this peripheral sea (Fig. 6), and while the lower and middle Muschelkalk deposits indicate alternations between marine and terrestrial settings, the limestones of the upper Muschelkalk reflect fully marine conditions. In Southern Germany, fossiliferous sediments formed in a restricted part of the basin. The region around Crailsheim, about 80 km to the north-east of Stuttgart, is famous for mass accumulations of *E. liliiformis* ossicles, the so called “Trochitenkalk” of the Crailsheim Member. These sediments, which reach a thickness of up to 16 m, formed under shallow marine conditions (above storm wave base respectively in parts also above fair weather wave base) on a gently inclined carbonate ramp (Vollrath, 1957; Aigner, 1985; Aigner and Bachmann, 1992). Flow conditions, including flow direction as well as velocity, probably varied in short time intervals in these settings. About 70 km to the west, the Trochitenkalk Member reflects a more basinal setting between wave base and storm wave base (Hagdorn, 1999), with intercalations of marls and clays between limestone beds, and an assumed water depth of no more than 180 m (Linck, 1954, 1965). In this habitat, flow conditions may have been more constant, so that changes in flow conditions occurred less rapidly and flow velocities were lower than in the settings around Crailsheim.

3.2 Flow tank experiments (PIV)

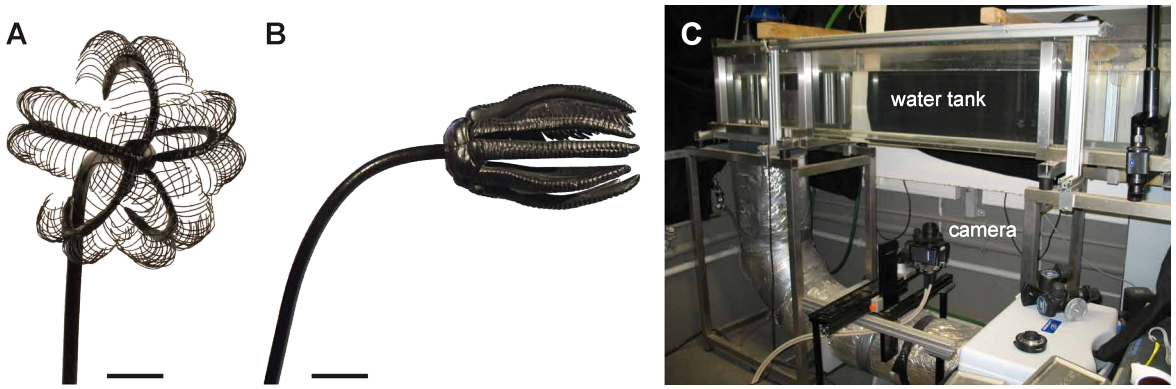

Figure 7: PIV experiments. A: resin-wire model of *Hyocrinus* sp., scale bar 20 mm; B: resin-wire model of *E. liliiformis*, scale bar 15 mm; C: flow tank at the Institut für Zoologie, Universität Bonn.

Flow tank experiments were performed using 2D Particle Image Velocimetry (PIV), a laser optical method to monitor flow directions and velocities. The experiments were realized in cooperation with Dr. A. Klein and Prof. H. Bleckmann at the Institut für Zoologie, Rheinische Friedrich-Wilhelms-Universität Bonn. For the experiments, partly flexible resin-wire models of *Hyocrinus* sp. (Fig. 7A) and *E. liliiformis* (Fig. 7B) were constructed with Apoxie®Sculpt, and painted in black matt car finish. The models were simplified by restricting them to the skeletal parts of the animals (stalk, calyx, arms and pinnules). In addition, the model of *E. liliiformis* had only three instead of all ten arms pinnulated.

The models were analysed in a recirculating fresh water tank (with a height and width of 280 mm) at 15°C water temperature, using seeding particles with diameters of 50 µm (PSP 50, Dantec Dynamics). The measurement area had a size of 134.7 mm by 134.7 mm, and was positioned in the XZ plane (laser sheet Pegasus, 527 nm), with the origin of the coordinate system in the centre of the crinoid crown. A laser produced light pulses over a defined time period illuminating the seeding particles. This procedure was videotyped by a high speed camera (Photron Ultima APX) positioned underneath the water tank (Fig. 7C), with 250 frames per second at 5 different Y locations (-40 mm, -20 mm, 0 mm, +20 mm, +40 mm). The images were calibrated with a two level calibration plate (Typ 20, LaVision) and preprocessed by Dr. A. Klein with the software DaVis (LaVision) to obtain txt-files of the two velocity components u (originally V, adapted to conform to the denomination shown in Fig. 2; representing streamwise flow) and v (originally U; representing crosswise flow) sampled at 128 x 128 points distributed on a regular grid across the measurement area. In addition, the corresponding root mean square values (RMS) were calculated to evaluate the flow fluctuations during the experiments. Due to the technical setup the inflow velocities comprise V_{inits} of 0.142 m/s, 0.169 m/s and 0.219 m/s for *Hyocrinus* sp., and 0.14 m/s, 0.166 m/s and 0.213 m/s for *E. liliiformis*.

3.3 Computer simulations (CFD)

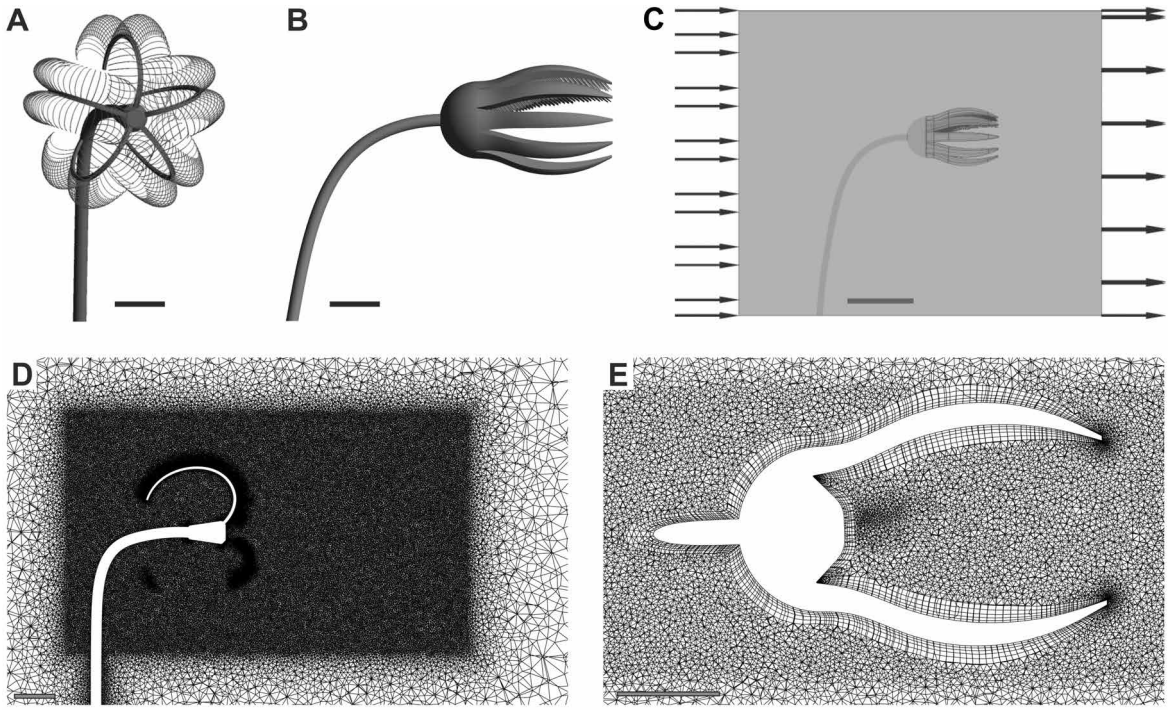

Figure 8: CFD simulations. A: 3D model of *Hyocrinus* sp., scale bar 20 mm; B: 3D model of *E. liliiformis*, scale bar 15 mm; C: setup of CFD simulations, arrows indicating inflow and outflow direction (representation of fluid domain not to scale), scale bar 50 mm; D: mesh of *Hyocrinus* sp., scale bar 20 mm; E: mesh of *E. liliiformis*, scale bar 20 mm.

Numerical simulations were carried out by applying Computational Fluid Dynamics (CFD), a computer based method for calculating fluid flow. This method is based on the numerical solution of partial differential equations solved for a continuous domain under specified boundary conditions. In the presented project, the finite volume based software CFX of the ANSYS Academic Research Releases 13 and 15 was used to simulate steady state flow based on the Navier Stokes equations. The change in software versions was analysed separately, and found to have no considerable effect on the resulting flow field (Appendix A).

Due to the complex three-dimensional geometries involved, the CFX solver was chosen over the alternative Fluent solver, and numerical simulations were performed with full models instead of using computationally less expensive axisymmetry options, with the exception of the tube feet submodel. Here, the four outer surfaces were set as symmetry boundaries to simulate a continous pattern in all spatial directions. The simulations were performed with default solver settings, and convergence was reached in less than 50 iterations (in most cases less than 30 iterations), using the default convergence criteria set to RMS values lower than $1.0E^{-4}$. For the solving process, HPC (High Performance Computing) resources of the bwGRiD project (http://www.bw-grid.de) and the bwUniCluster (http://www.bwhpc-c5.de) were used.

Table 1: Setup parameters and mesh details of CFD simulations

	freshwater parameters	seawater parameters
Density* [kg/m^3]	999.1	1026.021
Dynamic viscosity* [Pa·s]	0.001138	0.00122
Temperature [°C]	15	15
	Hyocrinus sp.	*E. liliiformis*
Crown length [m]	0.065	0.07
V_{init} [m/s]	0.142/0.169/0.219	0.14/0.166/0.213
No of mesh elements (CFD)	30 131 705	11 051 136
Average element skewness	0.22	0.26
	N. decorus	tube feet submodel
Crown length [m]	0.038	—
V_{init} [m/s]	0.142	0.142
No of mesh elements (CFD)	50 551 473	4 279 077
Average element skewness	0.22	0.23
	E. liliiformis 10AP	*E. liliiformis* PiSp
Crown length [m]	0.07	0.07
V_{init} [m/s]	0.03/0.14/0.5	0.03/0.14/0.5
No of mesh elements (CFD)	6 735 251	6 913 313
Average element skewness	0.30	0.30
	E. liliiformis AO	*E. liliiformis* 7A
Crown length [m]	0.07	0.07
V_{init} [m/s]	0.03/0.14/0.5	0.03/0.14/0.5
No of mesh elements (CFD)	8 298 277	6 261 045
Average element skewness	0.29	0.29

*data following d' Ans and Lax (1992), Wagner and Kretzschmar (2008), and ITTC (2011)

For the comparison with the flow tank experiments, geometries of the crinoids were constructed copying the handmade resin-wire models as exactly as possible. The geometries include *Hyocrinus* sp. (Fig. 8A), and *E. liliiformis* with only three of the ten arms covered with pinnules (Fig. 8B). In the PIV experiments, the resin-wire models were not aligned perfectly in the centre of the water tank but showed some rotation, such that the CFD models were adjusted accordingly. The crinoid models were surrounded by a "box primitive" copying the dimensions of the flow tank, and then cut out of this box thus resulting in the fluid domain that was analysed in the upcoming simulations (Fig. 8C). The CFD meshing process using a tetrahedral unstructured grid to resolve the complex geometries included a sizing with a body of influence around the crinoid crowns, using element sizing of 0.0012 m (Fig. 8D). For *Hyocrinus* sp., generating a mesh with inflation layers on the crinoid was not possible due to internal memory limitations, but for *E. liliiformis*, meshing these layers using default settings was successful (Fig. 8E). Inflation layers are build up of prisms forming a structured grid thus enabling a better numerical basis for the calculation of the boundary layer. Resulting mesh statistics are shown in Table 1. The setup parameters included the definition of the fluid domain by using freshwater parameters at 15°C (Table 1, following data provided

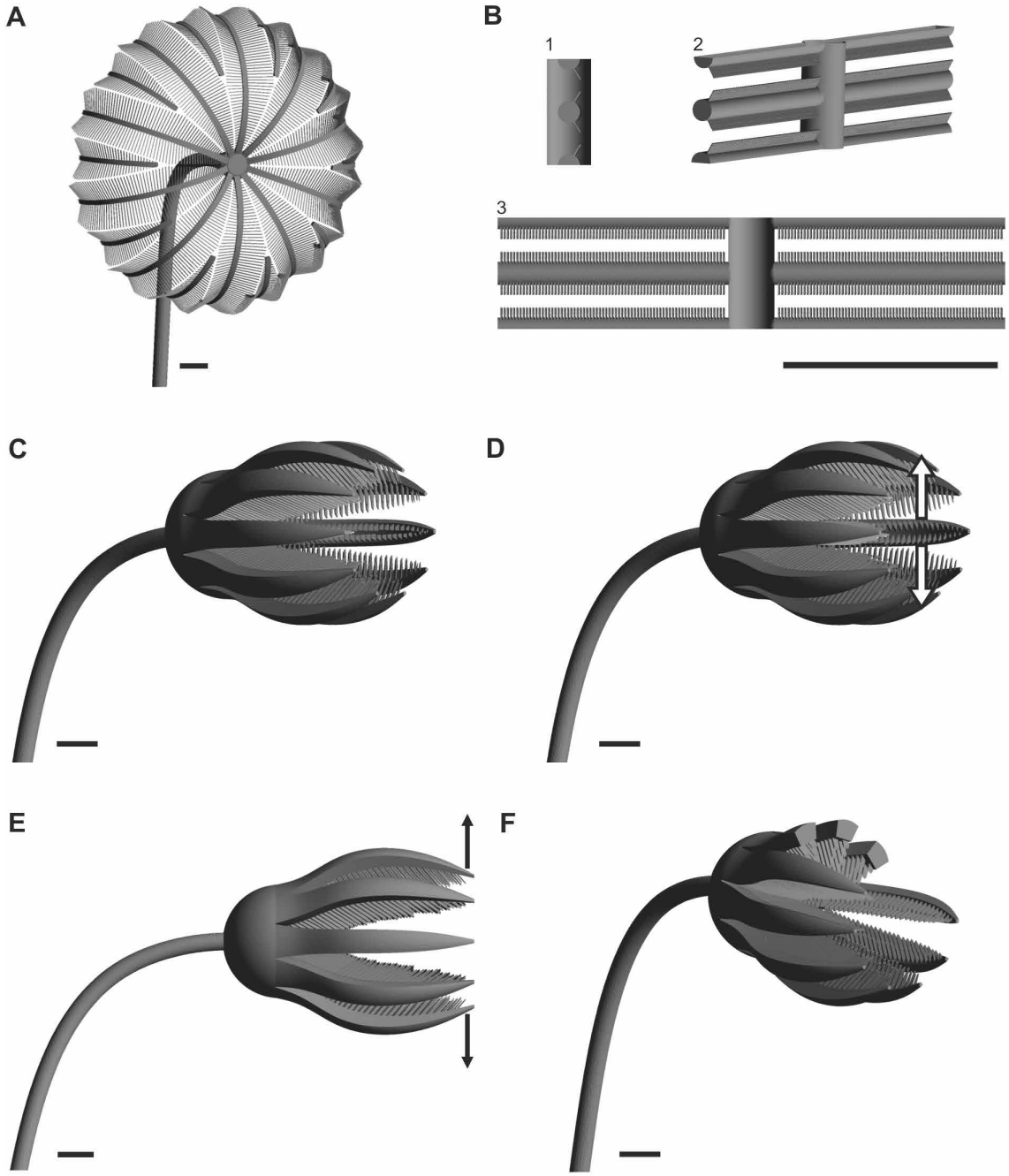

Figure 9: Expanded 3D models. A: 20-armed *N. decorus*; B: tube feet submodel in side view (1), perspective view (2), front view (3); C: *E. liliiformis* with all arms pinnulated (10AP); C: *E. liliiformis* with pinnules spread (PiSp), indicated by white arrows; D: *E. liliiformis* with arms opened (AO), indicated by black arrows; E: *E. liliiformis* with parts of three arms missing (7A). Scale bars: 10 mm.

by d' Ans and Lax,1992; Wagner and Kretzschmar, 2008; ITTC Fresh Water and Seawater Properties, 2011), and three inflow velocities equalling those applied in the PIV experiments, with an aboral inflow (velocity vector 1/0/0, parallel to the X-axis).

For further analyses, expanded simulations were performed, including seawater parameters (Table 1, based on ITTC Fresh Water and Seawater Properties, 2011) for the fluid domain, particle tracking simulations as well as new geometries (Fig. 9). The latter comprise:

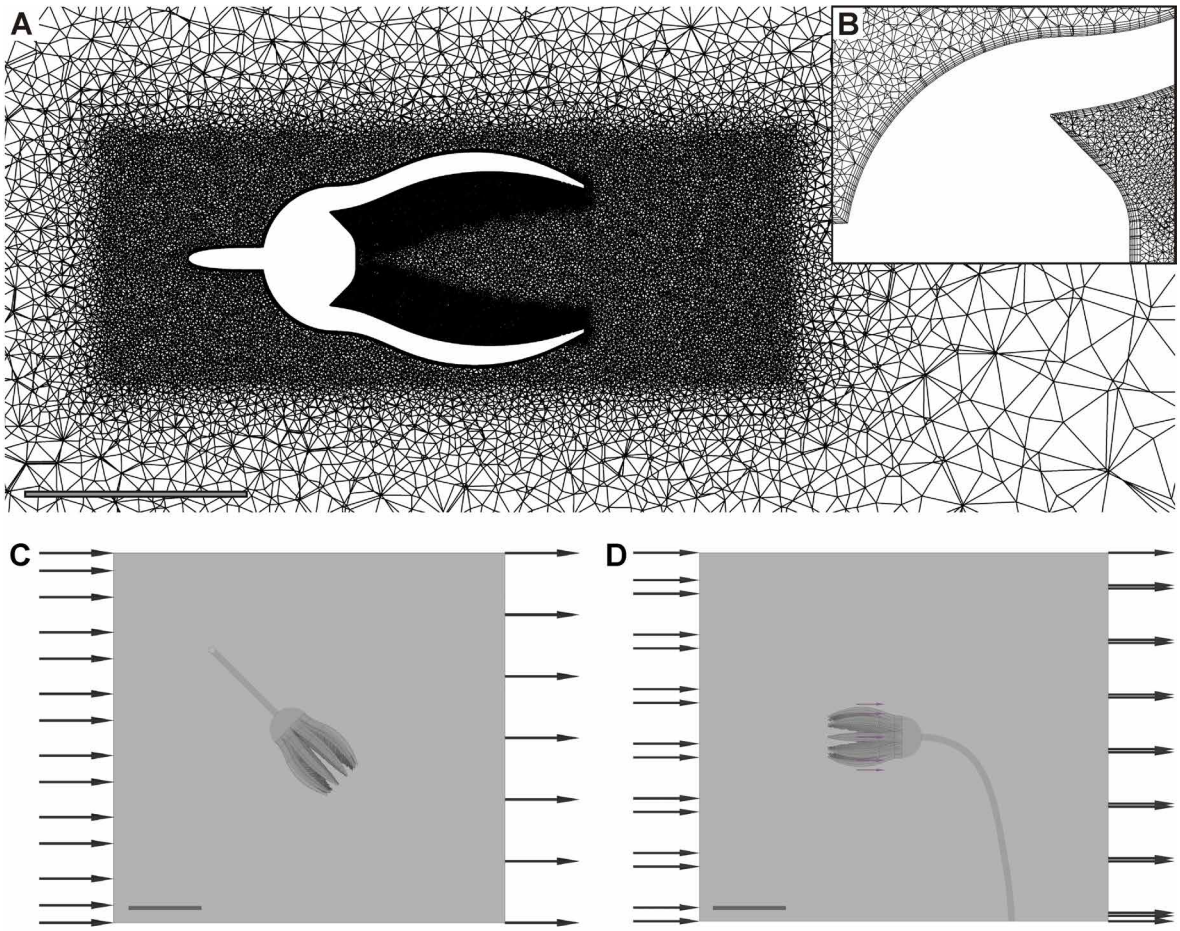

Figure 10: Mesh and additional inflow (directions indicated by black arrows) for *E. liliiformis*. A: mesh of the expanded model 10AP; B: detail of A, illustrating regular inflation layers on the model surface; C: slightly oblique inflow created through a rotation of the crinoid by 45° around the Z axis, top view; D: inflow from oral, side view. Scale bars: 50 mm, representation of fluid domain in C and D not to scale.

1) a model of a 20-armed *N. decorus* (Fig. 9A); 2) a submodel of part of an arm with several pinnules and tube feet (Fig. 9B); 3) a fully pinnulated model of *E. liliiformis*: 10AP (Fig. 9C), which then formed the basis for 4) *E. liliiformis* with a larger spreading degree of the pinnules: PiSp (Fig. 9D); 5) *E. liliiformis* with a wider opening of the arms: AO (Fig. 9E); and 6) *E. liliiformis* with parts of three arms missing to imitate autotomy or predatory action: 7A (Fig. 9F). The mesh of *N. decorus* was generated by using two bodies of influence for refinement, one surrounding the pinnules set to a sizing of 0.8 mm, the other one refining the close vicinity of the crown set to a sizing of 1 mm. For the comparison of *N. decorus* with *Hyocrinus* sp., the inflow velocity was set to 0.142 m/s as was investigated in the PIV experiments.

The meshes generated for the new *E. liliiformis* models were modified by setting the first inflation layer height to 0.1 mm (Fig. 10A, B). In order to evaluate the effect of this change in mesh topology on the flow, the results of both mesh types were compared at V_{init} = 0.14 m/s

and no significant difference was found (Appendix B). For *E. liliiformis*, additional inflow velocities of 0.03 m/s as well as 0.50 m/s were investigated, and the inflow direction was altered as to come from a slightly oblique angle (only model 10AP) (Fig. 10C) and from oral (Fig. 10D), to investigate changing conditions typcial for shallow water settings. The particle tracking simulations were performed by including 1000 one-way coupled particles with a density of ρ = 1080 kg/m^3 and a diameter of 150 µm. These values follow data published by Kitazawa et al. (2007) for diatoms. The particle injection region was defined as a full cone with an opening angle of 0°, a radius of 25 mm (respectively 70 mm for *N. decorus*), and a mass flow rate of 0.01 kg/s. For the tube feet submodel, the inlet was used as particle injection region with a uniform distribution of particles.

CFD today provides a very powerful tool to analyse flow phenomena in a large variety of industrial as well as scientific areas. Flow velocities and directions as well as pressure distributions, can be computed with very great detail and CFD results here yield reliable data even by using generally applicable setup parameters. For further interpretations of particular setups, especially as far as exact predictions on lift, drag, or flow separation are concerned, special mesh and setup requirements have to be fullfilled. In the presented study, the statements on these latter physical phenomena are of approximative nature (qualitative, not quantitative), but in future studies could be approached by resolving the boundary layer around the complex geometries in great detail, such that the SST instead of the very robust and widely applicable k-epsilon turbulence model can be used. This requires, however, powerful computer resources, which will probably be available in the near future with the increasing availability of computer clusters for High Performance Computing.

3.4 Data analysis

3.4.1 Comparison of PIV and CFD

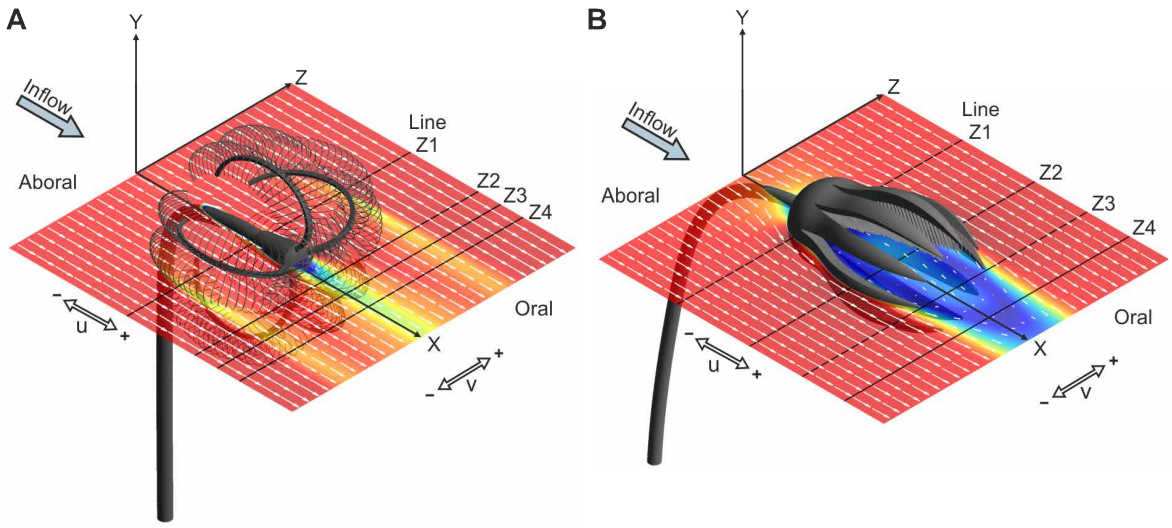

Figure 11: Setup to illustrate flow directions, velocity components, measurement plane and line transect positions for the comparison of PIV and CFD results. A: *Hyocrinus* sp.; B: *E. liliiformis*.

The PIV measurements provided values of the two velocity components u (parallel to the X-axis = streamwise) and v (parallel to the Z-Axis = crosswise), measured at 128 x 128 sampling points distributed on a regular grid across the measurement area (in the raw data the velocity components were denominated V and U with inverted values, but were adapted to the CFD coordinates for practical reasons). The values at light-sheet level Y = 0 mm (centre of the crown) yielded the best results for the interpretation of flow patterns. For a better convenience in interpretation and description the X origin of the PIV coordinate system was shifted to the beginning of the measurement range. From the CFD simulations, the same variables were obtained (Fig. 11).

The velocity components u and v were depicted as combined contour-vector plots, and at lines parallel to the Z direction, both parameters were extracted and plotted separately as line graphs. For *Hyocrinus* sp. (Fig. 8A), these lines are located at the beginning of the calyx (Line Z1), the end of the crown (Line Z2) and in the wake of the crinoid (Lines Z3 and Z4). For *E. liliiformis* (Fig. 8B), line positions comprise the widest diameter of the calyx (Z1), the widest opening of the arms (Z2), the end of the arms (Line Z3) and the wake of the crown (Line Z4). In the resulting line graph plots, negative u values indicate reversed flow direction, e.g. a value of -0.05 m/s represents a velocity of 0.05 m/s opposite to the inflow direction, whereas negative v values indicate a deflection in -Z direction. The line graph plots were created using Microsoft Excel (versions 2003, 2007 and 2010) and CorelDRAW X3 and X6, the combined contour-vector plots were computed with MATLAB (version 7.10.0).

3.4.2 Expanded CFD models

Similar to the comparison of PIV and CFD results, the flow pattern forming around the expanded models was analysed by extracting the velocity values at specified locations (Fig. 12), now including the third dimension, velocity component w (parallel to the Y axis). For *Hyocrinus* sp. and *N. decorus* (Fig. 12A, B), the three individual velocity components were obtained from two lines, one just in front of the beginning of the arms (Line Z1), and one at the end of the crown (Line Z2). In addition to the ZX plane at Y = 0 mm, more sections were introduced, including plane XY and two YZ planes at the same X coordinates as Lines Z1 and Z2 (for clarity, these planes are not shown in the illustrations of Figure 12A, B).

The flow field of the tube feet submodel was investigated by plotting the velocity distribution on a XY plane positioned as to cut through the centre of a tube foot (Fig. 12C). Additionally, two lines were introduced parallel to the X axis, with Line X1 being located in the gap between the tube feet of two adjacent pinnules, and Line X2 at the centre of the middle pinnule. A third line, Line Z1, runs parallel to the Z axis (and thus the middle pinnules), with a distance to the model of 1.55 mm. Furthermore, three YZ planes were introduced at the beginning of the arm, the end of the pinnule and the end of the arm (these and the coordinate axes are not depicted here, but can be found in the results section).

For *E. liliiformis* with an oral inflow direction (Fig. 12D), the locations include an additional plane in XY direction and a line parallel to the X axis (X1), starting at the tegmen. The lateral inflow was analysed with similar XY and ZX planes (the corresponding positions are shown in Fig. 12E in topview to illustrate the position where plane XY crosses the model). Results for an aboral inflow direction (Fig. 12F) were studied at two additional lines, Line Z1 (just in front of the arms), and Line Z2 (10 mm in front of the tegmen). At the same X locations, two YZ planes were introduced (for clarity, Plane YZ1 and YZ2 are not shown).

The expanded CFD models include particle tracking simulations, which enable the monitoring of particle behaviour, illustrated herein as trajectory and line graph plots of the velocity plotted against X respectively the time the particle needed to pass through the computational domain. For *E. liliiformis* with an aboral inflow direction, additional isosurface plots were created to illustrate the extension of the recirculation area. For all three inflow directions, additional contour plots were used to display the static pressure distribution on the crinoid surface, and polylines following the outline of the model were used to extract and plot p_{stat}. The dynamic pressure was illustrated as contour line plots on different planes.

Figure preparation and results interpretation were performed using the following software packages: ANSYS CFX Post (versions 13 and 15), Intelligent Light FIELDVIEW (version 14), Microsoft Excel (versions 2003, 2007 and 2010), CorelDRAW X3 and X6, and Adobe Photoshop (versions 12.1 (CS5) and 13.0.1 (CS6)).

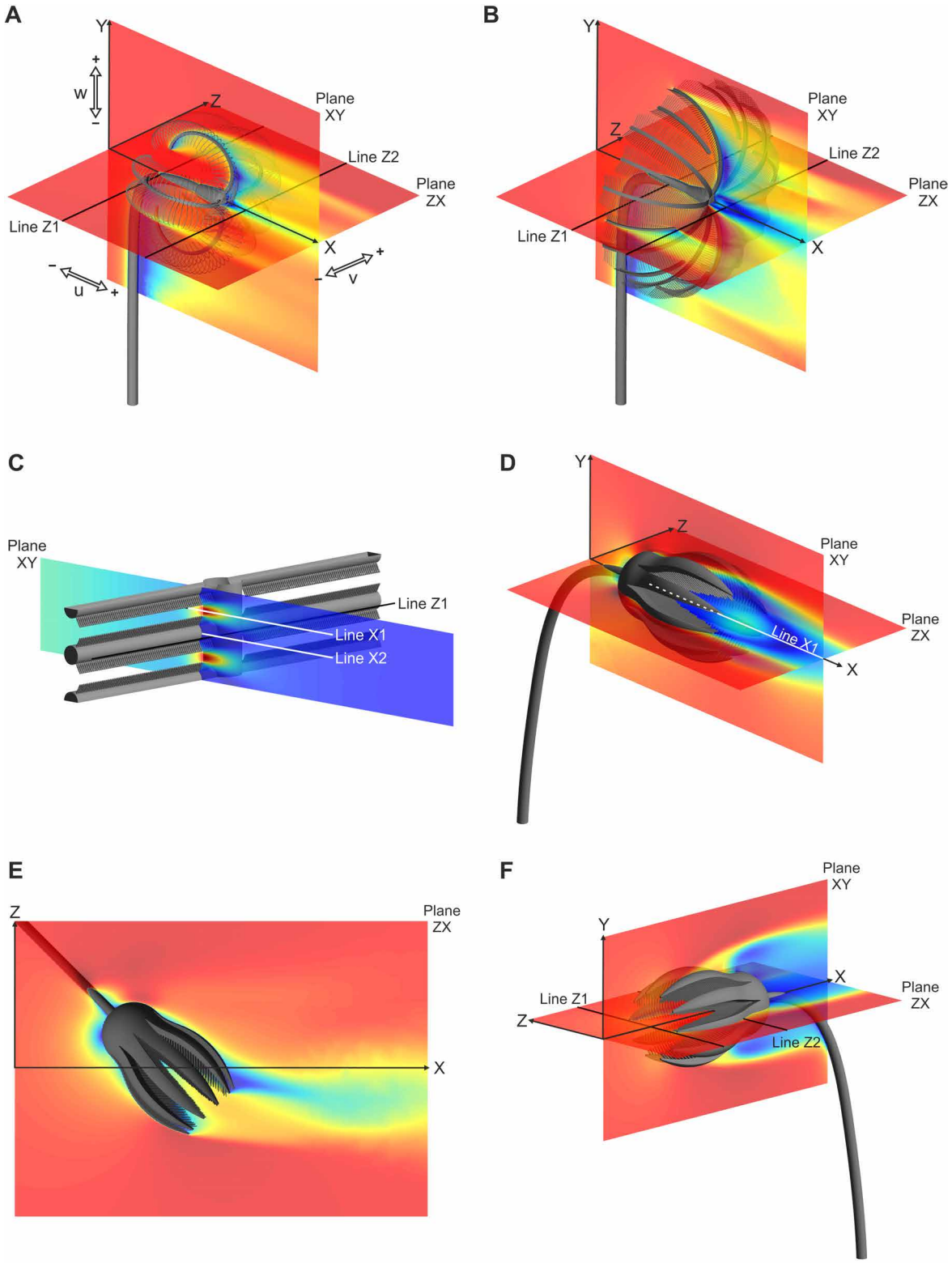

Figure 12: Setup to illustrate flow directions, velocity components, measurement planes and line transect positions for the expanded CFD models. A: *Hyocrinus* sp.; B: *N. decorus*; C: *E. liliiformis* with an aboral inflow direction; D: *E. liliiformis* with a lateral inflow direction (in top view); E: *E. liliiformis* with an oral inflow direction; *E. liliiformis* with an oral inflow direction illustrating the positions of the YZ planes.

4 Results

4.1 Comparison of PIV and CFD

4.1.1 *Hyocrinus* sp.

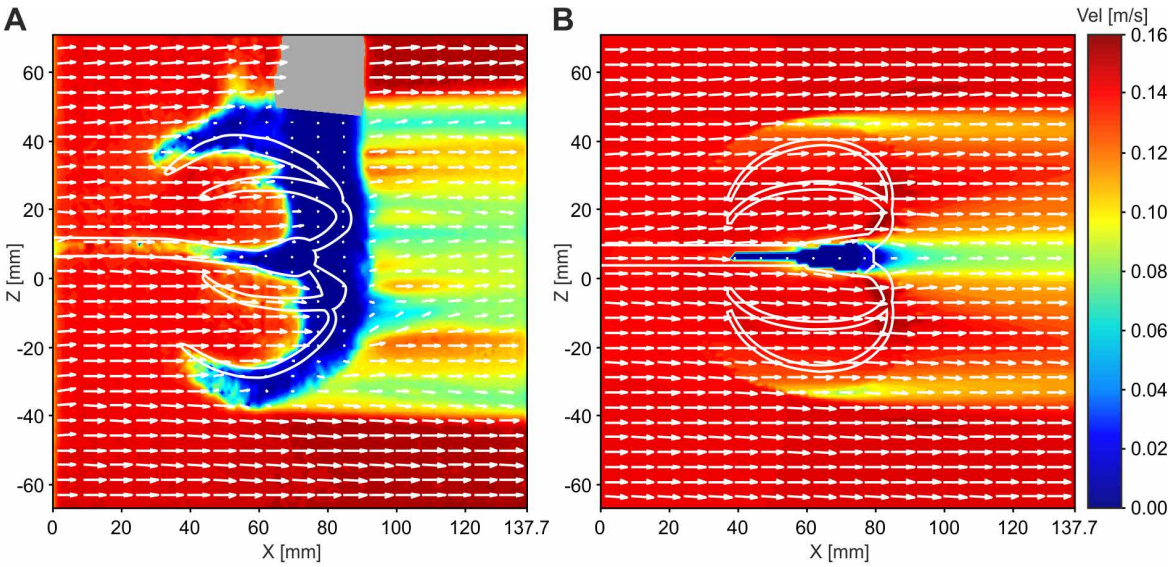

Figure 13: Results of flow analysis of the recent crinoid *Hyocrinus* sp. for V_{init} = 0.142 m/s illustrated as combined contour-vector plots. A: PIV results, area inaccessible to the laser in grey; B: CFD results.

The general flow pattern, resulting from the experiments and the computer simulations for the recent crinoid *Hyocrinus* sp., is similar and shows a straight flow of water through the crown for all of the three analysed velocities of V_{init} = 0.142 m/s $\pm$ 0.003 m/s, 0.169 m/s $\pm$ 0.004 m/s and 0.219 m/s $\pm$ 0.004 m/s. In detail, however, the results differ from each other, which can be attributed to deviations from the handmade resin to the computer generated 3D model. Due to the delicate nature of the pinnule, the wire used for the flow tank model is very thin and thus prone to irregularities in bending and spacing of the pinnules. The computer model, in contrast, is perfectly smooth and constructed of identical pinnule objects with constant spacing. This indicates the importance of the finer structures for the developing flow field. Owing to the experimental setup of PIV, some areas of the measurement plane were not accessible to the laser and do not yield results (grey region in the contour-vector plots).

The slow-down of the flow caused by the model with an inflow velocity of V_{init} = 0.142 m/s, is stronger in PIV compared to CFD (Fig. 13). In both cases, the vectors indicate a relatively unidirectional flow through the parabolic apparatus, with a stronger decrease in velocity at the arms, and a weaker decrease at the pinnules (yellow to light blue colours of the contour plots). Only in direct vicinity to the calyx, a small recirculation area exists, which already

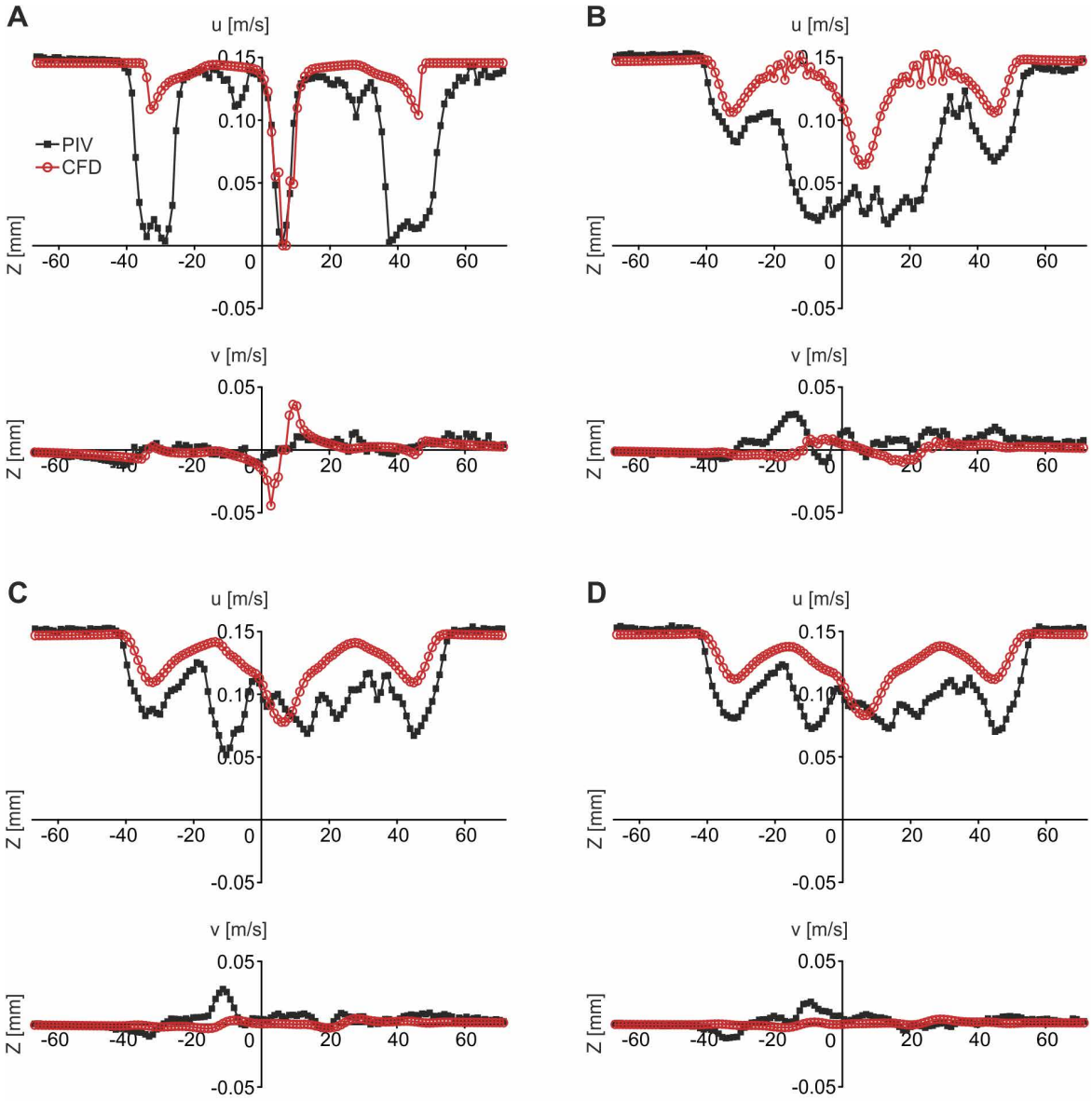

Figure 14: Results of flow analysis of the recent crinoid *Hyocrinus* sp. for V_{init} = 0.142 m/s, illustrated as line graph plots of velocity components u and v at 4 different transect lines. A: Line Z1 at the beginning of the calyx, equalling also the widest opening of the arms; B: Line Z2 at the end of the crown; C: Line Z3 in the wake, 10 measurement points behind Line Z2; D: Line Z4 in the wake of the crown, 10 measurement points behind Line Z3.

vanishes a short distance away from the crown. Root mean square (RMS) values of the PIV experiments (see Appendix C) indicate slight velocity variations at the upstream end of the arms and pinnules, but in general, however, the variations are low so that the mean values of PIV and steady state computer simulations provide a good representation of the overall flow pattern. PIV results of the additional measurement planes, which were not used for the comparison with CFD, are shown in Appendix D.

The two velocity components u and v at V_{init} = 0.142 m/s show overall similar curve progressions, but the higher impact of the PIV model on the flow compared to CFD is

recognizable in all four line transects (Fig. 14). In addition, velocity component u reveals that two of the five arms of *Hyocrinus* sp., arising beneath the measurement plane at Y = 0 mm, also are apparent in the PIV image at positions Z $\approx$ -8 mm and Z $\approx$ +27 mm. At the beginning of the calyx (Fig. 14A), the decrease in u_{PIV} at the arms in PIV almost reaches values of u = 0, whereas the CFD simulations provide lowest values of u_{CFD} = 0.1039 m/s. At the calyx, which also equals the widest opening of the arms, u reaches values of u = 0 m/s in both methods, but the crosswise deflection seen in component v is much higher in CFD compared to PIV. At the end of the crown (Fig. 14B), u_{CFD} values change only little compared to the beginning of the calyx, with u_{CFD} = 0.1058 m/s, while $_{PIV}$ increases to u_{PIV} = 0.0673 m/s. v_{PIV} varies stronger, and the highest crosswise deflection is caused by one of the arms lying beneath the measurement plane. In CFD, crosswise deflection is only caused by the calyx, while the influence of the arms on the flow has already vanished. With increasing distance from the end of the crown the differences in the results of PIV and CFD diminish (Fig. 14C, D), and the flow pattern stays relatively uniform.

Increasing the inflow velocity to V_{init} = 0.169 m/s and 0.219 m/s does not change the overall flow field (Fig. 15). The flow tank experiments and computer simulations continue to show similar patterns, and the general flow direction stays uniform with the water moving straight through the parabolic filtration fan. The combined contour-vector plots (Fig. 15A-D) illustrate the still higher impact of the PIV model on the flow compared to CFD. In PIV, the baffling effect of the crinoid model at V_{init} = 0.169 m/s does merely differ from the one observed at V_{init} = 0.142 m/s, while the higher inflow velocity of V_{init} = 0.219 m/s leads to respective higher values of u at the arms and pinnules (Fig. 15E). At the calyx, all three line graph plots show similar values in u. The progressions of the line graph plots of velocity component w do not differ considerably from each other. The CFD calculations, however, result in a uniform increase in both velocity components with increasing V_{init} (Fig. 15F).

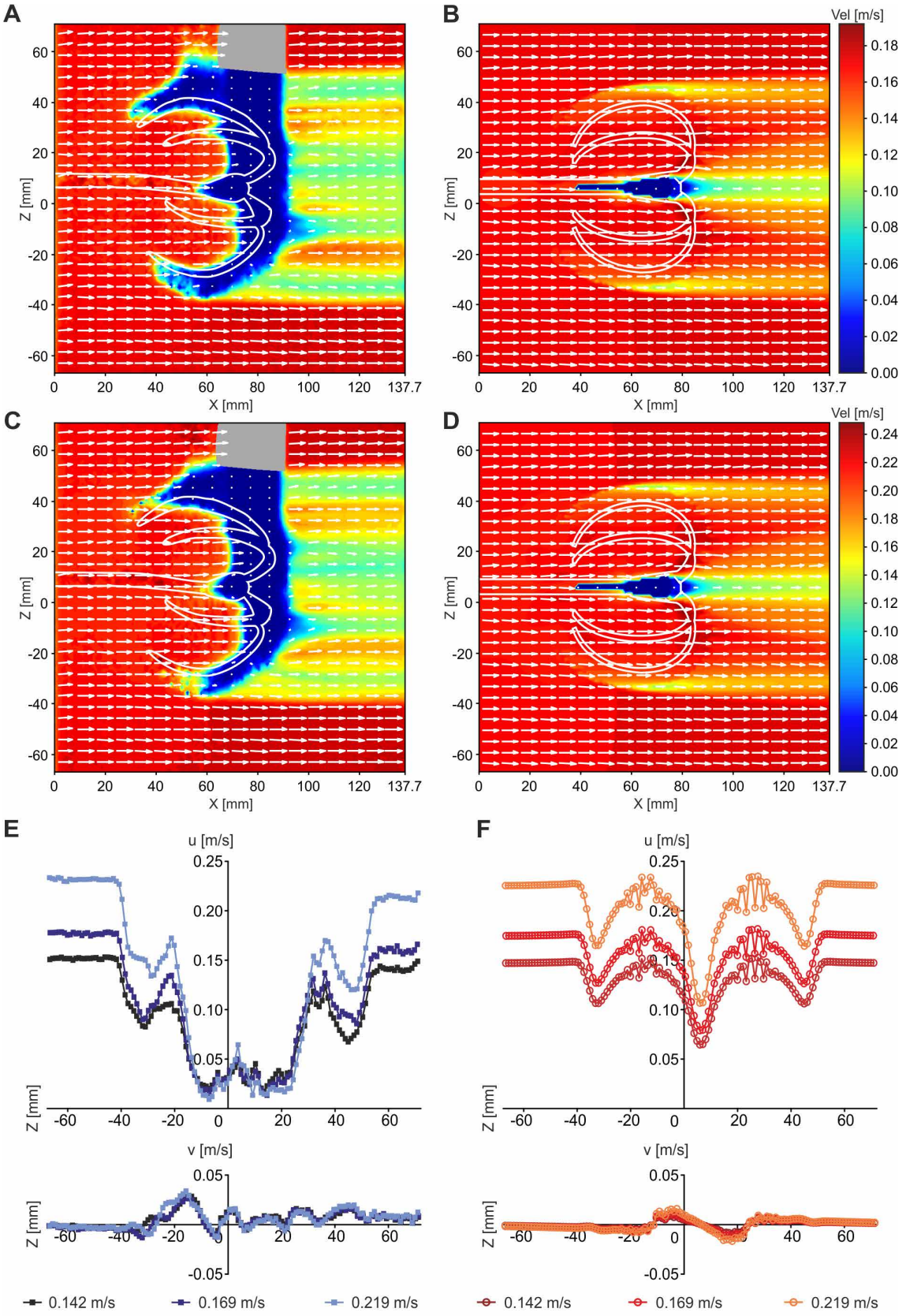

Figure 15: Results of flow analysis of *Hyocrinus* sp. for increased inflow velocities. A: PIV results for V_{init} = 0.169 m/s, area inaccessible to the laser in grey; B: CFD results for V_{init} = 0.169 m/s; C: PIV results for V_{init} = 0.219 m/s, area inaccessible to the laser in grey; D: CFD results for V_{init} = 0.219 m/s; E: PIV results of velocity components u and v at Line Z2 for all three inflow velocities; F: CFD results of velocity components u and v at Line Z2 for all three inflow velocities.

4.1.2 *Encrinus liliiformis*

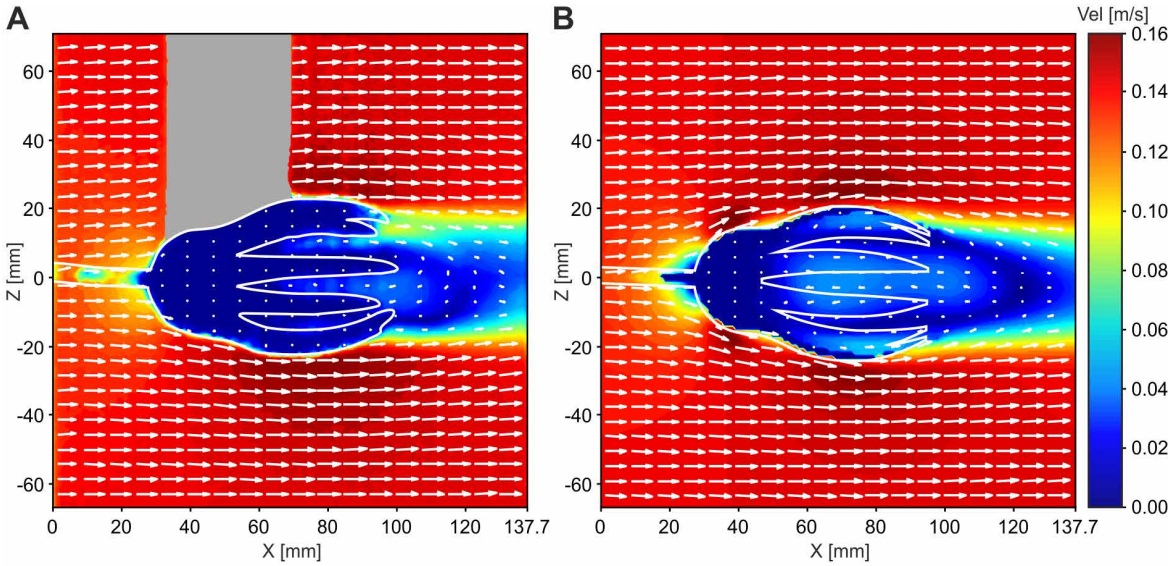

Figure 16: Results of flow analysis of the fossil crinoid *E. liliiformis* for V_{init} = 0.14 m/s illustrated as combined contour-vector plots. A: PIV results, area inaccessible to the laser in grey; B: CFD results.

The PIV and CFD results for the fossil crinoid *E. liliiformis* show a good agreement. As already noticed for *Hyocrinus* sp., observed differences in the results can be explained by slight and unavoidable deviations of the resin and the 3D model from each other. For all three inflow velocities of V_{init} = 0.14 m/s ±0.001 m/s, 0.166 m/s ±0.001 m/s and 0.213 m/s ±0.002 m/s, a recirculation of water into the crown occurs. As expected in this Reynolds number range (global Re ≈ 8600 – 13 000, considering the length of the crinoid crown as characteristic length), the RMS values (see Appendix E) indicate slight transient variations of the position and extant of the recirculation zone behind the crown, increasing with V_{init}. Transient CFD analyses using the steady state results as initialization, confirm this flow behaviour (see Appendix F). This undulation, however, is not strong and the general flow pattern is well represented by mean values of PIV and steady state simulations of CFD, which are less computationally expensive.

Due to a decrease in cross sectional area of the fluid at the maximum diameter of the calyx and the widest opening of the arms, the combined contour-vector plots for V_{init} = 0.14 m/s (Fig. 16) show an increase in velocity of the surrounding flow (darker red colours of the contour plots). The white arrows illustrate the crosswise deflection of the water being similar in direction, but CFD reaches higher values compared to PIV. In the wake of the crown, a decrease in velocity can be observed (darker blue colours). The vectors indicate a reversal of the flow direction, with the recirculation starting at the tip of the arms, where the flow is redirected into the filter apparatus. In the centre of this recirculation area, the velocity again increases (lighter blue colours). The parts of the measurement plane that were not

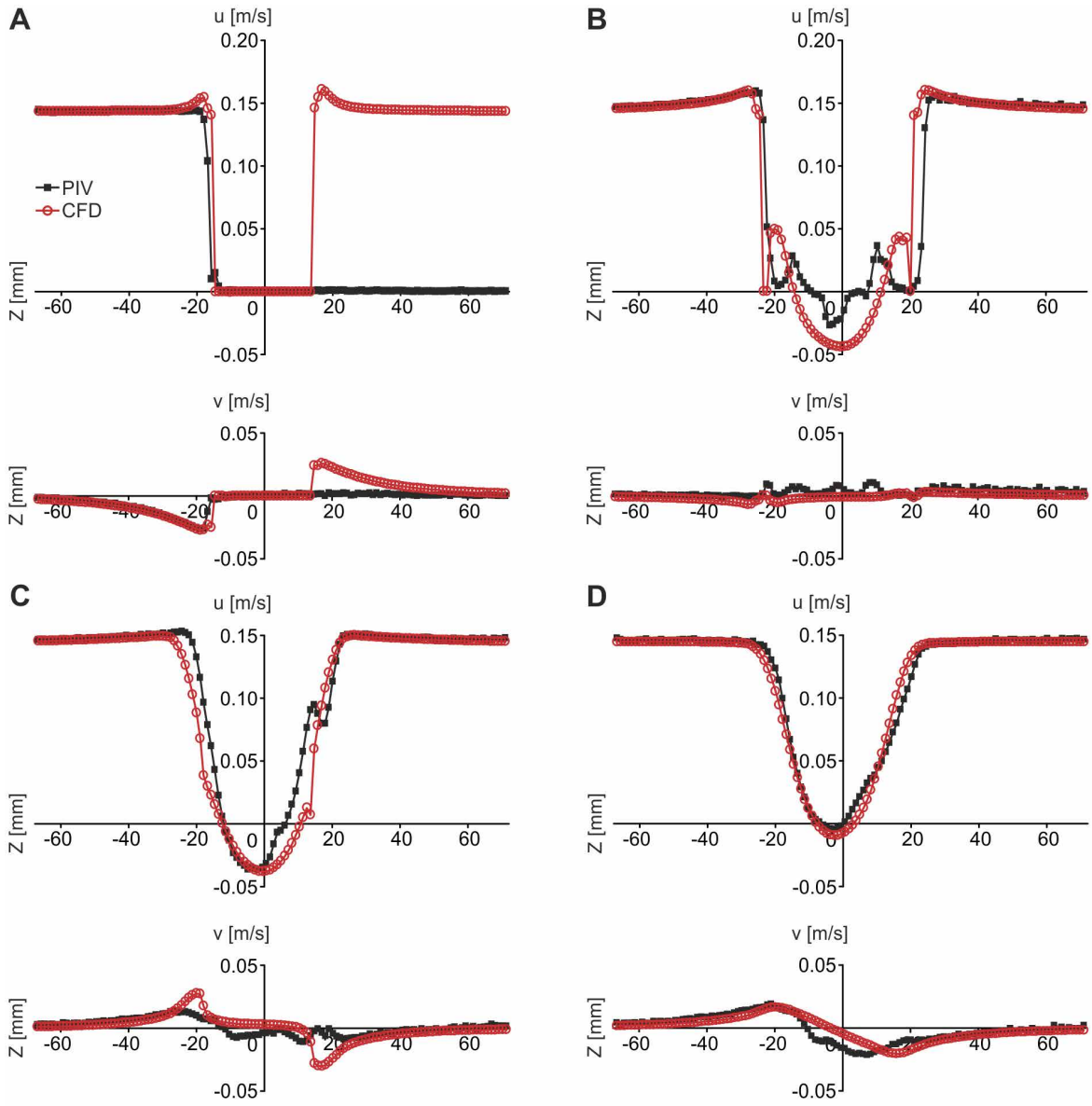

Figure 17: Results of flow analysis of the fossil crinoid *E. liliiformis* for V_{init} = 0.14 m/s, illustrated as line graph plots of velocity components u and v at 4 different transect lines. A: Line Z1 at the beginning of the calyx; B: Line Z2 at the widest diameter of the crown; C: Line Z3 directly behind the end of the arms; D: Line Z4 in the wake of the crown, 20 measurement points behind Line Z3.

accessible to the laser in the PIV experiments and thus do not yield results, include areas in +Z direction (displayed in grey) and the inside of the crown, which was partially obscured by the crinoid model itself. CFD provides spatially complete data, and shows that the highest recirculation velocities are reached in the centre of the crown. The contour plots reveal that flow separation at the outer surface of the body occurs some millimeters behind the widest diameter of the crown, before the end of the arms is reached. PIV results of the additional measurement planes are shown in Appendix G.

The comparison of u and v values for V_{init} = 0.14 m/s (Fig. 17) enables a more detailed illustration of the flow field. At the beginning of the calyx, u decreases where the fluid impinges

on the object and the flow follows the crown outline (Fig. 17A). Where the calyx reaches its widest diameter, the streamwise flow velocity reaches maximum values of u_{PIV} = 0.1447 m/s (RMS = 0.0077 m/s), and u_{CFD} = 0.1612 m/s. The difference here can be attributed to the simplification of the calyx in the computer generated 3D model, in which it was generated by a smooth half sphere, whereas the calyx of the handmade resin-wire model possesses details of the plate morphologies. Both methods result in a similar crosswise deflection, as can be seen by the curve progressions of velocity component v.

The same pattern can be observed at the widest opening of the arms (Fig. 17B), while here the increase in u in PIV and CFD does not differ as much as at the maximum diameter of the calyx, with u_{PIV} = 0.1592 m/s (RMS = 0.0067 m/s) and u_{CFD} = 0.16 m/s. Even though the PIV values gained from the inside of the crown of *E. liliiformis* are influenced by the overlapping of arms of the model, PIV still yields some values and the general flow pattern of PIV and CFD is similar. Both velocity components slow down to 0 m/s, where the arms lie in the measurement plane, and substantial negative u values are reached between the arms, indicating the reversal of the flow direction. Right behind the end of the crown (Fig. 17C), both velocity profiles describe an asymmetric curve, with a slight decrease in u only on one side of the model (at Z $\approx$ 18 mm). This anomaly is caused by a slight rotation of the resin-wire model in the flow tank (which was reproduced in the computer simulations), so that the arm in positive Z direction reached further downstream (this fact is obscured by the PIV model in the contour-vector plots). This asymmetry ceases in the wake of the crown (Fig. 17D), in PIV slower than in CFD. The velocity in reversed direction here reaches values of u_{recirc} = -0.0362 m/s (RMS = 0.0143 m/s) in PIV, and u_{recirc} = -0.038 m/s in CFD. The v component indicates higher crosswise deviation in the CFD simulations compared to the PIV measurements. The end of the recirculation area, represented by the change from negative to positive u values, is located 23.9 mm behind the end of the arms in PIV, and with 24.5 mm slightly further downstream in CFD.

An increase in inflow velocity (Fig. 18) does not change the general flow pattern, but at the end of the arms u_{recirc} reaches higher values with increasing V_{init}, thus producing a stronger velocity gradient inside the crinoid crown. Both methods result in a uniform change of the velocity profiles with increasing V_{init}. For V_{init} = 0.165 m/s, the recirculation velocity reaches values of u_{recirc} = -0.0425 m/s (RMS = 0.018 m/s) in PIV, and u_{recirc} = -0.0438 m/s in CFD; for V_{init} = 0.213 m/s u_{recirc} = -0.0551 m/s (RMS = 0.0257 m/s) in PIV, and u_{recirc} = -0.0536 m/s in CFD. In PIV, the end of the recirculation area shifts towards the crown, ending 20.6 mm respectively 17.4 mm behind the end of the arms. The same effect can be observed in CFD, while the computer simulations do not show such a strong alteration as the experiments, with the end of recirculation being located 24.3 mm and 24 mm behind the end of the arms.

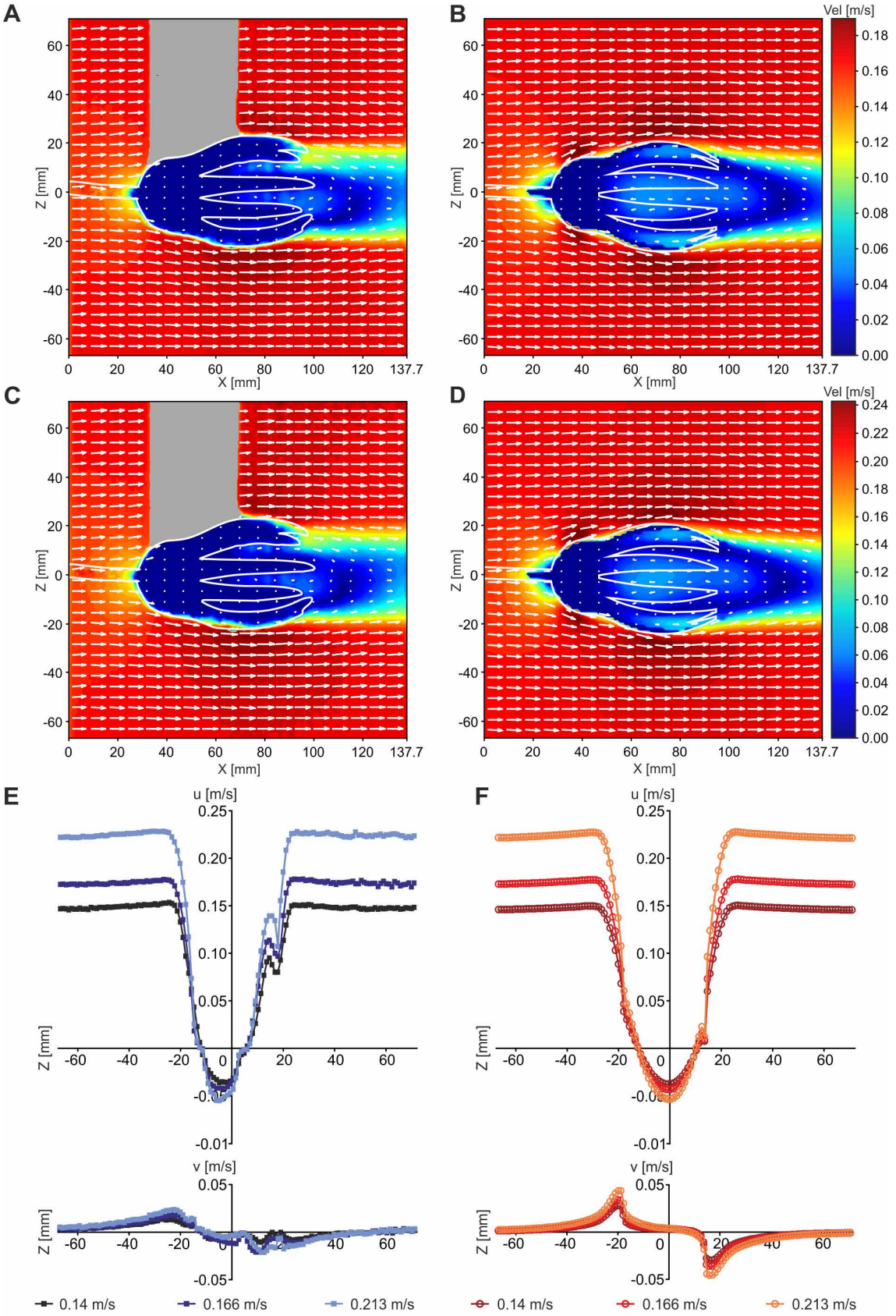

Figure 18: Results of flow analysis of *E. liliiformis* for increased inflow velocities. A: PIV results for V_{init} = 0.166 m/s, area inaccessible to the laser in grey; B: CFD results for V_{init} = 0.166 m/s; C: PIV results for V_{init} = 0.213 m/s, area inaccessible to the laser in grey; D: CFD results for V_{init} = 0.213 m/s; E: PIV results of velocity components u and v at Line Z3 for all three inflow velocities; F: CFD results of velocity components u and v at Line Z3 for all three inflow velocities.

4.2 Expanded CFD models

4.2.1 *Hyocrinus* sp.

The CFD analysis of the same 3D model of *Hyocrinus* sp. that was used for the PIV-CFD comparison, now with seawater as fluid, does not result in a significant change of the flow pattern. The water moves straight through the crown (Fig. 19A, B), only behind the calyx a small recirculation area develops. In the wake, the models' stalk, calyx and arms cause a relatively strong decrease in flow velocity (indicated by the dark blue colours). The pinnules that are oriented perpendicular to the inflow, lead only to a weak slow-down of the water, and the pinnules that are lying parallel to the inflow, lead to an increase in velocity between them (darker red colours). The effect of the stalk on the upstream flow is clearly recognisable by a zone with decreased velocity, which extends about 10 mm in upstream direction, while the influence of the crinoid crown on the upstream flow is relatively weak and the velocity in front of it does not differ significantly from the inlet velocity of 0.142 m/s.

A more detailed pattern is revealed by limiting the velocity range to V = 0.102 – 0.142 m/s (Fig. 19C-E). On the YZ plane just in front of the tips of the arms (4.5 mm in front of the oral surface of the calyx, Fig. 19C), only a very restricted area shows values lower than the initial velocity, with values of V = 0.136 m/s (representing a slow-down of 4.2 % in relation to V_{init}). In the centre of the crown, the water enters the filter apparatus almost with V_{init}, with values of V = 0.141 m/s. Due to the presence of the stalk, the decrease in velocity in front of the two lower arms is not as strong as in the upper portion of the crown.

In the wake, about 1.25 mm behind the oral surface of the calyx, the contour plot shows the decrease in velocity caused by the calyx and arms with a very steep gradient (Fig. 19D). Again, it is apparent that the pinnules lying perpendicular to the flow, cause a slow-down, while the water passes the pinnules oriented parallel to the flow direction with increased velocities. Only downstream of the stalk, this effect does not occur and instead, the water behind some of the pinnules is slowed down and reaches values of V = 0.102 m/s and lower. The contour lines in Figure 19E illustrate the irregular shape of the baffling effect of the crinoid on the flow. Upstream of the crinoid, no confined area of decreased velocity exists and the water enters parts of the filter without considerable lower flow velocities. Inside the crown, the flow is apparently slower than V_{init} before reaching the upper arm, and a small stagnation point exists at the beginning of the calyx. Downstream of the crinoid, the arms and especially the calyx have the strongest effect with zones of decreased velocity extending about 120 mm into the wake with values of V < 0.102 m/s.

The graphic representation of the total velocity V and its individual components u, v and w as line graph plots (Fig. 20) gives more insights into the details of the flow pattern developing

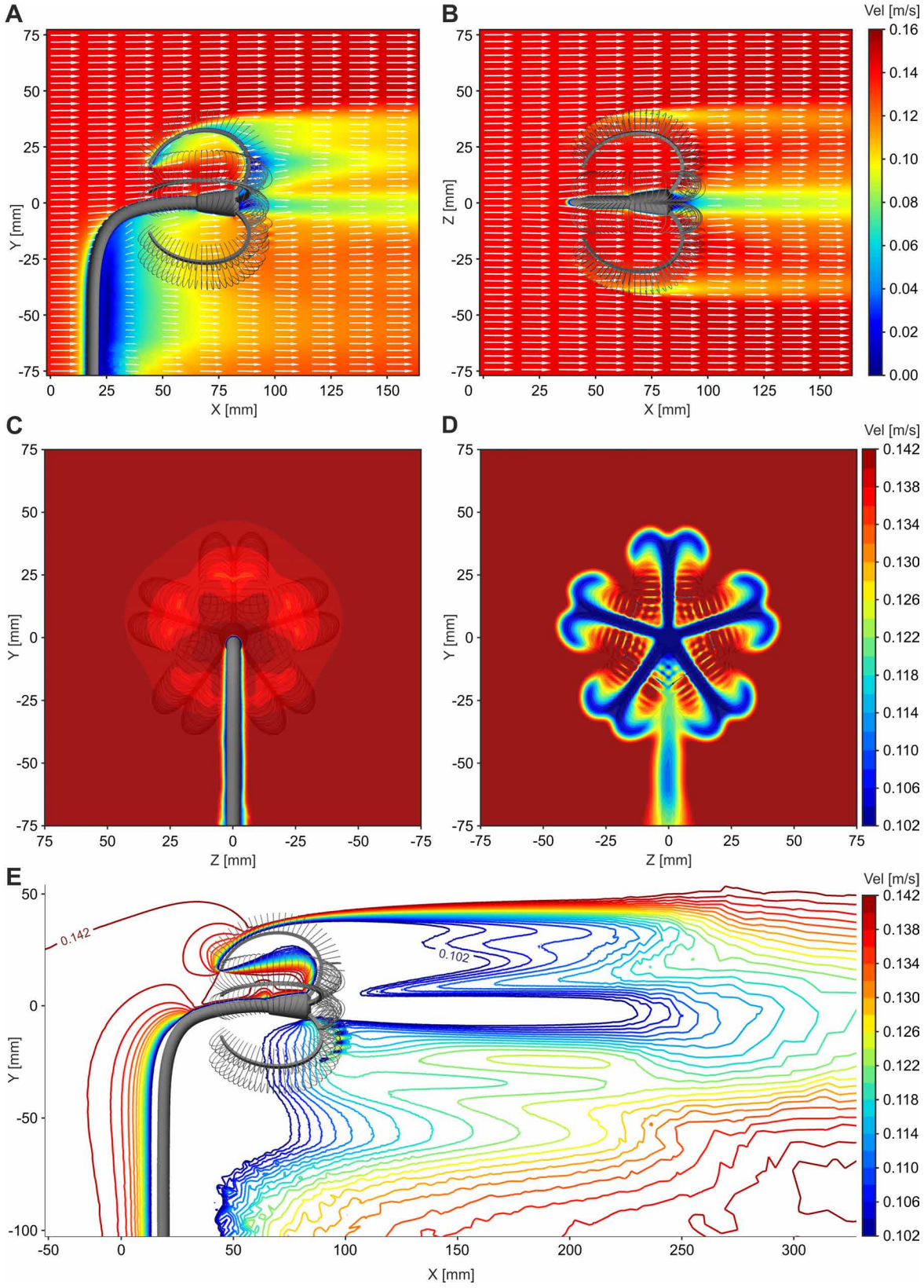

Figure 19: Results of flow analysis of the recent crinoid *Hyocrinus* sp. with seawater as fluid and V_{init} = 0.142 m/s. A: combined contour-vector plot on XY plane; B: combined contour-vector plot on ZX plane; C: contour plot on YZ plane at the beginning of the arms, D: contour plot on YZ plane at the end of the arms; E: contour lines on XY plane.

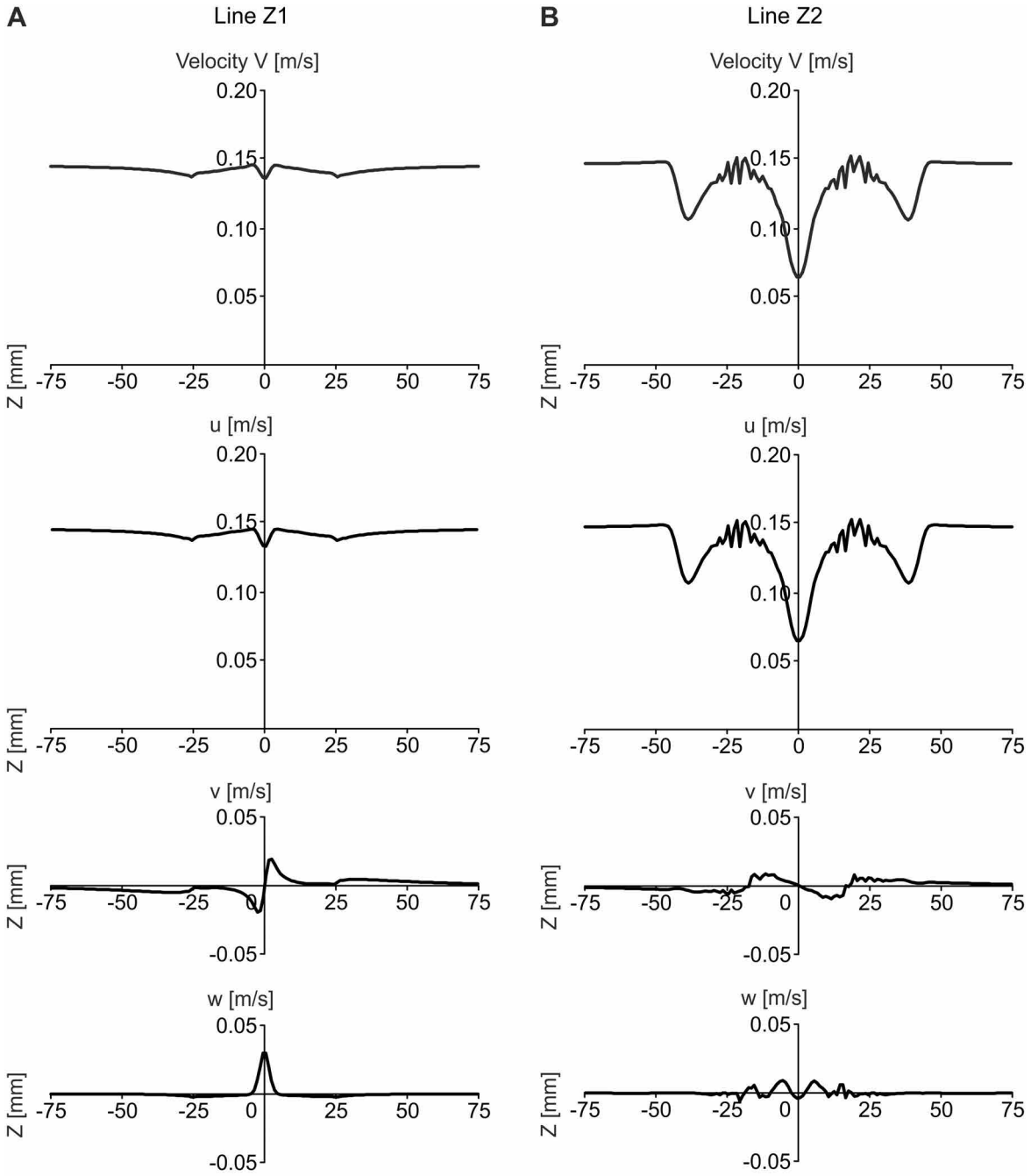

Figure 20: Results of flow analysis of *Hyocrinus* sp. with seawater as fluid and V_{init} = 0.142 m/s illustrated as linegraph plots of the total velocity and the three individual velocity components. A: Line Z1 at the beginning of the arms; B: Line Z2 at the end of the arms.

around the model of *Hyocrinus* sp. At Line Z1 (Fig. 20A), upstream of the crinoid, the diagrams show that the total velocity V and the velocity component u have almost similar curve progressions. The stalk and two of the five arms cause a slight decrease in the total velocity, with the lowest values in front of the stalk with V = 0.1357 m/s, representing a slow-down of 4.4 % in relation to V_{init}. While the arms evoke almost no change in all of the three velocity components, the stalk leads to a decrease in u down to 0.1321 m/s, and a deviation of the water in -Z/+Z and +Y direction.

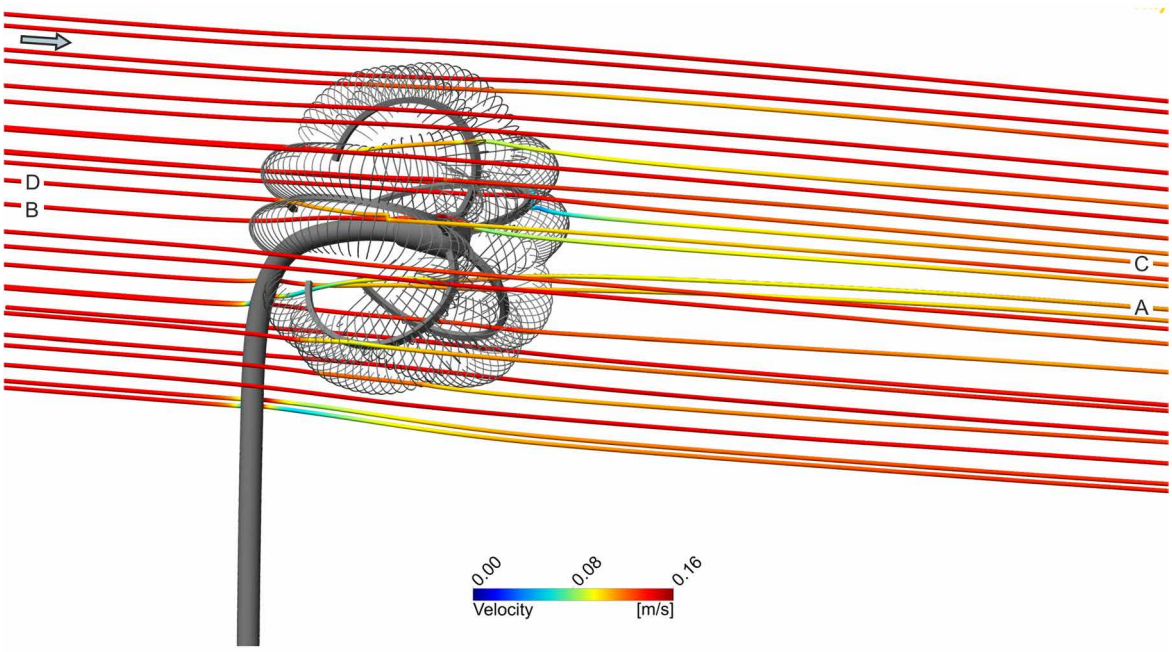

Figure 21: Trajectories of particles imitating plankton with a density of 1080 kg/m^3 and a diameter of 150 µm; labels indicate trajectories presented in Figure 22.

Downstream of the crown, at Line Z2 (Fig. 20B), velocity component u is still the main contributor to the total velocity V. The decrease in V is caused mainly by the arms with values of V = 0.1058 m/s, accounting for a slow-down of 25.5 % of V_{init}, and the stalk and calyx with V = 0.0642 m/s (54.8 %). The deviation of the water in Y and Z direction is stronger compared to the upstream flow, with v = -0.0117 m/s and w = 0.0128 m/s. The zigzag progression of the curves represents the effect of the pinnules on the flow, and can be traced back to an alternating decrease in velocity, where the flow hits the pinnules, and increase in velocity between two adjacent pinnules.

The particle trajectories (Fig. 21) support the observation that no large scale recirculation forms at the parabolic filtration fan of *Hyocrinus* sp. and the particles move straight through the crown without being redirected onto the oral surface. Some of the particles hit the pinnules and arms directly, while others pass the filtering structures in close vicinity or are slowed down by the stalk and the calyx before entering the filter apparatus (clear colour change of the particle trajectories).

To analyse the particle behaviour, the total velocity V of 4 exemplary chosen particles, which are indicated in the trajectory plot of Figure 21, is plotted against the X coordinate (Fig. 22). One particle passes the stalk (A), one the calyx (B), one an arm (C), and one a pinnule (D). Particle A exhibits the highest velocity gradient on its path, first slowing down to V = 0.0447 m/s, followed by an increase in velocity of up to V = 0.1796 m/s while passing the stalk. Then the particle velocity decreases again to V = 0.0608 m/s, then speeds up slightly until it reaches the filter and slows down a second time at one of the lower arms. In the wake

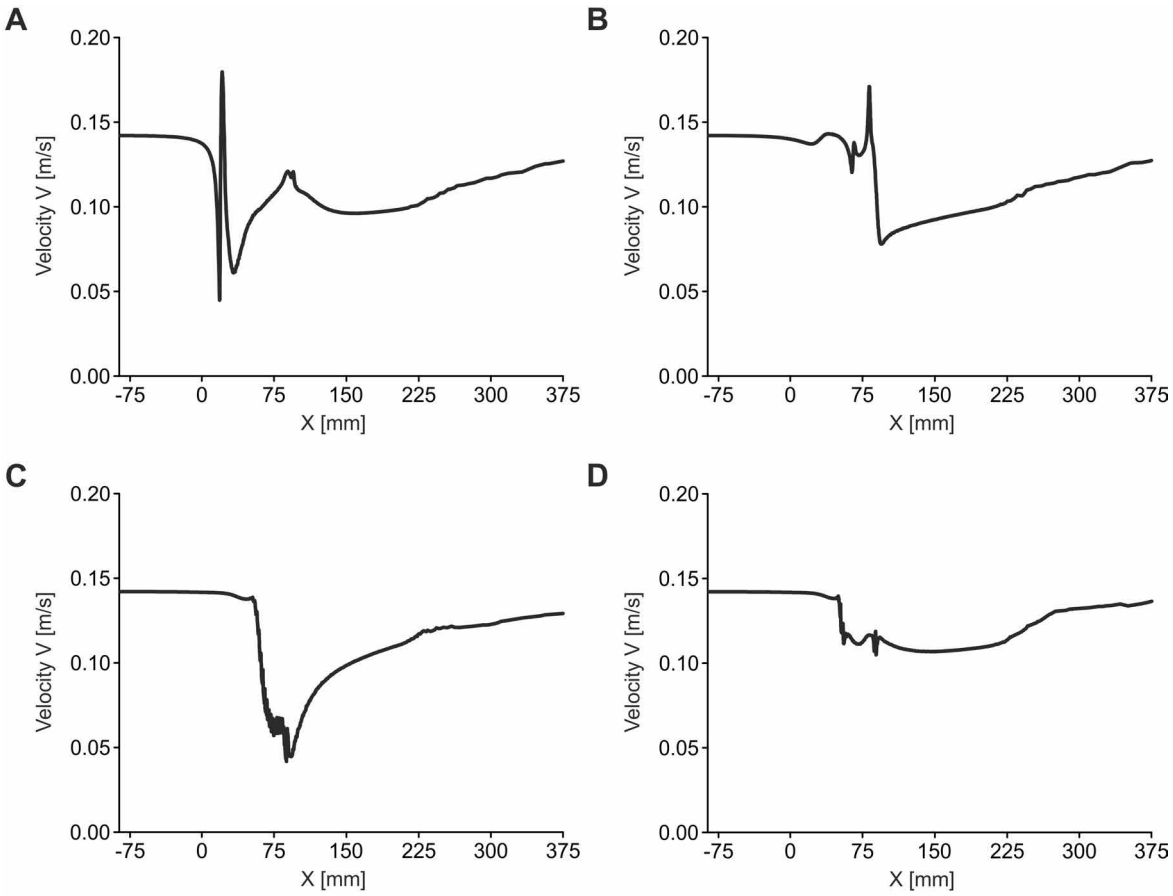

Figure 22: Total velocity of particles in X direction (corresponding trajectories marked in Figure 21). A: particle passing the stalk; B: particle passing the calyx; C: particle passing an arm; D: particle passing a pinnule.

of the crinoid, the velocity of particle A increases constantly. Particle B, passing the calyx, first slows down in front of the calyx, speeds up while passing the calyx to V = 0.171 m/s, then slows down to V = 0.0779 m/s and constantly gains velocity after leaving the crinoid crown. Particles C and D, passing an arm respectively a pinnule, both merely slow down before reaching the crinoid, and in contrast to particle A and B do not speed up while passing one of the filtering structures. Instead, both follow the outline of the arm/pinnule for some distance, particle C showing the strongest slow-down of all particles with V = 0.0418 m/s, particle D exhibiting the weakest slow-down with V = 0.1048 m/s.

4.2.2 *Neocrinus decorus*

The flow simulation of the simplified *N. decorus* model results in straight flow of water through the parabolic filtration fan, similar to that observed in *Hyocrinus* sp., as is shown in the combined contour-vector plots (Fig. 23A, B) by the distribution and direction of the total velocity V. The flow slows down considerably at the stalk, calyx and arms (blue colours of the contour plot), but the deviation -Y/+Y and -Z/+Z direction is generally small, as is indicated by the vector plots. The area, where the slow-down of the water is caused by the vertical part of the stalk, reaches at least 10 mm into upstream direction (Fig. 23A). Upstream of the crown, the flow velocity slightly decreases, indicated by the lighter red to orange colours in the range of X = 60 – 70 mm and Y= 0 – 50 mm (Fig. 23A) respectively Z = -50 – 50 mm (Fig. 23B). In the wake of the calyx, a relatively large recirculation zone develops with water movement in -X direction and a slight deviation in +Y direction. The slow-down of the flow behind the lower arms (in -Y direction) is influenced by the presence of the stalk, resulting in a broader area with decreased flow velocities compared to the upper arm (in +Y direction). Above the crown, laterally, and between the arms, the water velocity increases (darker red colours in Fig. 23 A,B).

The contour plots of Figure 23C-E illustrate the velocity distribution in front of the crown and directly behind it, with a velocity range limited to Vel = 0.102 – 0.142 m/s. The slow-down of the water in front of the crown (20 mm in front of the oral surface of the calyx) is visible in Figure 23C as circular contours, reaching the lowest values in the centre (orange contour with V = 0.130 m/s, accounting for a slow-down of 8.5 % in relation to V_{init}). In the wake of the crown (about 3 mm behind the oral surface of the calyx), the velocity distribution has high gradients with a strong decrease in velocity behind the arms and calyx, intensified by the stalk in -Y direction, and small scale increases caused by the closely spaced pinnules (Fig. 23D). The baffling effect of the crinoid is illustrated by the contour lines in Figure 23E, with a convex shape protruding in -X direction, slowing down the upstream flow, and an irregular zone of decreased velocity, extending more than 200 mm into the wake with velocity values lower than V = 0.102 m/s.

The evaluation of the individual velocity components (Fig. 24) illustrates the flow directly in front of and behind the crown in more detail. At the beginning of the arms (Fig. 24A), the curve progression of V and u do merely differ from each other, with a very slight decrease in velocity in front of the arms down to V = 0.1343 m/s (representing 94.6 % of V_{init}). In contrast to the model of *Hyocrinus* sp., Line Z1 crosses the stalk so that values of zero velocity are reached at Z = 0 mm. The deviation of the flow in -Z/+Z direction reaches maximum values of v = 0.0097 m/s at the arms. Velocity component w only varies at the stalk with a deviation in +Y direction of w = 0.0077 m/s.

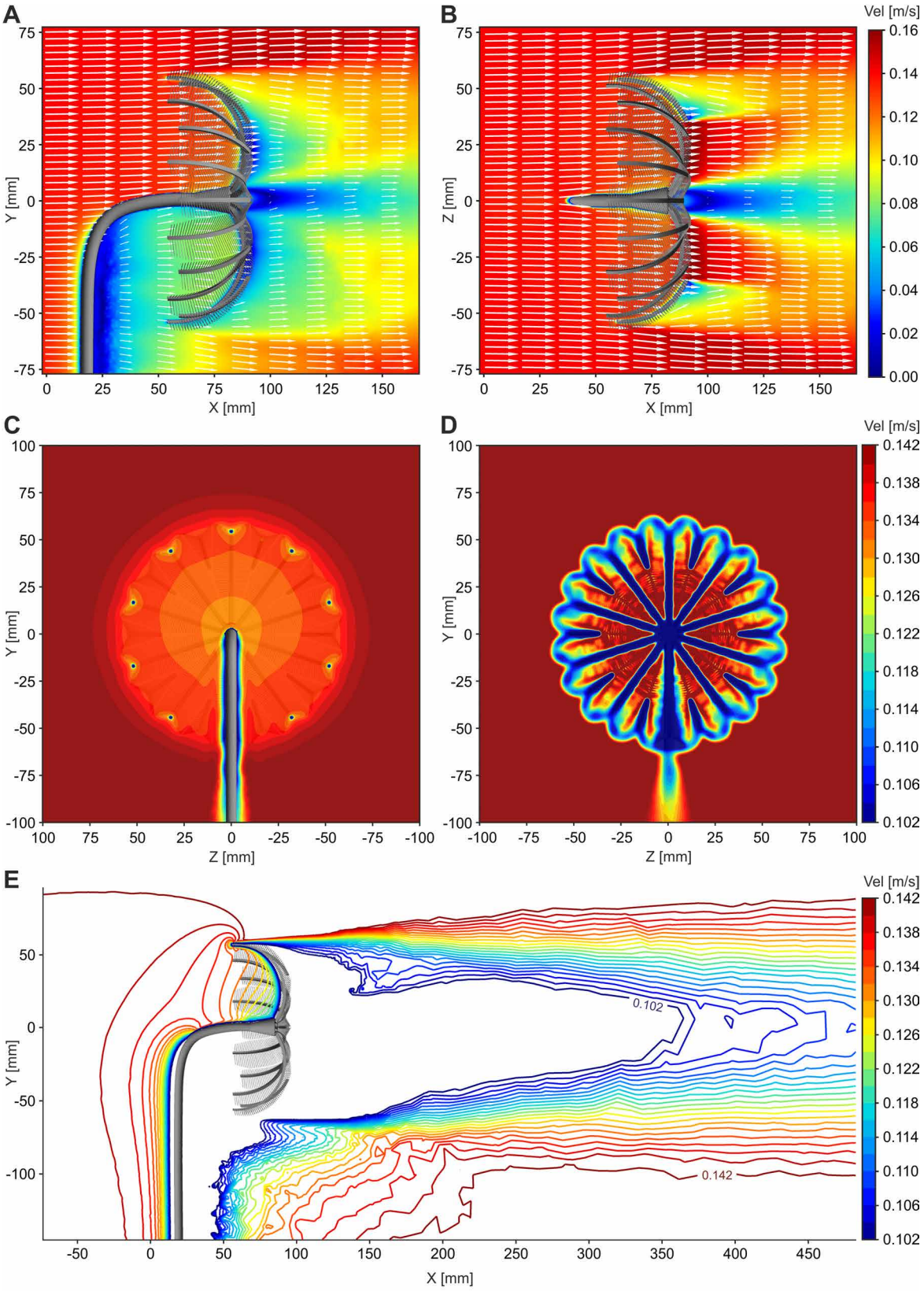

Figure 23: Results of flow analysis of the recent *N. decorus*. A: combined contour-vector plot on XY plane; B: combined contour-vector plot on ZX plane; C: contour plot on YZ plane at the beginning of the arms, D: contour plot on YZ plane at the end of the arms; E: contour lines on XY plane.

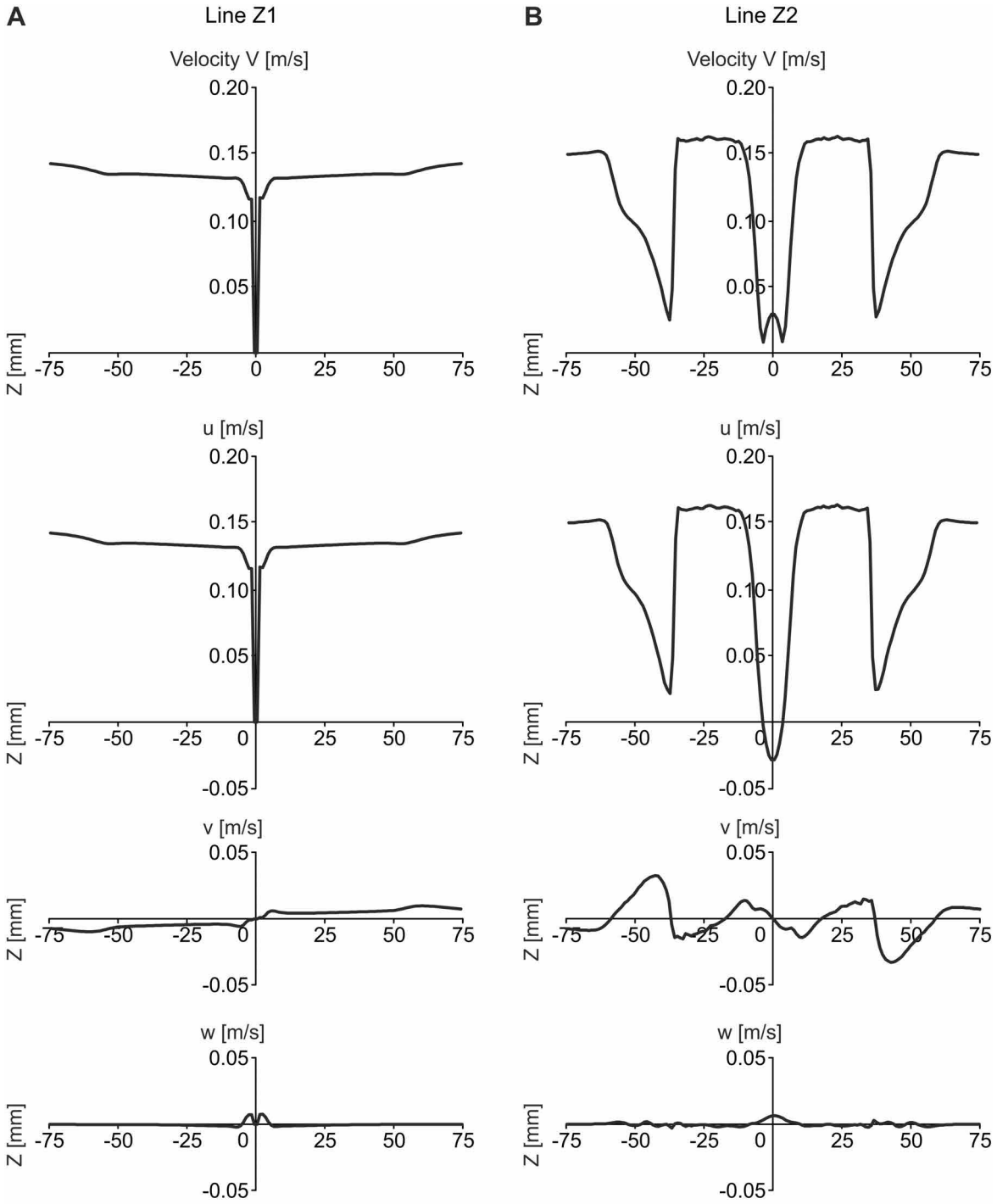

Figure 24: Linegraph plots of the total velocity and the three individual velocity components u, v and w in Z direction. A: Line Z1 at the beginning of the arms; B: Line Z2 at the end of the arms.

Directly behind the arms (Fig. 24B), the total velocity V decreases considerably at the arms down to V = 0.025 m/s (17.6 % of V_{init}). In the wake of the pinnules, V increases to values of V = 0.1633 m/s (representing 15 % higher values than V_{init}). At the stalk, V shows a decrease down to V = 0.0082 m/s (5.8 % of V_{init}), but increases again at Z = 0, which is a result of the recirculation zone forming behind the calyx and is apparent in the linegraph plot of velocity component u, here having negative values with a minimum of u = -0.0287 m/s.

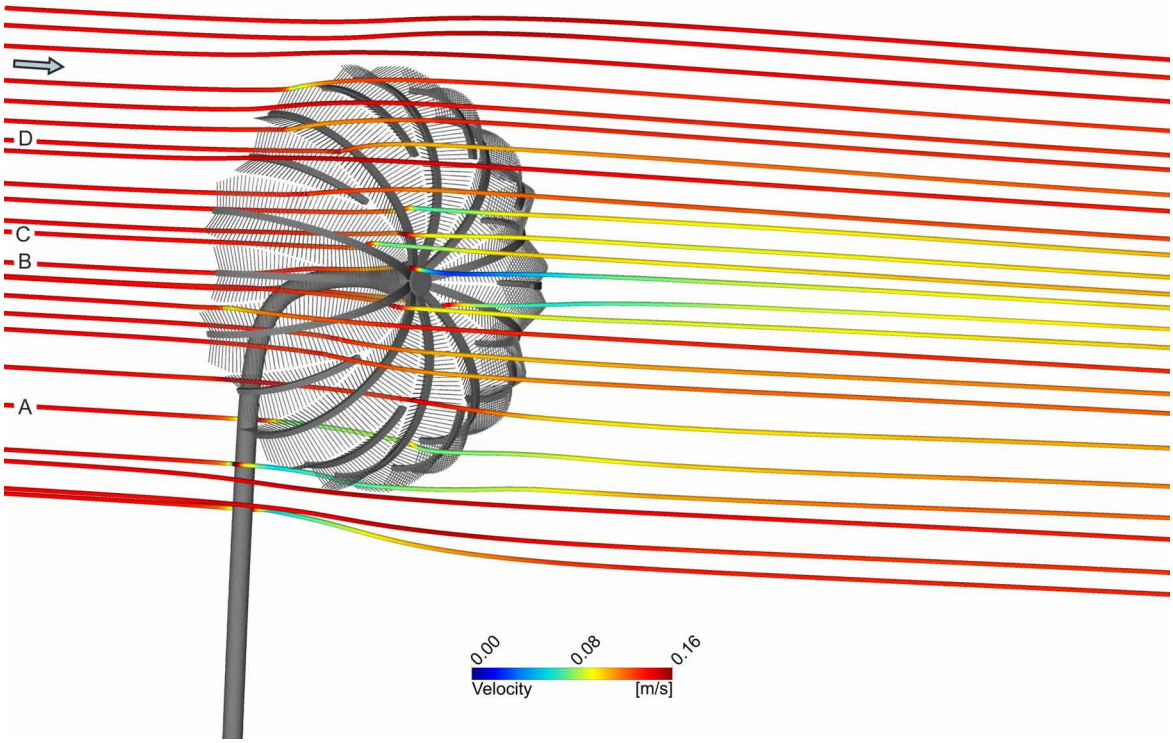

Figure 25: Trajectories of particles imitating plankton with a density of 1080 kg/m^3 and a diameter of 150 µm; labels indicate trajectories presented in Figure 26.

Velocity component v is influenced clearly by the presence of the crinoid arms and reaches maximum values of v = 0.0322 m/s. Behind the crown, the water movement parallel the Y axis is very small, and w only shows slight variations at the arms and a positive deviation at the stalk.

The particle tracking simulations reveal that particles with a density slightly higher than seawater and diameters of 150 µm move straight through the crown (Fig. 25). The particles are slowed down by the stalk, calyx, arms and pinnules, and some impact the filtering structures directly, which is recognizable by the abrupt colour change of the particle trajectories. Even the prominent recirculation zone existing behind the calyx does not transport any particles back onto the crown surface by recirculating water.

Figure 26 depicts the velocity profiles of 4 exemplary chosen particles, one passing the stalk (A), one the calyx (B), one an arm (C) and one a pinnule (D) (the corresponding trajectories are indicated in Fig. 25). All particles slow down some distance before reaching the crinoid, then speed up while passing the object, slow down again in the wake followed by an increase in velocity with increasing distance from the crinoid (except particle A). Particle A, passing the stalk, exhibits the highest speed-up on its path, first being slowed down to V = 0.094 m/s, followed directly by an increase in velocity to V = 0.187 m/s. The particle then slows down again to an even lower value of V = 0.0764 m/s, then speeds up slightly and then more abruptly while passing through the gaps between the pinnules of one of the lower

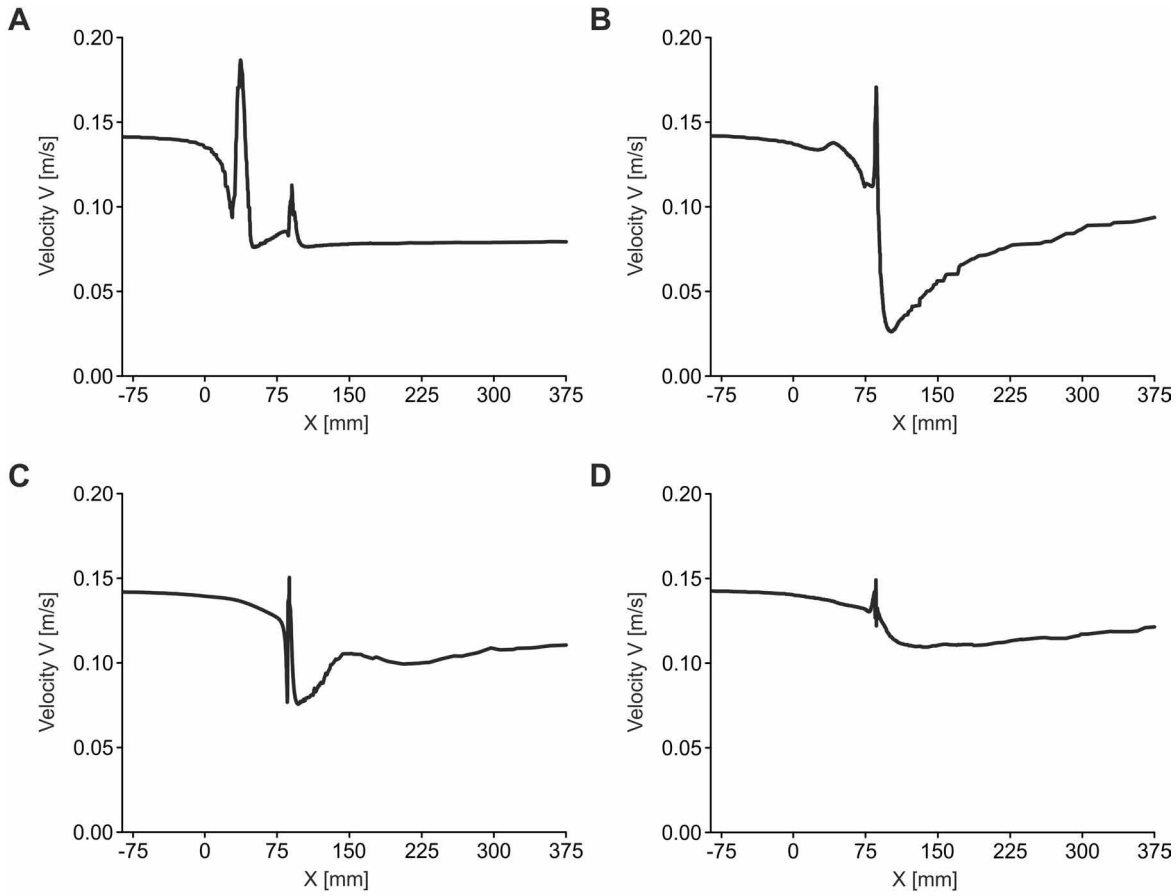

Figure 26: Total velocity of particles in X direction (corresponding trajectories marked in Figure 25). A: particle passing the stalk; B: particle passing the calyx; C: particle passing an arm; D: particle passing a pinnule.

arms of the crinoid. After leaving the filter, the particle maintains a constant velocity value of V = 0.12 m/s in the wake of the crinoid. Particle B, passing the calyx, first speeds up slightly at the beginning of the calyx, then slows down and by reaching the arms increases to a velocity of V = 0.1704 m/s, which is followed by the strongest velocity decrease of all four particle paths with values of V = 0.026 m/s, which is a result of the presence of the recirculation zone behind the calyx. Instead of being transported back to the oral surface, the particle keeps constantly moving in +X direction and gains velocity in the wake. The particle that passes the arm (C), slows down to V = 0.0766 m/s, speeds up to V = 0.1502 m/s, slows down again to V = 0.0755 m/s and exhibits slight variations in velocity in the wake of the crown. Particle D, passing the pinnule, shows the lowest variation in velocity values along its path. It slows down only slightly before reaching the pinnule, to values of V = 0.1296 m/s, then speeds up to V= 0.1461 m/s, slows down a second time reaching values of V = 0.126 m/s, speeds up to the highest velocity value with V = 0.1483 m/s and then slows down to V = 0.1087 m/s in the wake, where the particle velocity rises slowly and constantly with increasing distance from the crown.

4.2.3 Tube feet submodel

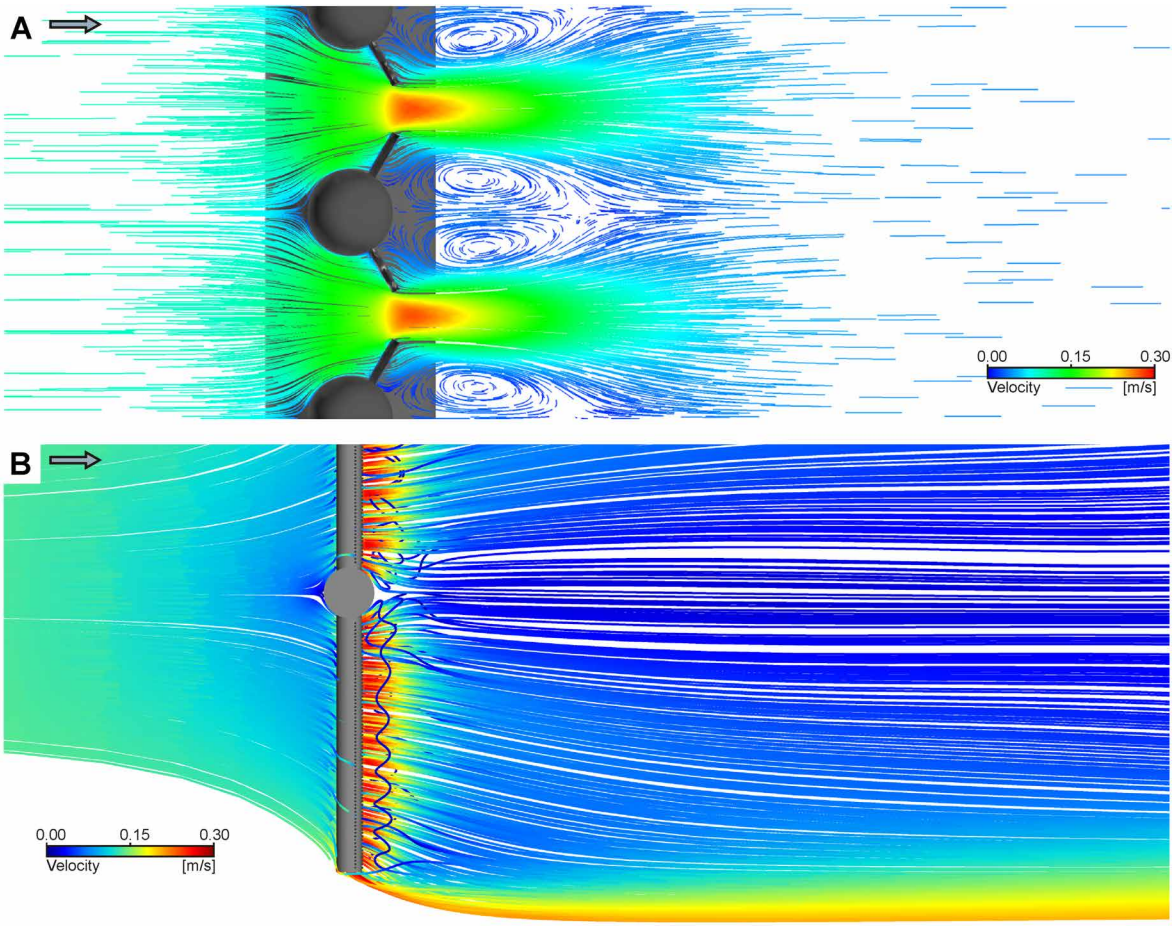

Figure 27: Results of flow analysis of the tube feet submodel for V_{init} = 0.142 m/s illustrated as vector and streamline plot. A: curved vector plot in side view; B: cut out section of streamline plot in top view.

The flow analysis of a submodel including the finer filtering structures of the tube feet shows that behind the model local recirculation flows develop, whereas the global flow direction stays unidirectional (Fig. 27). The eddies are generated behind the arm and pinnules, which is illustrated in Figure 27B, where a streamline passing the arm in close vicinity forms an eddy in its wake, and the streamline can then be followed undergoing several whorls while running alongside the pinnule.

The contour plots of the velocity in front of and behind the model provide an overview of the impact of the crinoid on the flow (Fig. 28). In front of the model (Fig. 28B), the slow-down diminishes from the centre of the model towards the tips of the pinnules. The strongest slow-down that is not caused by the arm but mainly by the pinnule, reaches values of V = 0.0746 m/s (accounting for 52.5 % of V_{init}). At the same Z coordinate, but in front of the gap between two adjacent pinnules, the water is slowed down to 0.1017 m/s (71.6 %). Behind the model, at Plane YZ2 (Fig. 28C), the increase in velocity in the gap

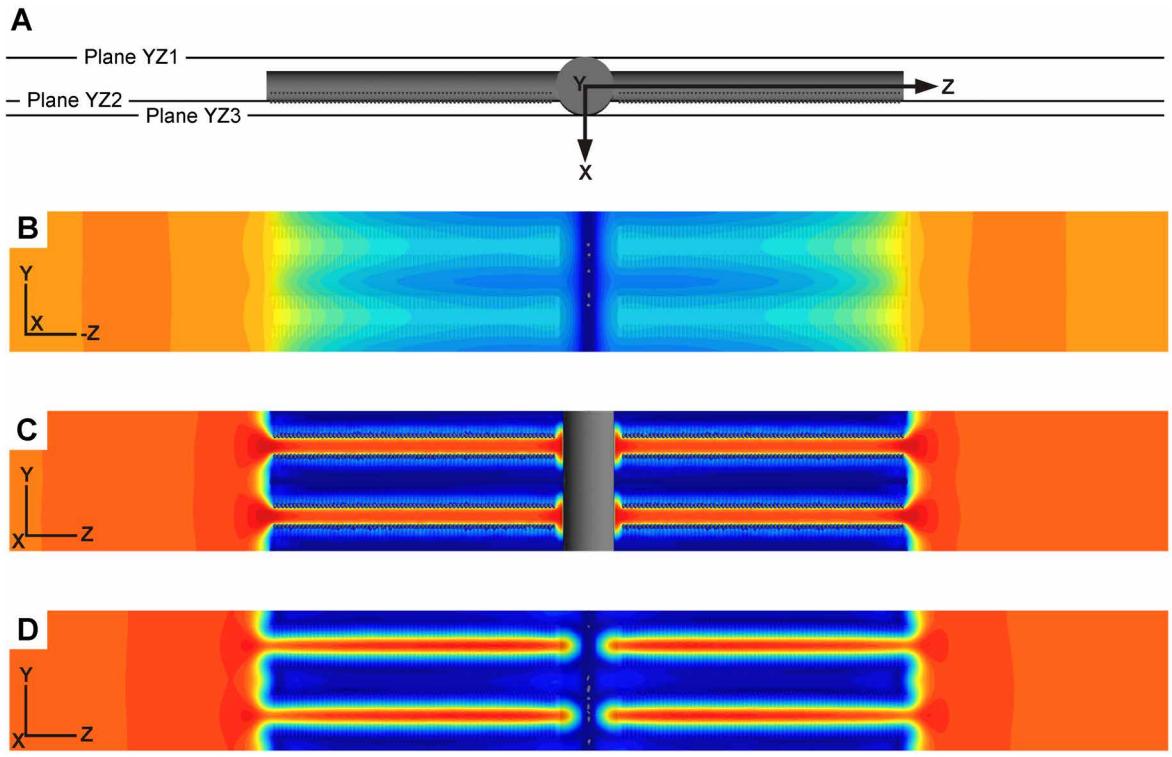

Figure 28: Contour plots illustrating the velocity distribution on YZ planes of the tube feet submodel for V_{init} = 0.142 m/s. A: location of planes in top view; B: Plane YZ1 (located at the beginning of the arm); C: Plane YZ2 (at the end of the pinnule); D: Plane YZ3 (at the end of the arm).

between adjacent pinnules is clearly visible. The local Reynolds number here takes values of Re = 43 (gap width = 0.54 mm and average V = 0.0951 m/s). Alongside the centre of the pinnules, where the food grooves are located, the water is slowed down to values of V = 0.0017 m/s (1.2 %), where component u contributes a recirculation velocity of u_{recirc} = -0.0015 m/s. At Plane YZ3 (Fig. 28D), the distribution of the velocity has merely changed, but here the recirculation is stronger with values of u_{recirc} = -0.015 m/s.

The linegraph plots of Line X1 (Fig. 29A, B) illustrate that the water velocity first increases slightly while entering the space between the pinnules, and then considerably by passing the gap between adjacent rows of tube feet, reaching velocities of up to V = 0.2749 m/s (193.1 %). This increase in velocity is only present for a short distance, due to a concurrent deviation of the water in -Y/+Y direction into regions with lower flow velocities in the wake of the model. Only a short distance away from the crinoid model, the flow in the wake is moving in a straight direction again, without showing large disturbances caused by the model, but being slowed down to values of V = 0.0365 m/s (25.7 %). Velocity component u does not take negative values at Line X1, so that here no recirculation flow develops.

Line X2 (Fig. 29C, D), which runs through the centre of the middle pinnule, shows a decrease in velocity in front of the model, with values of V = 0 m/s directly at the model (X = -0.5-0.5 mm). Behind the pinnule, V increases to V = 0.0346 m/s (24.4 %), decreases

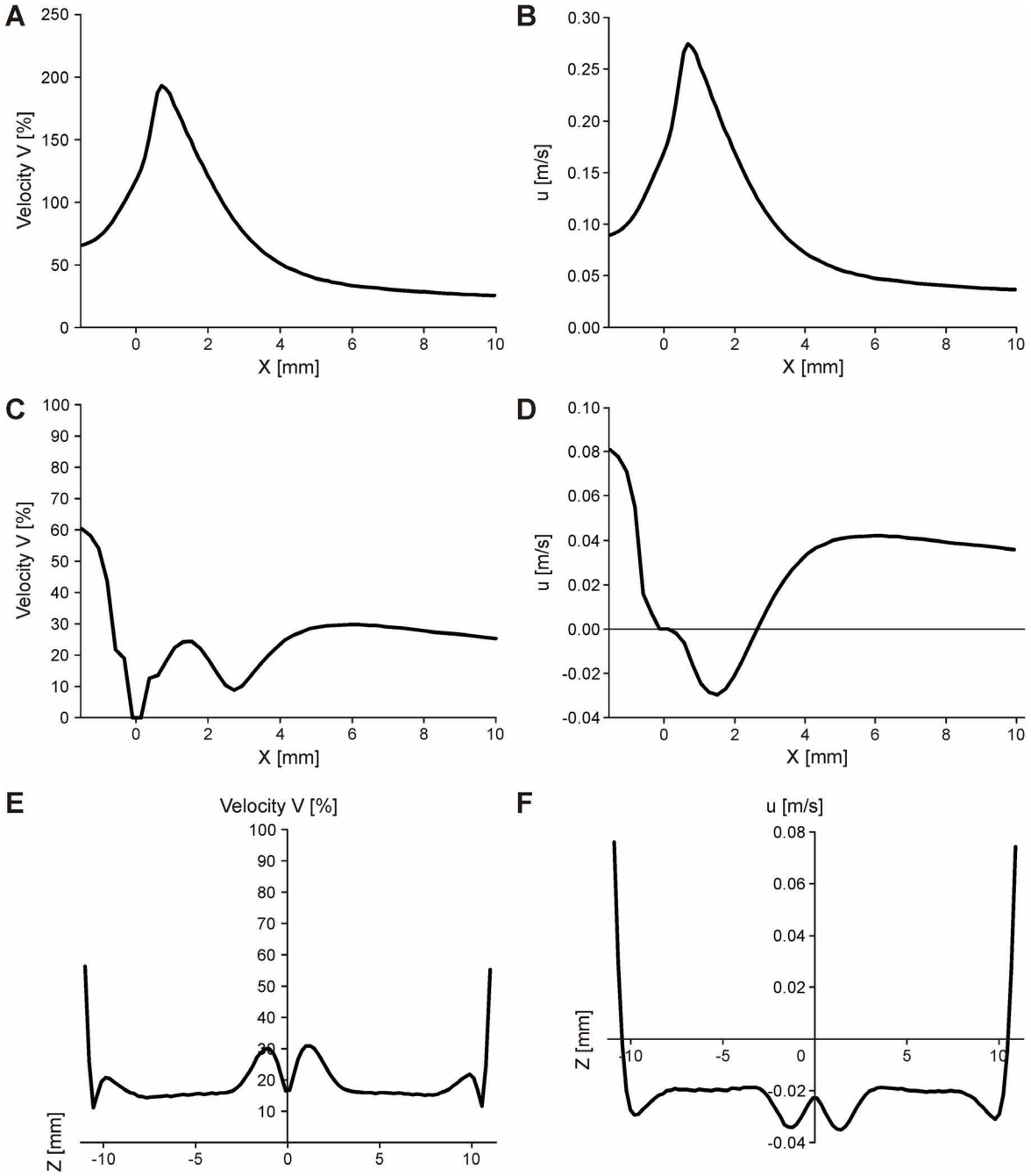

Figure 29: Velocity along lines illustrated as linegraph plots of the tube feet submodel for V_{init} = 0.142 m/s. A: Line X1, velocity in % of V_{init}; B: Line X1, component u; C: Line X2, velocity in % of V_{init}; D: Line X2, component u; E: Line Z1, velocity in % of V_{init}; F: Line Z1, component u.

to V = 0.0125 m/s (8.8 %), and increases again to V = 0.0424 m/s (29.8 %). Velocity component u reveals that the velocity increase directly behind the pinnule can be attributed to a recirculation zone that extends into the food groove. In a distance of about 1.5 mm behind the model, the strongest recirculation occurs with u_{recirc} = -0.0298 m/s. At Line Z1, V shows several alternations of velocity decreases and increases (Fig. 29E), which all correspond to negative peaks in u (Fig. 29F), where the recirculation reaches values of u_{recirc} = 0.0351 m/s close to the arm, and u_{recirc} = 0.031 m/s close to the end of the pinnules.

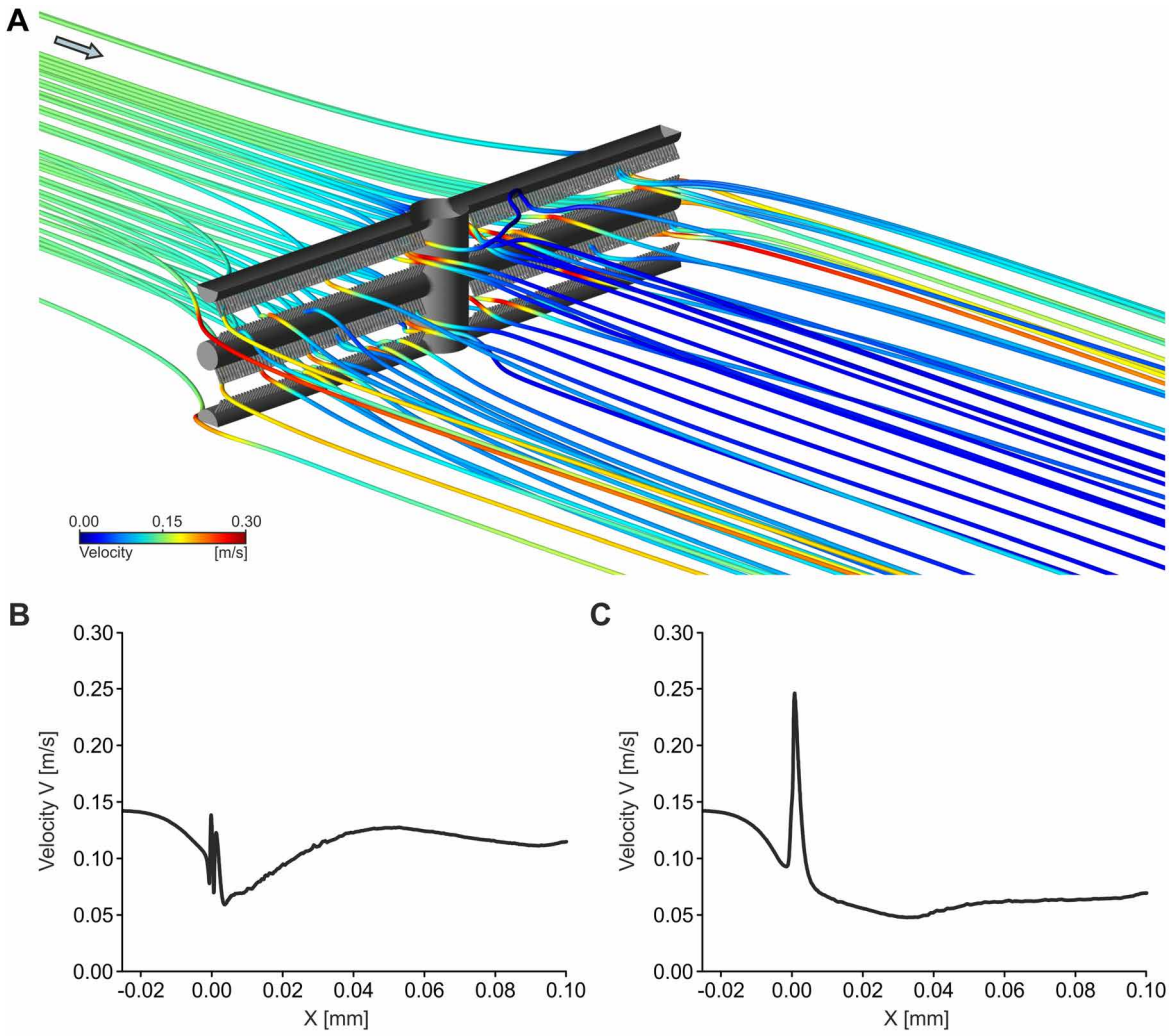

Figure 30: Results of particle tracking of the tube feet submodel for V_{init} = 0.142 m/s. A: particle trajectories; B: total velocity in X direction of one particle passing the middle pinnule; C: total velocity in X direction of one particle approaching the tube feet.

As the particle tracking simulations reveal, in the presented example only one out of 1000 injected particles is actually caught in a recirculation current and transported backwards into the direction of the model (Fig. 30A). This particle is approaching the centre of the pinnule, where the food groove is located, instead of touching the particle catching structures of the tube feet. Particles passing the pinnules are deviated to move through the small gap in between the tube feet, while particles approaching the tube feet move in between the gap between two adjacent rows of tube feet, without getting close to the food catching surface.

The velocity profile in Figure 30B illustrates the behaviour of a particle that first passes the middle pinnule, then is deviated in +Y direction and passes through the small gap in between two tube feet, where it slows down to a velocity of V = 0.0592 m/s. In Figure 30C, a particle first approaches the tube feet, but before it comes close to the surface, it is deviated and passes the gap between the pinnules and adjacent rows of tube feet, where it increases to a velocity of V = 0.2459 m/s.

4.2.4 *Encrinus liliiformis*

Inflow from aboral

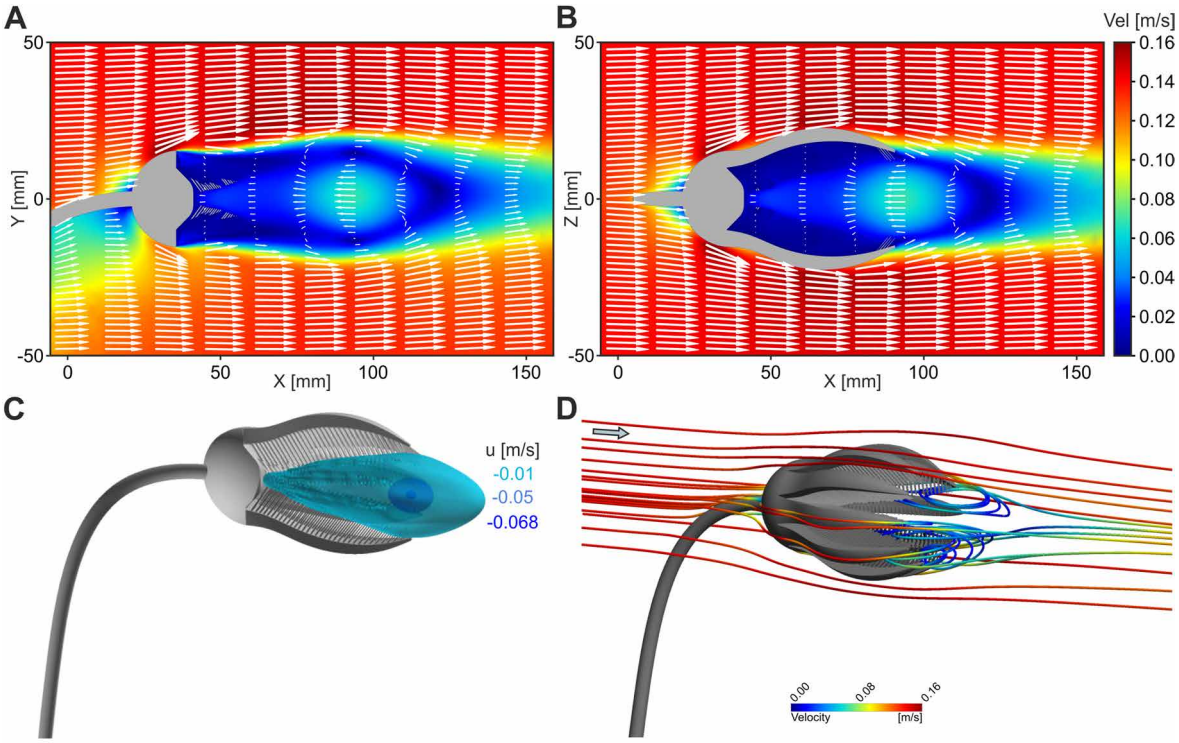

Figure 31: Results of flow analysis of *E. liliiformis* with full pinnulation for V_{init} = 0.14 m/s and aboral inflow. A: vector plot illustrating flow on ZX plane; B: vector plot illustrating flow on XY plane; C: isosurface plots of u_{recirc} illustrating the extent of the recirculation zone forming inside the crown; D: particle trajectories showing recirculation of plankton into the crown.

V_{init} = 0.14 m/s. The flow pattern of the expanded model of *E. liliiformis* with all arms pinnulated (10AP) and seawater as fluid in general conforms with the results of the simplified geometry used for the PIV-CFD comparison and studied under freshwater conditions. The tear shape of the crown leads to the formation of a recirculation zone inside and behind the crown (Fig. 31A, B). Compared to the simplified geometry, the recirculation centre shifts in +X direction and is now located directly behind the end of the arms, reaching considerably higher reciculation velocities with u_{recirc} = -0.0681 m/s (48.6 % of V_{init}).

The shape and strength of the recirculation zone are illustrated by isosurface plots of negative values of the velocity component u (Fig. 31C). These surfaces reveal that the recirculation extends well into the crown and reaches the tegmen with the centrally located mouth. The end of the recirculation in the wake is located 29.84 mm behind the tips of the arms. The particle tracking simulations show that 15 particles (Table 2, p. 49), which all pass the calyx in close vicinity, are caught in the recirculation current and directed back onto the oral surface of the crinoid (Fig. 31D). Some of these particles are then moving through

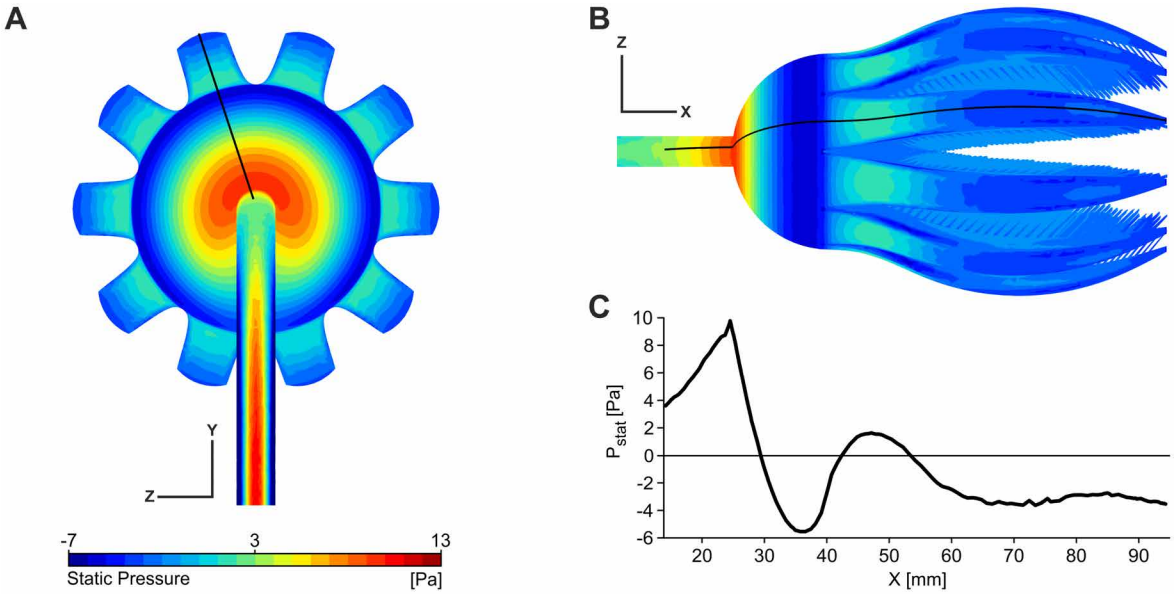

Figure 32: Static pressure distribution on the surface of model 10AP for V_{init} = 0.14 m/s and aboral inflow. A: contour plot, view in +X direction; B: contour plot, view in -Y direction; C: line graph plot with p_{stat} plotted against X, position indicated by black line in A and B.

the space between adjacent pinnules. The zone, where the water is slowed down behind the model is relatively confined and already about 200 mm behind the end of the object the water almost approaches the freestream velocity of 0.14 m/s.

The pressure distribution (Fig. 32) shows that the maximum pressure on the crown occurs at the calyx directly above the insertion of the stalk with values of p_{stat} = 9.77 Pa. Following the outline of the crown, the pressure reaches minimum values at the widest calyx diameter with p_{stat} = -5.55 Pa, then increases to p_{stat} = 1.62 Pa where the arms curve outward and show a gentle fillet, and then decreases again to reach negative values decreasing constantly along the arm. Here, the curve progression reveals slight disturbances in p, but the flow, however, stays attached to the crinoid and flow separation occurs a few millimeters before the tips of the arms.

The comparison of the velocity distribution of the four different models of *E. liliiformis* shows slight variations in the flow field. Figure 33 displays the linegraph plots of the absolute velocity V and the three individual velocity components along Line X1 for all alternatives of the geometry. The curve progressions of the absolute velocity in general equal each other, reaching almost 20 % of V_{init} close to the tegmen, followed by a slight decrease (except model 7A) and then increase to the highest values (around 50 %) near the tips of the arms, which end at X = 99 mm, followed again by a decrease down to around 5 % indicating the end of the recirculation zone, and a subsequent increase of the flow velocity in the wake of the crown where the water speeds up continuously (Fig. 33A). The evaluation of the individual velocity components (Fig. 33B-D) illustrates the differences between the models

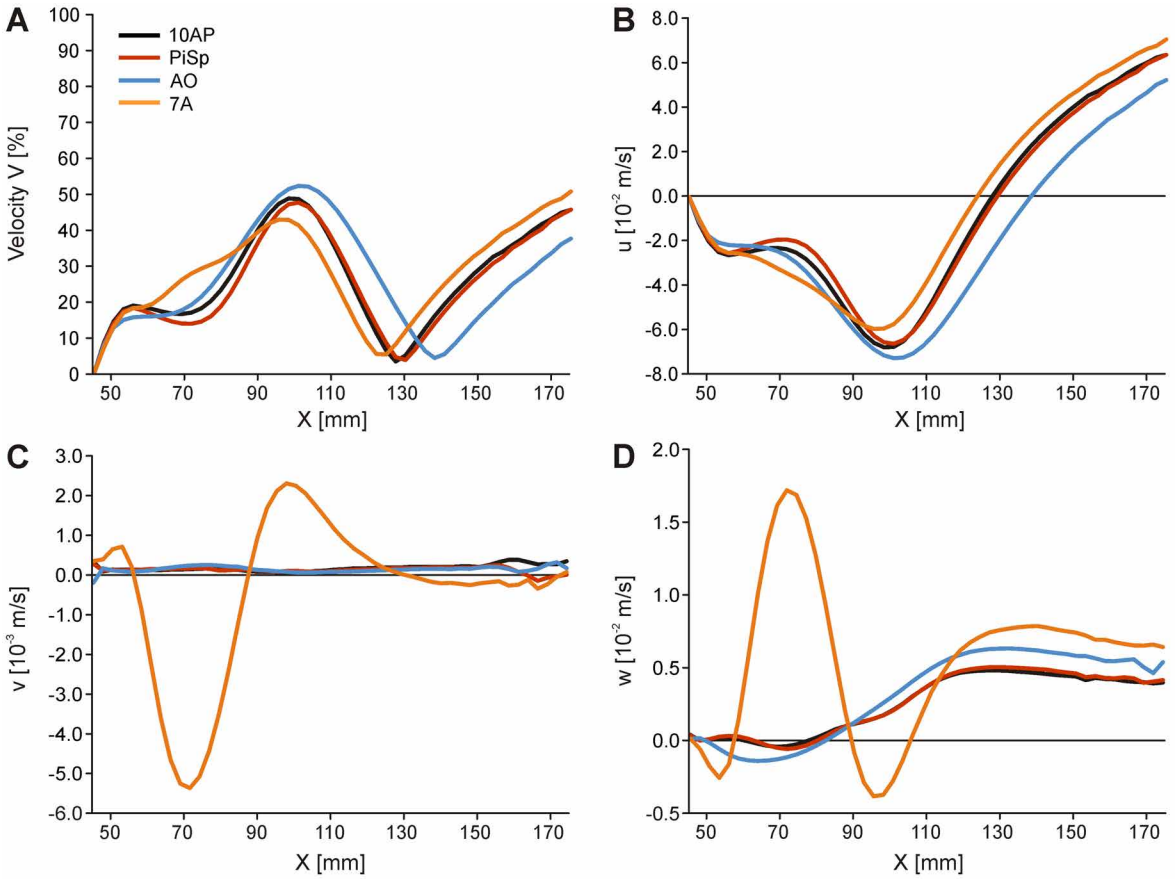

Figure 33: Velocity values for the expanded models of *E. liliiformis* at Line X1 for V_{init} = 0.14 m/s and aboral inflow. A: total velocity V in % of V_{init}; B: component u; C: component v; D: component w.

in more detail: while the spreading of pinnules (PiSp) has only little effect compared to the base model (10AP), the opening of the arms (AO) results in an elongation of the recirculation zone in X direction, ending 40.46 mm behind the tips of the arms, and higher negative peak values of u_{recirc} = -0.0729 m/s, while the loss of parts of 3 arms (7A) leads to a shift of the recirculation zone into the crown and a decrease of negative peak values of u (Fig. 33B).

Velocity component v (Fig. 33C) generally varies little along Line X1, only the model with 7 complete arms has a considerable effect on the crosswise deviation of the flow with a maximum deflection in -Z direction at X = 72 mm with v = -0.0054 m/s and a second lower peak in +Z direction at X = 100 mm with v = 0.0021 m/s. Velocity component w (Fig. 33D) shows generally a larger variation thus leading to higher deviation of the flow along the Y axis, reaching the highest values in the wake of the crown for all models except 7A. While the base model 10AP and the model PiSp again do not show apparent differences, model AO evokes a slightly higher deviation of the water along the Y axis and the flow of model 7A develops clear amplitudes at the same X positions where the highest peaks in velocity component v appear, with w = 0.0172 m/s in +Y direction and w = -0.0039 m/s in -Y direction.

The isosurfaces of the negative u values of model AO show the enlargement of the re-

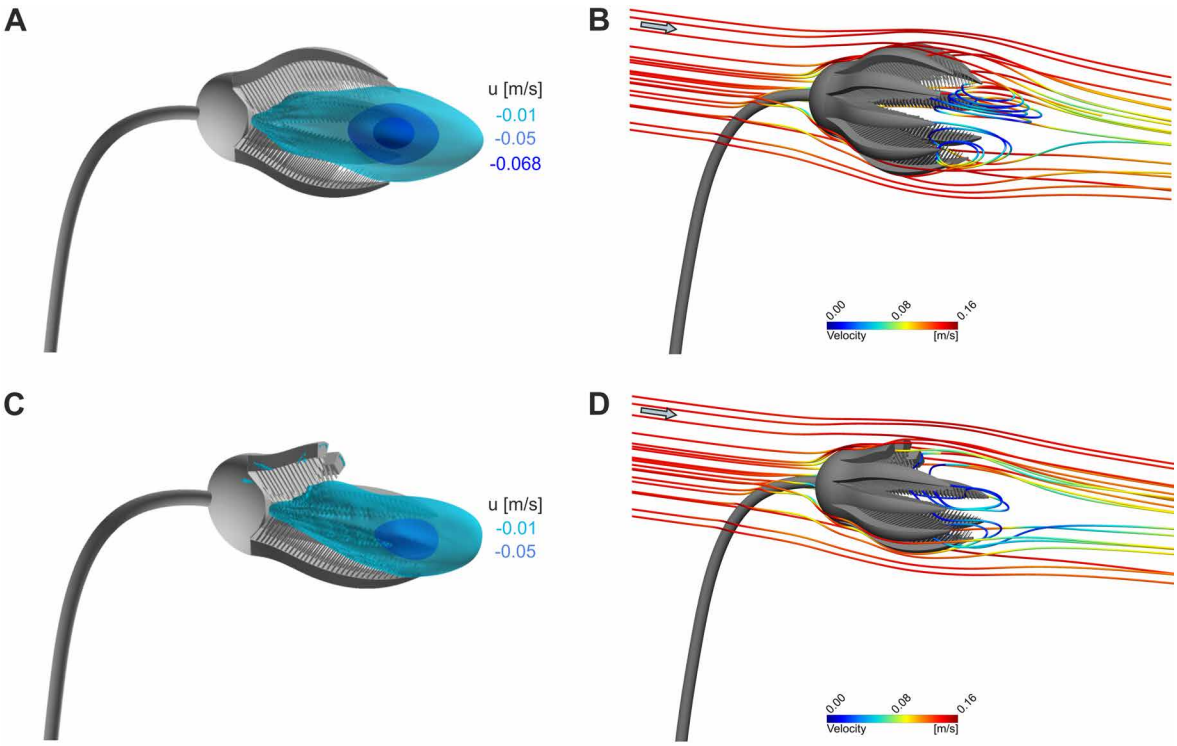

Figure 34: Isosurface plots and particle trajectories of the expanded models of *E. liliiformis* for V_{init} = 0.14 m/s and aboral inflow. A+B: model AO; C+D: model 7A.

circulation zone in all three dimensions and the increased recirculation velocity (Fig. 34A). The opening of the arms increases the number of recirculating particles to 34 (Table 2), as well as it increases the number of turns the particles perform (Fig. 34B). The isosurfaces of model 7A reveal that with parts of some arms missing, the recirculation zone is flattened in the upper part and the maximum reached negative u values decrease (Fig. 34C). The particle trajectories of model 7A show that the recirculating current is sufficient to redirect 11 of the particles back onto the oral surface (Fig. 34D, Table 2). Most of these particles, however, leave the inside of the crown through the gap on the upper side without approaching the oral surface closely.

Following the path of one exemplary particle illustrates the effect of altering the base geometry on the potential food source in more detail (Fig. 35). In the flow simulation of model 10AP, the particle performs one loop inside the crinoid crown (Fig. 35A). On its path,

Table 2: Minimum reached u_{recirc} along Line X in % of V_{init} and number (#) of reciculating particles

V_{init}	0.03 [m/s]		0.14 [m/s]		0.50 [m/s]	
	u_{recirc}	#	u_{recirc}	#	u_{recirc}	#
10AP	23.70	5	48.63	15	63.72	17
PiSp	24.39	6	47.45	16	53.80	10
AO	26.12	13	52.07	34	71.19	27
7A	22.06	5	42.68	11	50.94	13

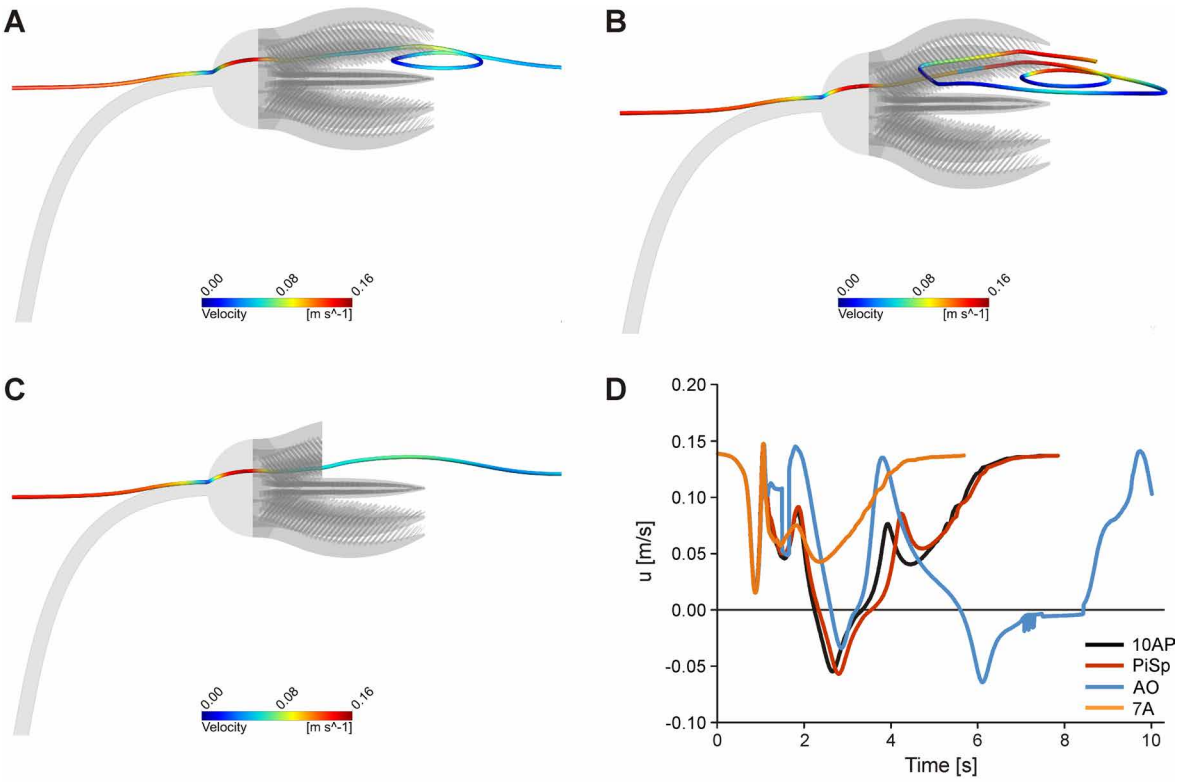

Figure 35: Path of one particle followed for the different models of *E. liliiformis* for V_{init} = 0.14 m/s and aboral inflow. A: particle trajectory of model 10AP; B: particle trajectory of model AO; C: particle trajectory of model 7A; D: recirculation velocity u plotted against time.

the particle exhibits several intervals of decreasing and increasing velocity with maximum reached velocity values of 65 % of V_{init} after passing the calyx and before entering the recirculation zone. The occurrence of one loop is visible in velocity component u that reaches negative values in one peak (Fig. 35D). The particle needs 7.7 s to pass the computational domain. A similar behaviour can be observed in model PiSp, where the particle needs slightly more time with 7.8 s (Fig. 35D). Model AO leads to an increase in the number of loops the particle performs (Fig. 35B), and higher velocity values before entering the recirculating current, reaching values of 102 % of V_{init} before the first loop and 95 % before the second loop. Due to the increased number of recirculation loops, velocity component u reaches negetive values in two peaks (Fig. 35D) and after 10 s the particle is still moving in the recirculation current and has not passed the complete computational domain. In model 7A, the particle does not recirculate at all (Fig. 35C), so that velocity component u has only positive values and the particle needs only 5.7 s to pass through the computational domain (Fig. 35D).

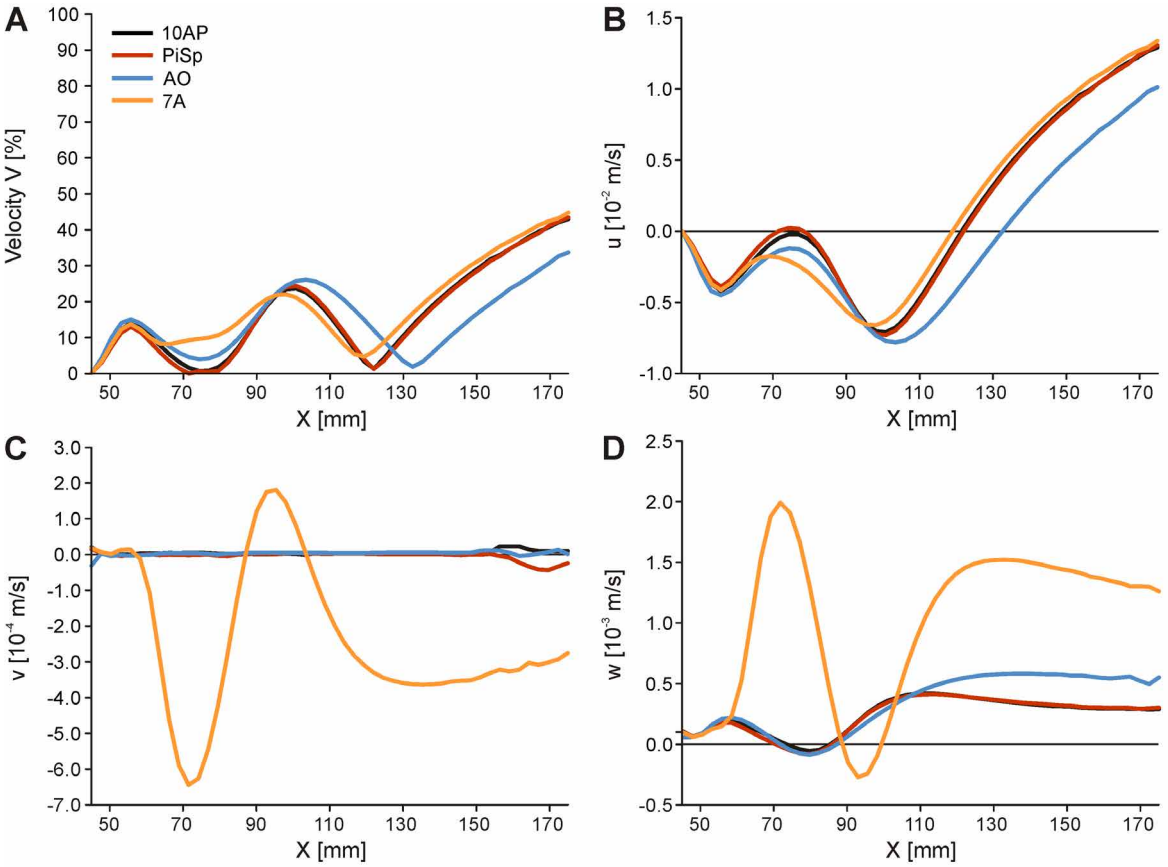

Figure 36: Velocity values at Line X1 for the different models of *E. liliiformis* for V_{init} = 0.03 m/s and aboral inflow. A: total velocity V in % of V_{init}; B: component u; C: component v; D: component w.

V_{init} = 0.03 m/s. A decrease in V_{init} results in a general weakening of the recirculation compared to V_{init} = 0.14 m/s (Table 2, p. 47). The velocity line graph plots of all geometries show similar curve progressions with two peaks, one reaching about 15 %, the second 25 % of V_{init} (Fig. 36A). The results of the total velocity V of model 7A do not differ considerably from the othe three models. Velocity component u (Fig. 36B) still gains negative values, with u_{recirc} = -0.0071 m/s for model 10AP. An opening of the arms results in a slightly increased recirculation velocity compared to the base model 10AP with values of u_{recirc} = 0.0078 m/s, and a small shift of the recirculation centre in +X direction. Velocity component v varies only considerably in model 7A (Fig. 36C), while velocity component w oscillates inside the crown, with the largest values reached in model 7A (Fig. 36D).

At V_{init} = 0.03 m/s, only five of 1000 injected particles are caught in the recirculation current, and only one of these particles approaches the pinnules and thus filtering surface. At a velocity of V_{init} = 0.01 m/s, none of the injected particles recirculates anymore. As could already be observed at V_{init} = 0.14 m/s, the opening of the arms raises the number of recirculating particles, here to a total of 13. Following the path of one particle for the four models shows that the effect of altering the morphology on the particle velocity is not as strong as at V_{init} = 0.14 m/s (Fig. 37A-E). The static pressure distribution along the outline of the crown

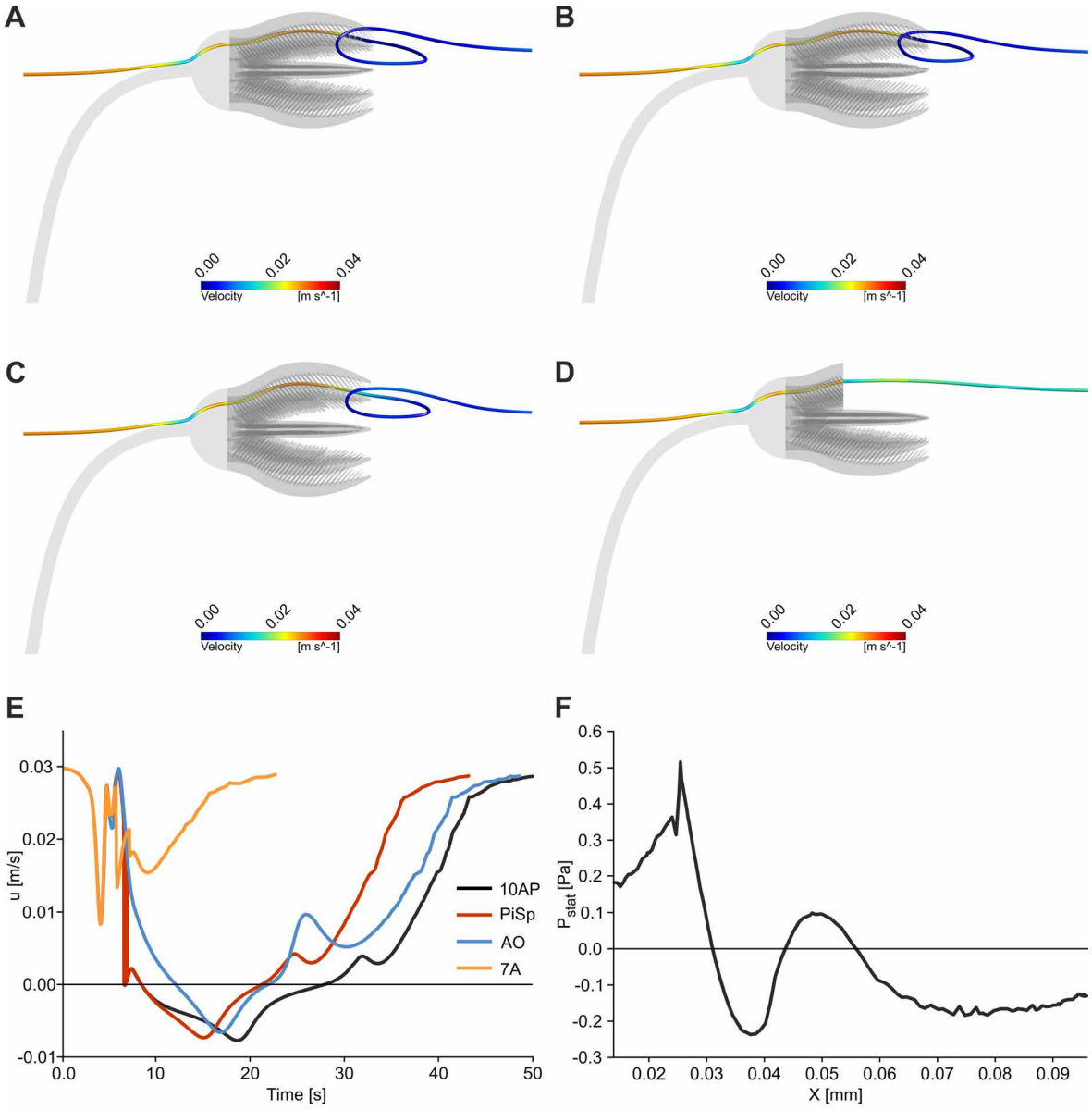

Figure 37: Path of one particle followed for the different models of *E. liliiformis* and static pressure for V_{init} = 0.03 m/s and aboral inflow. A: particle trajectory of model 10AP; B: particle trajectory of model PiSp; C: particle trajectory of model AO; D: particle trajectory of model 7A; E: u_{recirc} plotted against time; F: p_{stat} of model 10AP plotted against X.

is generally similar to the distribution observed at V_{init} = 0.14 m/s, with maximum values of p_{stat} = 0.52 Pa and minimum values of p_{stat} = -0.24 Pa (Fig. 37F). Only along the arms the flow behaviour differs from V_{init} = 0.14 m/s with a constant increase instead of a decrease in p_{stat} before the flow separates at the tips of the arms.

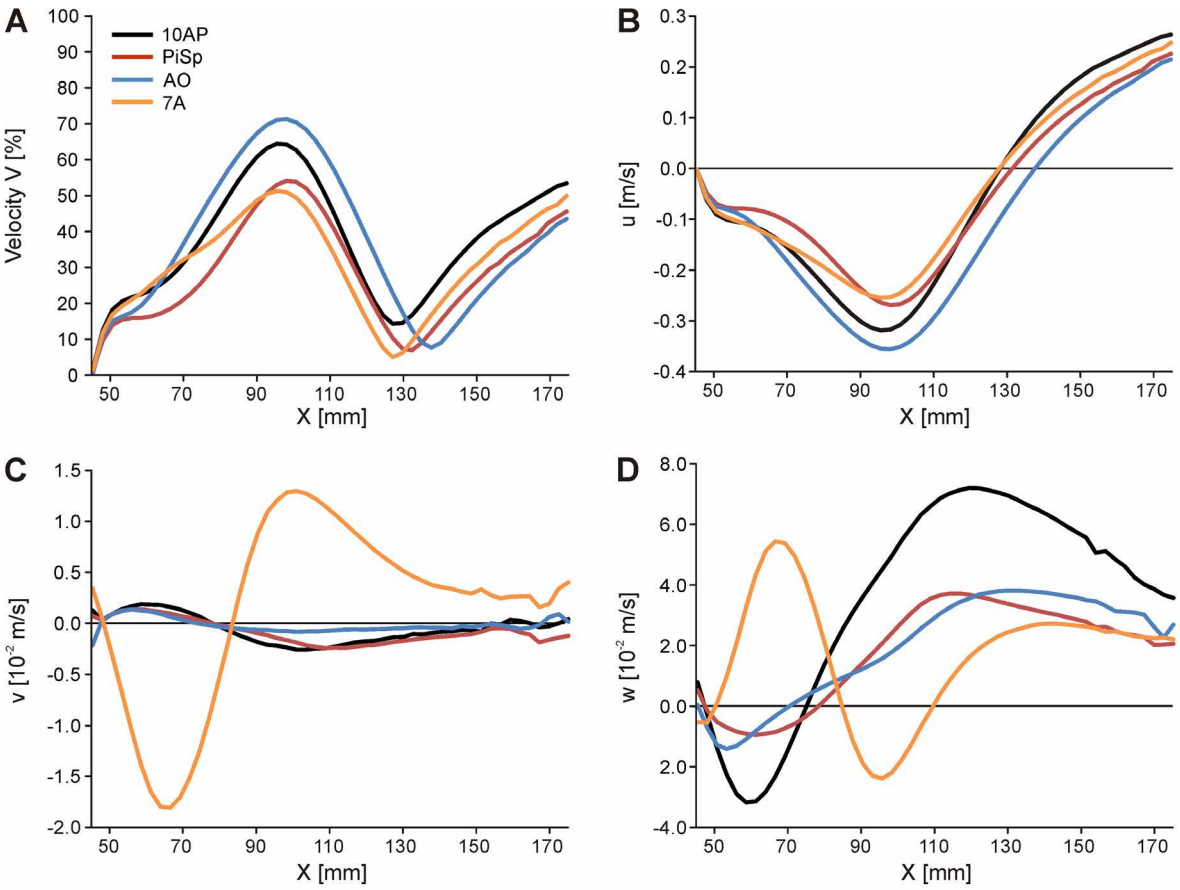

Figure 38: Velocity values at Line X1 for the different models of *E. liliiformis* for V_{init} = 0.50 m/s and aboral inflow. A: total velocity V in % of V_{init}; B: component u; C: component v; D: component w.

V_{init} = 0.50 m/s. An increase in V_{init} results in a general intensification of the recirculation compared to V_{init} = 0.14 m/s (Table 2, p. 47). With an inflow velocity of 0.50 m/s, the differences in the velocity distribution between the various geometries increase (Fig. 38A-D). The base model 10AP reaches V values of around 60 %, the opening of the arms slightly higher values of around 70 % (Fig. 38A). The spreading of the pinnules leads to similar decreased values of V as the loss of parts of three arms, both reaching about 50 % of V_{init} at the end of the arms. The same pattern can be observed in velocity component u (Fig. 38B) with maximum recirculation velocities of u_{recirc} = 0.3559 m/s for model AO. The variation of the flow in Z direction is generally higher compared to the other inlet velocities for all geometries (Fig. 38C), and velocity component w now shows large deviations along the Y axis inside as well as behind the crown (Fig. 38D).

The particle tracking simulations show that with model 10AP and 7A slighlty more particles are captured in the recirculating current compared to V_{init} = 0.14 m/s (Table 2, p. 47) but the duration time of the particles inside the crown is decreased due to their higher velocities (Fig. 39E). For model PiSp, the number of recirculating particles decreases to 10, and the increase in particles in model AO is not as high as at V_{init} = 0.14 m/s, with a total

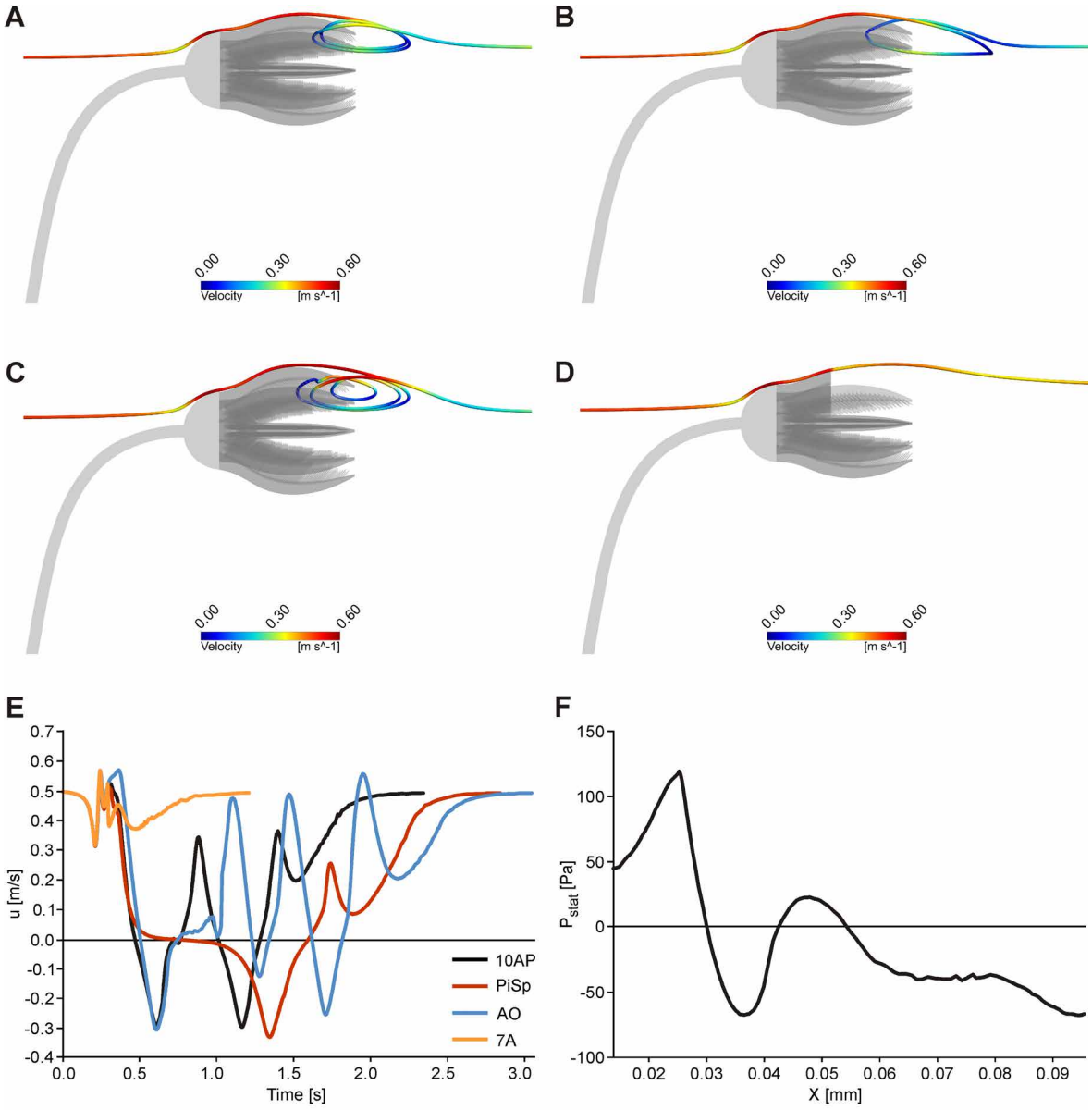

Figure 39: Path of one particle followed for the different models of *E. liliiformis* and static pressure for V_{init} = 0.50 m/s and aboral inflow. A: particle trajectory of model 10AP; B: particle trajectory of model PiSp; C: particle trajectory of model AO; D: particle trajectory of model 7A; E: u_{recirc} plotted against time; F: p_{stat} of model 10AP plotted against X.

of 27 particles. The comparison of one particle reveals that it performs two loops in the base model 10AP (Fig. 39A), one loop in model PiSp (Fig. 37B), three loops in model AO (Fig. 39C) and no loop in model 7A (Fig. 39D). The pressure shows a similar curve progression as at V_{init} = 0.14 m/s, with maximum values of p_{stat} = 119.13 Pa and minimum values of p_{stat} = -67.75 Pa (Fig. 39F). Only the decrease in pressure towards the end of the arms is stronger, so that the point of flow separation moves upstream and the flow separates sligthly earlier compared to V_{init} = 0.14 m/s.

Inflow from lateral

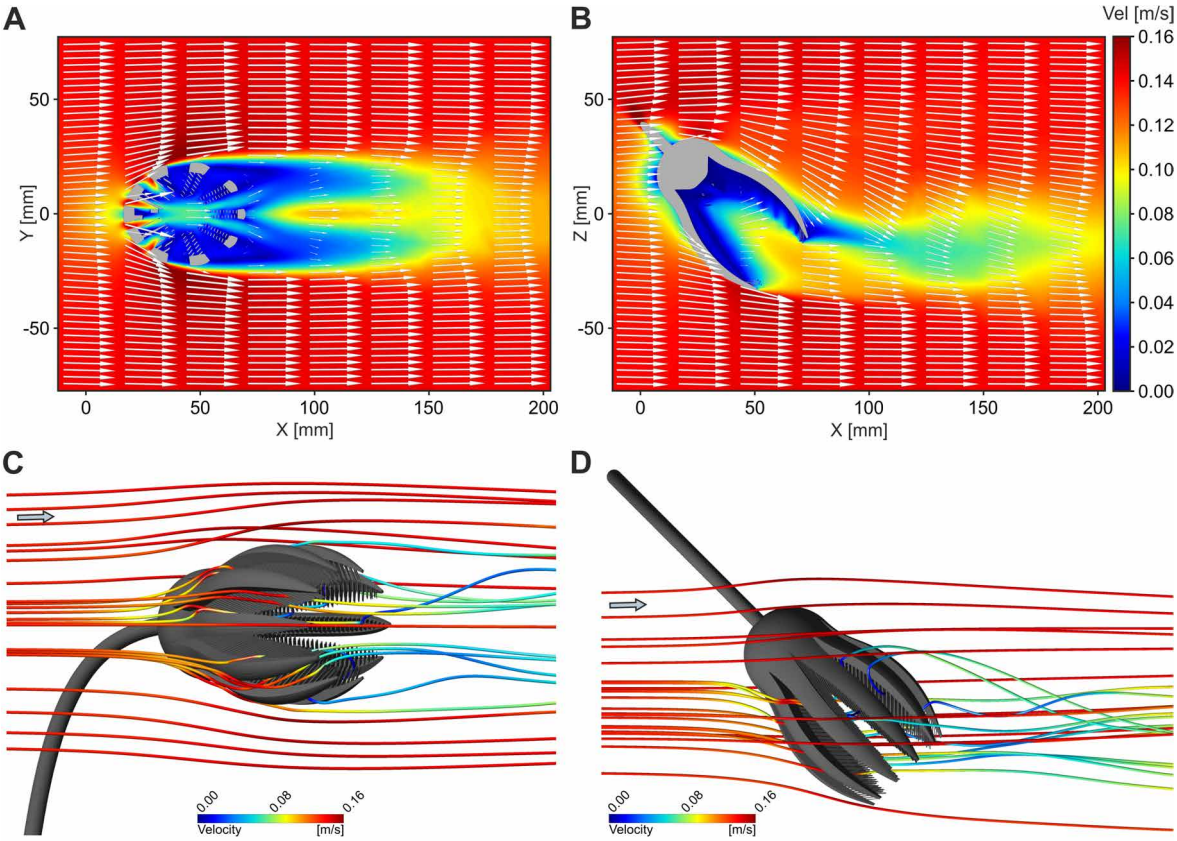

Figure 40: Results of flow analysis of *E. liliiformis* with 10 arms pinnulated for V_{init} = 0.14 m/s and lateral inflow. A: combined contour-vector plot on YZ plane; B: combined contour-vector plot on ZX plane; C: particle trajectories in lateral view; D: particle trajectories in top view.

V_{init} = 0.14 m/s. The change of the model orientation by a rotation of 45° around the Z axis shows a relatively unidirectional flow through the crown (Fig. 40). Inside the crown and in its wake, the flow pattern is irregular in shape and high velocity gradients develop at the filtering structures facing the incoming water. Inside the crown, the flow is slowed down at the pinnules, but in relation to V_{init}, reaches relatively high values in the centre close to the opening of the arms with velocities of V = 0.10 m/s. Downstream of the calyx, the flow is deviated and the vectors follow the outline of the arms without a considerable decrease in flow velocity (Fig. 40B).

The particle tracking simulations show, however, that some of the particles change their direction inside the crown and pass in between the pinnules during the turn they perform (Fig. 40C, D). Many of the particles reach the crown without a considerable decrease in velocity and impact on the pinnules. Other particles reach the arms, are deviated and then transported with lower velocities into the space between the pinnules. Some of the particles first approach the upstream pinnules and on their further path also reach the downstream

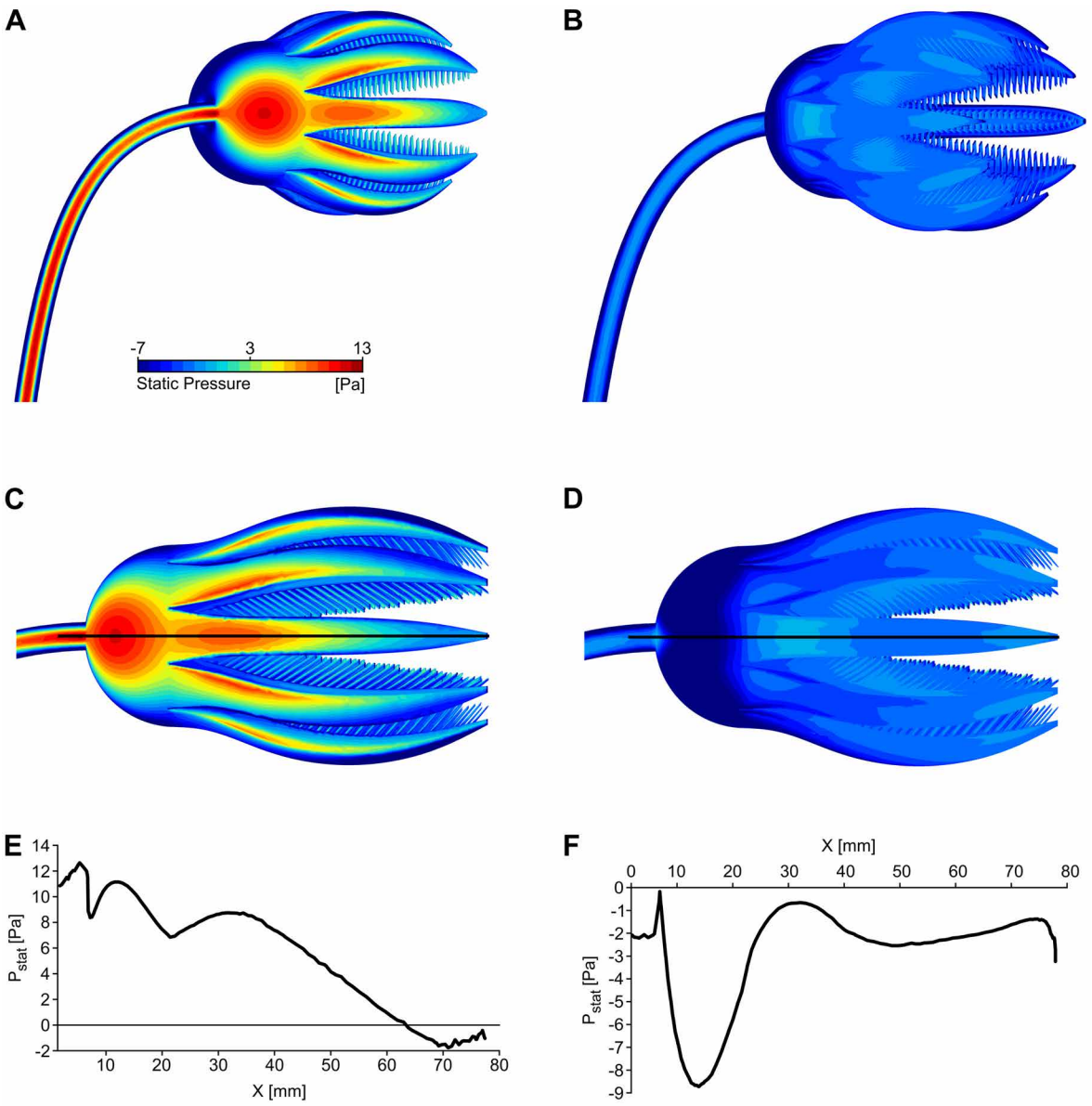

Figure 41: Static pressure distribution on the surface of model 10AP for V_{init} = 0.14 m/s and lateral inflow. A: contour plot, view in downstream direction; B: contour plot, view in upstream direction; C: contour plot, view in local Z direction; D: contour plot, view in local -Z direction; E and F: line graph plots with p_{stat} plotted against local X, position indicated by black lines in C and D.

located pinnules thus being in close vicinity to the filtering structures two times.

The distribution of the static pressure on the surface of the crinoid (Fig. 41) illustrates that three pressure peaks exist at different locations: the highest values occur on the stalk (p_{stat} = 12.64 Pa), followed by the calyx (p_{stat} = 11.15 Pa) and the proximal parts of the arms (p_{stat} = 8.75 Pa). On the downstream side of the crinoid, the static pressure is generally negative and reaches minimum values of p_{stat} = -8.73 Pa at the calyx. The difference in static pressure between the upstream and downstream surfaces of the crown is thus relatively high, reaching maximum values of p_{stat} = 19.67 Pa at the calyx (X = 13 mm).

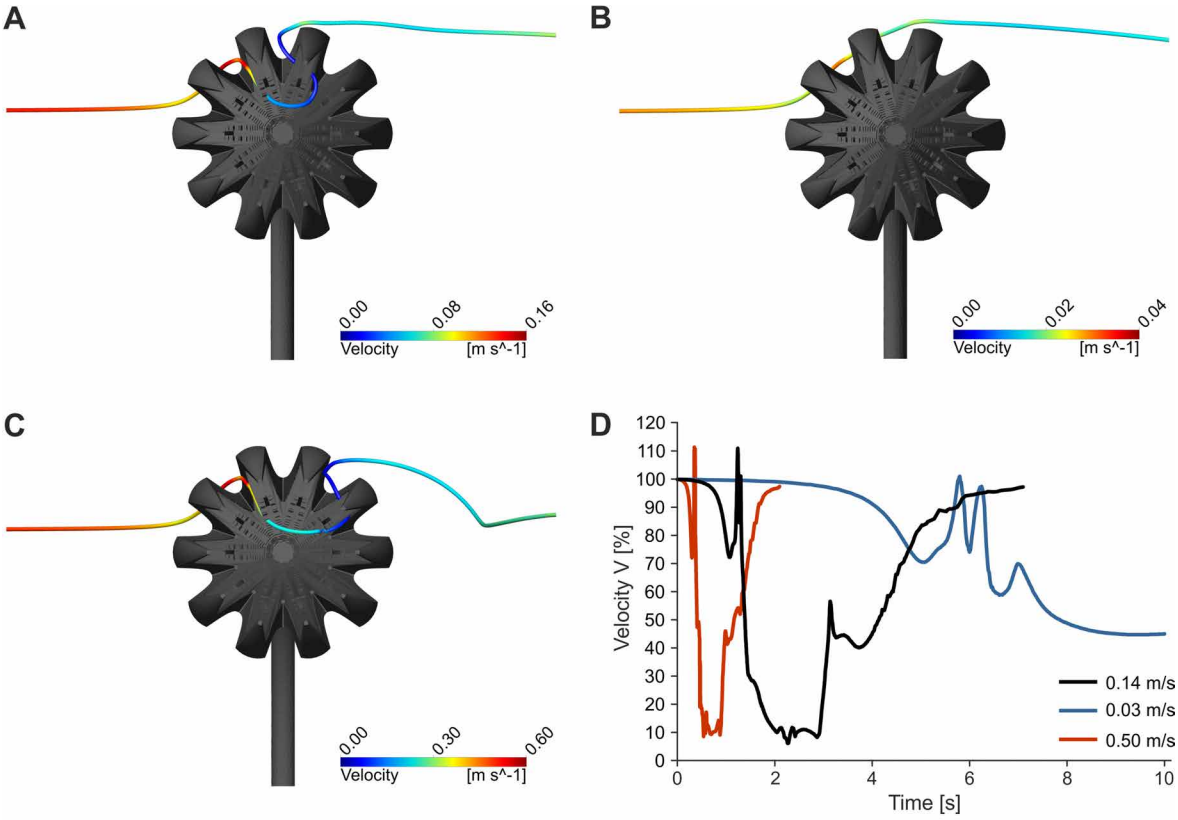

Figure 42: Particle behaviour of the same particle at different V_{init} of model 10AP and lateral inflow. A: particle trajectory at V_{init} = 0.14 m/s; B: particle trajectory at V_{init} = 0.03; C: particle trajectory at V_{init} = 0.50 m/s; D: linegraph plots of the particle velocity V in % of V_{init} plotted against time.

V_{init} = 0.03 m/s. The decrease in inflow velocity does not change the general distribution of the static pressure on the crinoid surface, but the difference between the upstream and downstream facing surfaces is relatively lower with values of p_{stat} = 0.92 Pa at the calyx. The particle tracking simulations reveal that some of the particles which enter and move through the filtering structures at V_{init} = 0.14 m/s, show a different behaviour. The same particle that describes a curve inside the crown and passes through the pinnules twice (Fig. 42A), does not enter through the gap in between the arms but instead is deviated around the crown (Fig. 42B). Generally, the number of particles that approach the oral surface and thus are likely to be captured, is decreased compared to the higher velocities.

V_{init} = 0.50 m/s. An increase in inflow velocity results in relatively higher static pressure differences developing between the upstream and downstream side of the crown, while the general distribution of p_{stat} is analogous to the ones observed at the other inflow velocities. The maximum difference in static pressure reaches values of p_{stat} = 257 Pa at the calyx. The particles show a similar behaviour compared to V_{init} = 0.14 m/s (Fig. 42C), but pass through the computational domain in a much shorter time (Fig. 42D). While the particle at V_{init} = 0.14 m/s needs 7.1 s, the same particles needs only 2.1 s at V_{init} = 0.50 m/s.

Inflow from oral

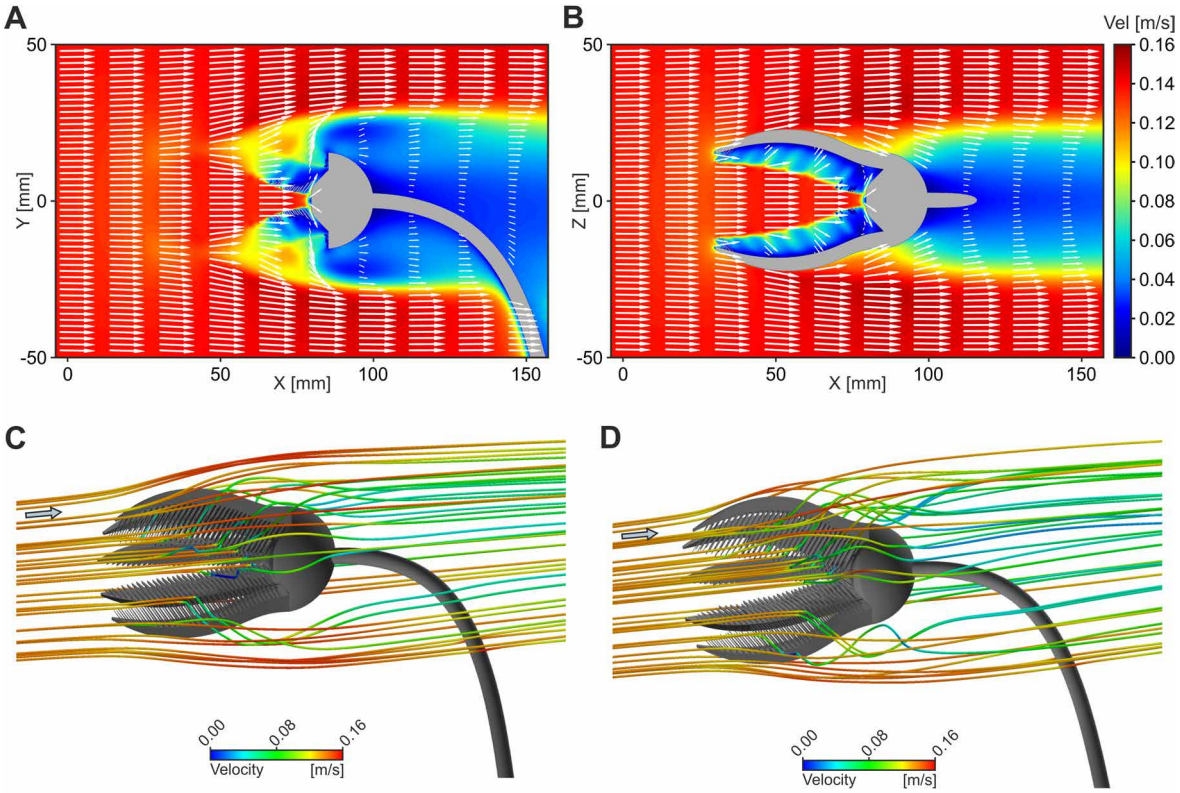

Figure 43: Results of flow analyses of the different models of *E. liliiformis* for V_{init} = 0.14 m/s and oral inflow. A: combined contour-vector plot on YZ plane; B: combined contour-vector plot on ZX plane; C: particle trajectories for model 10AP; D: particle trajectories for model AO. C+D: crinoid model cut to illustrate particle paths inside the crown.

V_{init} = 0.14 m/s. Reversing the inflow direction to simulate water coming from the oral side, results in similar flow patterns for all analysed models and inflow velocities. The flow enters the inside of the crown with almost unaltered velocity and direction (Fig. 43). Only by approaching the pinnules, the water is slowed down and deviated around the filtering structures. The crinoid evokes a broad wake in which the water has considerably lower flow velocities and approaches the freestream velocity slowly with increasing distance from the model. 200 mm behind the end of the calyx, the wake has reached 80 % of V_{init} in model 10AP and PiSp, while model AO causes a slightly stronger slow-down reaching 73 % of V_{init}, and model 7A results in the opposite effect with 82 % at the same distance.

The particle trajectories show that the particles reach the oral surface almost without any decrease in velocity, then are slowed down rather abruptly and deviated through the gaps between the pinnules and arms (Fig. 43C). Some particles pass the filtering structures two times on their way through the crown. An opening of the arms increases the catchment area that is facing the flow and thus the number of particles that are reaching the oral surface (Fig. 43D). The particle trajectories of model AO also illustrate the higher disturb-

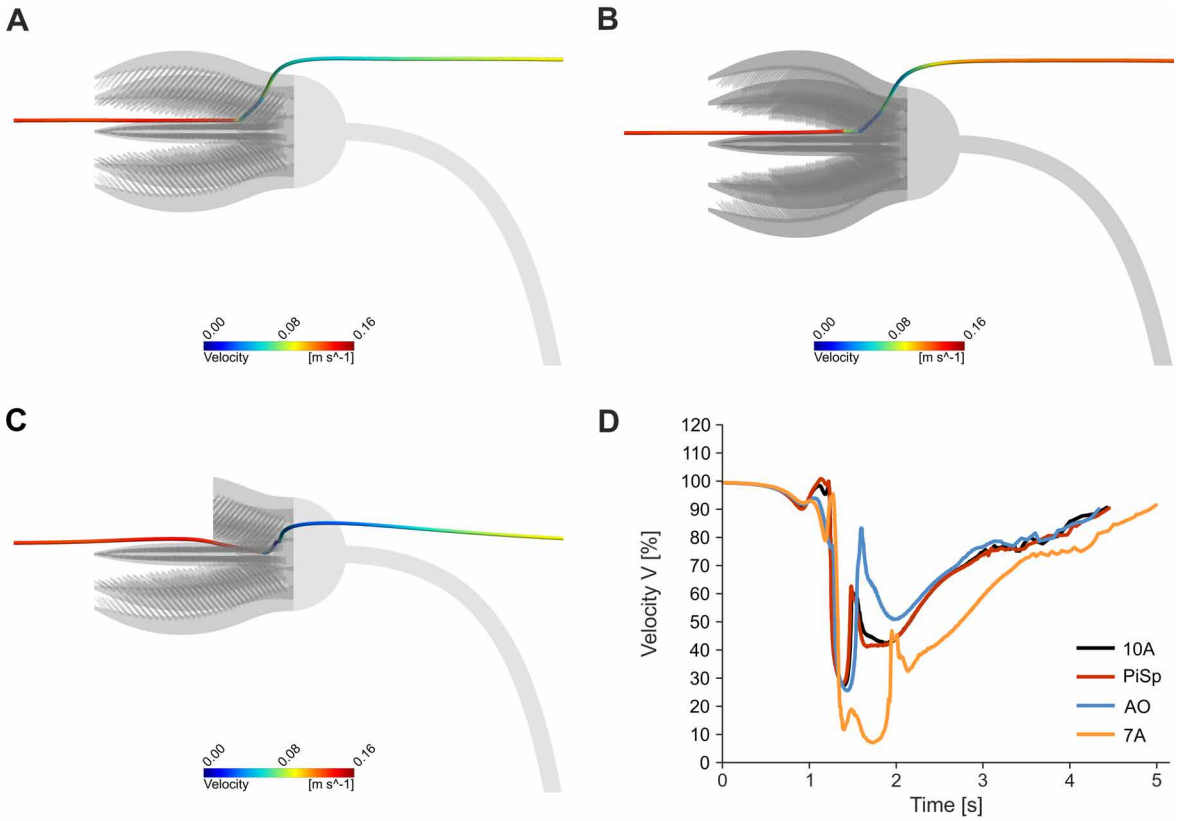

Figure 44: Path of one particle followed for the different models of *E. liliiformis* for V_{init} = 0.50 m/s and oral inflow. A: particle trajectory of model 10AP; B: particle trajectory of model AO; C: particle trajectory of model 7A; D: particle velocity V plotted against time.

ance caused by the crinoid model in the wake compared to model 10AP. A spreading of the pinnules also increases the catchment area, but to a much smaller extent than an opening of the arms. Model 7A has the opposite effect and many of the particles entering the crown are moving through the gap caused by the missing arm parts without approaching the pinnules.

Figure 44 illustrates the velocity of one particle that encounters a pinnule in the different variations of *E. liliiformis*. In all models the particle shows the same behaviour. It reaches the pinnule at the same time (1.2 s), its velocity decreases, then increases again while passing between the arms, followed by a second sequence of decreasing and increasing velocity in the wake of the crown. Model 7A causes a stronger and longer lasting decrease so that the particle shows a delayed increase in velocity and thus needs more time to pass through the computational domain than in the other models. In addition, the particle is deviated in -Y and thus the opposite direction compared to the other models.

With an oral inflow, the filtering surface is exposed to the water current directly and thus has to withstand the pressure exerted by the flowing water. The contour plots of Figure 45 illustrate the static pressure distribution on the oral surface of the crinoid crown for the four different models. In general, the distribution of the static pressure is similar in all models with peak values (orange colours) occurring on the tips of the arms and pinnules, and the centre

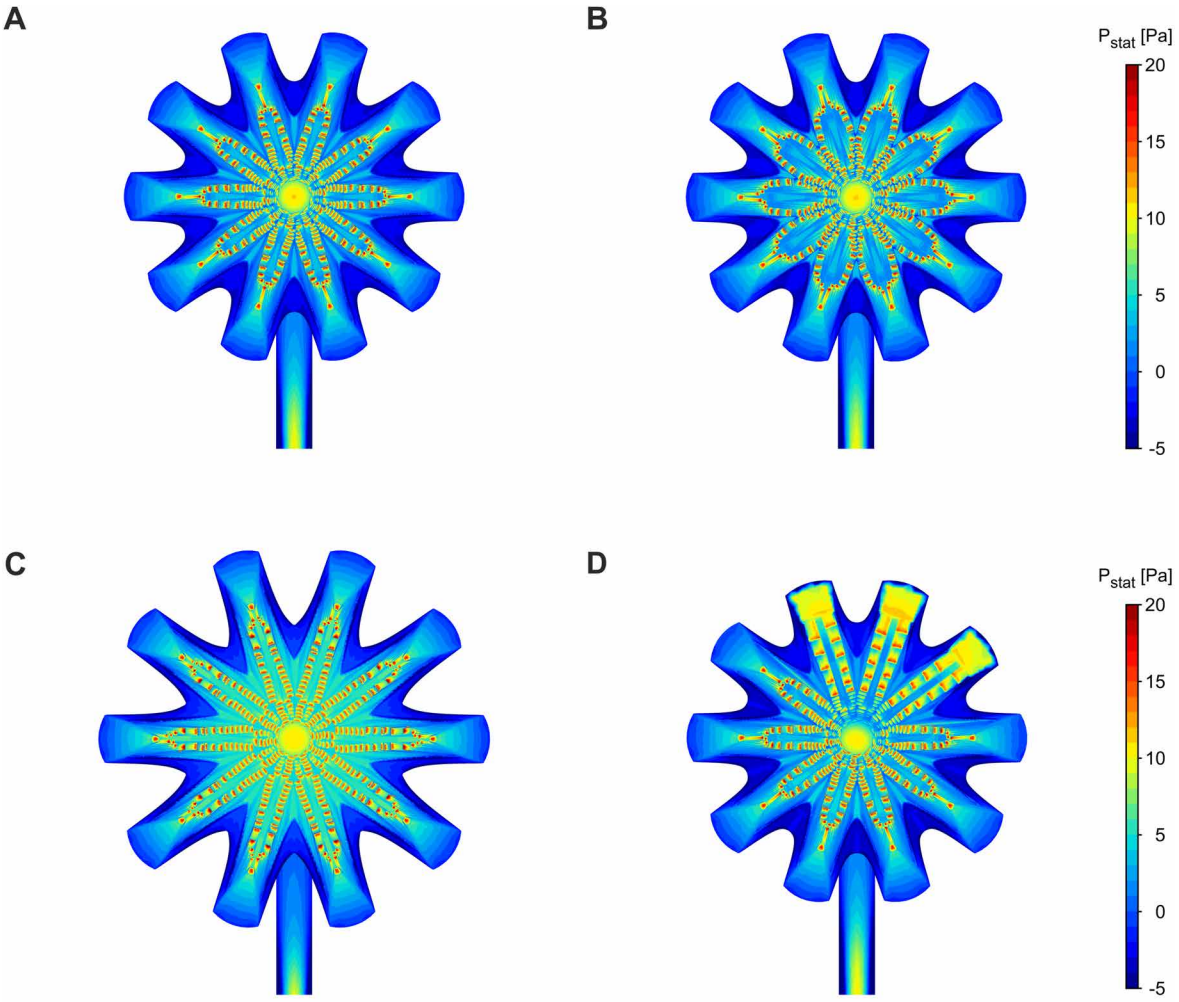

Figure 45: Static pressure distribution illustrated as contour plots for the different models of *E. liliiformis* at V_{init} = 0.14 m/s and oral inflow. A: model 10AP; B: model PiSp; C: model AO; D: model 7A.

of the tegmen. The highest pressure occurs on the tips of the pinnules reaching values of p_{stat} = 25.64 Pa (model 10AP). In the centre of the tegmen, the static pressure takes values of p_{stat} = 11.14 Pa (model 10AP).

The dynamic pressure distribution (Fig. 46) illustrates the baffling effect of the crown on the inflowing water. In front of the crown, the contour lines have a convex shape extending about 120 mm into upstream direction, with values of p_{dyn} = 10 Pa (Fig. 46A). The contour plot directly at the beginning of the arms (Fig. 46B) shows the concentric pressure distribution, with increasing values in the centre of the crown with p_{dyn} = 8.41 Pa. 10 mm in front of the tegmen (Fig. 46C), the dynamic pressure has increased to values of p_{dyn} = 9.66 Pa. The comparison of the four models (Fig. 46D, E) shows that only the opening of the arms has a considerable effect on the dynamic pressure distribution, resulting in a wider zone in front of the crown, and lower values close to the tegmen with p_{dyn} = 6.04 Pa.

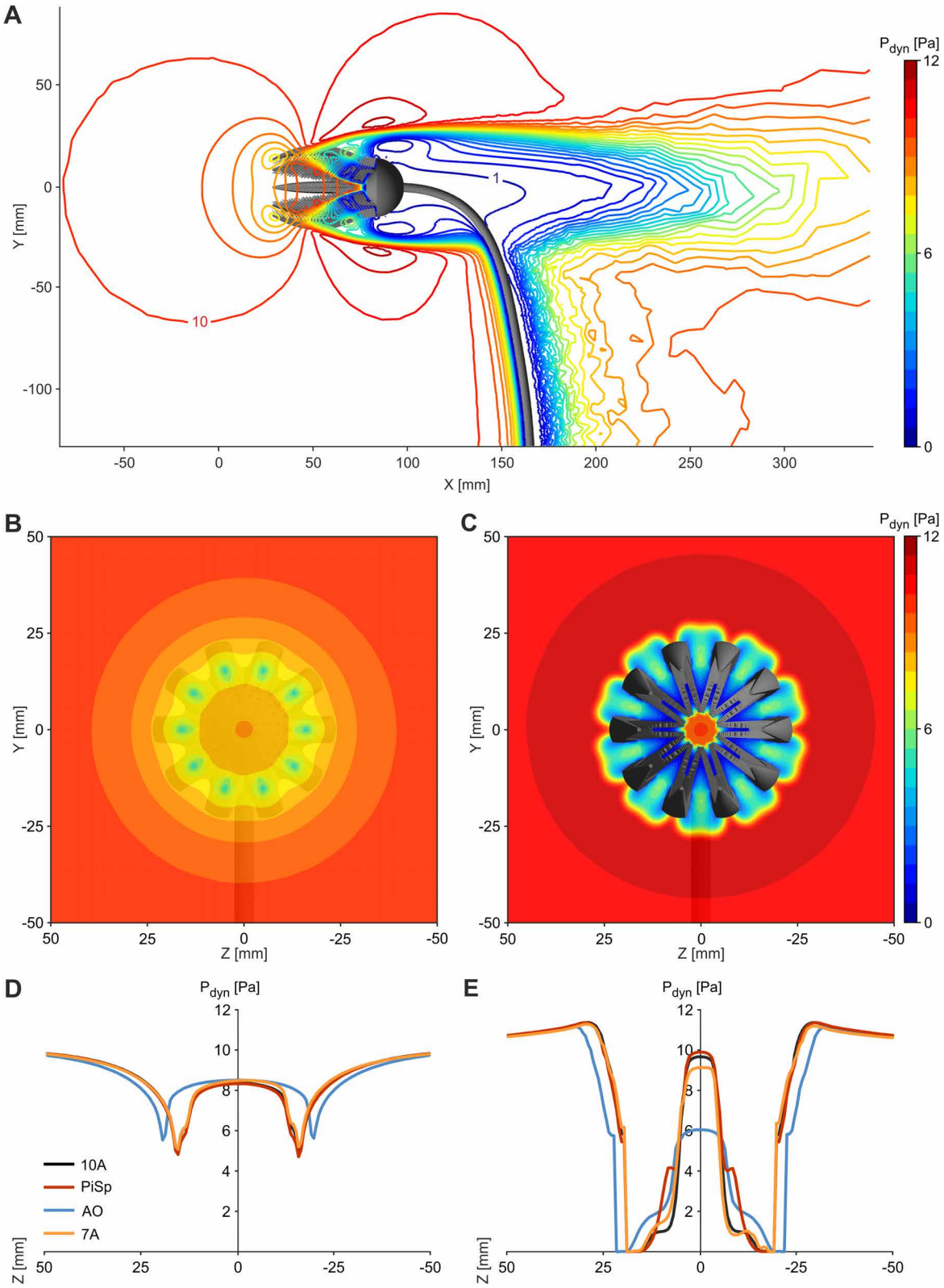

Figure 46: Dynamic pressure distribution for *E. liliiformis* at V_{init} = 0.14 m/s and oral inflow. A: contourline plot on plane XY for model 10AP; B: contour plot on Plane YZ1 for model 10AP; C: on Plane YZ2 for model 10AP; D: line graph plot at Line Z1 for all models; E: line graph plot at Line Z2 for all models.

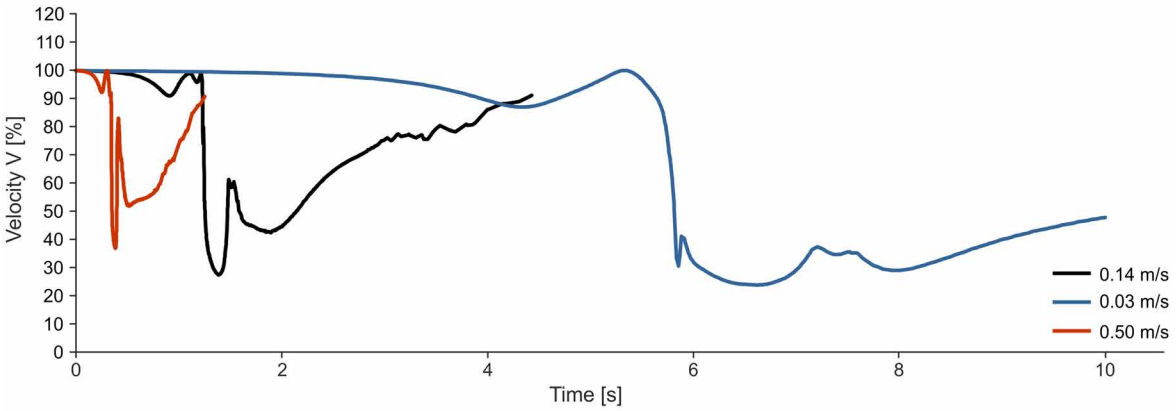

Figure 47: Velocity values of the same particle in all four analysed models, followed on its path through the computational domain, plotted against time. A: total velocity V in % of V_{init}; B: component u; C: component v; D: component w.

V_{init} = 0.03 m/s. The decrease in inflow velocity does not result in a considerable change of the flow field developing around the crown of *E. liliiformis*. Figure 47 illustrates the velocity profile of the same particle at the different inflow velocities for model 10AP. The particle at V_{init} = 0.03 m/s needs more time to pass the fluid domain, and generally shows less variation in velocity values along its path compared to the other inflow velocities. The general pressure distribution equals the one at the higher inflow velocities, with peaks of the static pressure on the tips of the pinnules with values of p_{stat} = 2.4 Pa for model 10AP. The static pressure occuring on the centre of the tegmen takes values of p_{stat} = 0.3 Pa. The distribution of the dynamic pressure in front of the crinoid is similar to that observed at V_{init} = 0.14 m/s, and reaches values of p_{dyn} = 0.46 Pa.

V_{init} = 0.50 m/s. Similar to the two lower inflow velocities, the flow field at V_{init} = 0.50 m/s shows a relatively straight and uniform flow of the water through the crown. The particle tracking simulations for model 10AP reveal that the curve progression of the particle velocity equals that of V_{init} = 0.14 m/s (Fig. 47), but the particle needs considerably less time to pass through the computational domain (1.3 s). Due to the increased velocity, the pressure acting on the crinoid is relatively higher, while the general pressure distribution does not show large differences. Peak values of the static pressure on the pinnules of model 10AP reach p_{stat} = 253 Pa, and on centre of the tegmen p_{stat} = 134.4 Pa. The dynamic pressure in front of the crown shows the same distribution as at V_{init} = 0.14 m/s, and the convex baffling effect takes values of p_{dyn} = 125 Pa.

5 Discussion

5.1 Parabolic filtration fan

In the presented study, the flow analyses of the parabolic filtration fan were performed experimentally using PIV, and computationally with CFD, to evaluate the potential of these methods for the investigation of filter feeding in crinoids. Both methods result in generally similar flow fields, with a straight flow of water through the crown, so that the used turbulence model and setup criteria proved to be adequate. The observed differences for the five-armed *Hyocrinus* sp. can be explained by the discrepancies of the handmade model from the computer-generated geometry. In future studies, the results comparison of PIV and CFD could be enhanced by using 3D printed computer models instead of handmade ones. The CFD simulations enabled to setup more natural conditions, include particle tracking and investigate finer filter structures. Even if no validation data can be provided (due to the lack of comparative experiments in the deep sea or with living crinoids in flow tanks), it is concluded from the generally good agreement of both applied methods that the observed flow patterns of the extended computer models generally resemble those that would be obtained with living crinoids under natural conditions.

In the analysed models of *Hyocrinus* sp. and *N. decorus*, the crown does not induce recirculating turbulences in the wake, which is assumed based on theoretical considerations for other crinoids (Roux, 1978, 1979, 1987). In these studies, it appeared that the crown shape leads to the formation of small scale eddies (= independent "packages" of swirling fluid) in its wake, increasing the drag acting on the crinoid. In present-day sea lilies it is assumed that the animal holds the crown in such a position as to benefit from the maximum possible lift elevating the crown above the sea floor (Roux, 1987; Baumiller, 1992). The drag forces, however, have to be minimal to avoid high strain on the stalk and its ligaments and to prevent detachment from the sea floor. Drag values for *Cenocrinus asterius* were obtained by strain gages attached to a living specimen in a flow tank and found to be in the range of 0.06 to 0.07 N for flow velocities of 0.04 to 0.06 m/s (Baumiller, 1993). A computer analysis of drag as well as lift forces would need to incorporate the tube feet so that here no comparative data can be provided.

Based on flume studies using models of the fossil crinoid *Pterotocrinus* forming a parabolic filtration fan (Welch, 1978), recirculations in the wake of the crinoids are interpreted to redirect water and nutritive particles back onto the oral surface, where they can be caught by the tube feet. This suggestion is supported by experimental studies on gorgonian corals (Leversee, 1976) as well as by the monitoring of feather stars showing similar feeding positions (Nichols, 1960; Meyer, 1973, 1979; Holland et al., 1986). It was assumed that this

leeward feeding has certain advantages for catching food particles out of the water and can be observed in different suspension feeding organisms (Warner, 1977). *Hyocrinus* sp. with its five arms and also the expanded model of *N. decorus* with 20 arms, however, represent open filter architectures thus precluding the development of large scale turbulences and a recirculation zone in their wake. In *Hyocrinus* sp., a small recirculation area behind the crown exists, in *N. decorus* this area is enlarged and additional zones form behind the arms, but the particle tracking simulations reveal that these areas are too small to catch any particles and redirect them back to the oral surface.

In the presented study, the baffling effect of the crown that was described for feather stars (Meyer, 1982), and flow tank models of *Pterotocrinus* (Welch, 1978), is larger in the 20-armed than in the five-armed crinoid which is consistent with other studies on filters (Loudon, 1990, Baumiller, 1993b). As was shown for simplified filter architectures based on recent crinoids (Baumiller, 1993b) and fossil crinoids (Kammer and Ausich, 1987; Holterhoff, 1997; Brower, 2007), coarse filters perform over a wide range of flow velocities including low speeds while fine filters need a minimum velocity and are adapted to higher speeds. This relationship was also found in the fossil record and used to explain the distribution of crinoids with varying crown morphologies in different sedimentary environments (Meyer et al., 2002). Distinct distributions of crinoid assemblages have also been described for recent sea lilies where occurrences were correlated to different water depths and substrate types with some species being restricted to specific flow regimes (Messing, 1985).

The 20-armed *N. decorus* exposes a much larger filter area towards the flow and thus has a higher particle capture rate compared to the five-armed *Hyocrinus* sp. during similar flow conditions. Generating quantitative data of particle capture rates is, however, not possible in this study since monitoring of particle capture requires tube feet. Detailed theoretical considerations of biological filter feeding mechanisms were described by Rubenstein and Koehl (1977), where 5 basic mechanisms of particle capture were identified. According to the comprehensive study of Shimeta and Jumars (1991), only two of these basic mechanisms are of high importance for passive suspension feeders: direct interception and inertial impaction. To get insights into the details of paricle capture, the simulations would need to include a different solver (Fluent instead of CFX) so that an erosion model could be used to identify particles that touch the filtering surface instead of only passing them in close vicinity.

The analysis of the tube feet submodel revealed the presence of recirculation currents right behind the finer filtering structures, but particle transport onto the oral surface could not be confirmed in the present study. As could be shown, many of the injected plankton particles instead pass in between the tube feet and are thus likely to be caught by direct capture, without the necessity of recirculation involved in the feeding process.

5.2 *Encrinus liliiformis*

The comparison of the PIV and CFD results for the fossil crinoid *E. liliiformis* with an aboral inflow direction show a good agreement. Because this is the first time that such an analysis has been conducted on fossil crinoids, a description of the occurring recirculation current has not been reported before and no comparative data exist. Due to the shape of the crown, however, the development of the observed eddies in its wake is not surprising, and is well known from standardized bodies (e.g. Hucho, 2011). The further CFD analysis of *E. liliiformis*, including variations of the morphology as well as of inflow velocities and directions, reveal that the tear shape of the crown had a broad functionality and was suitable for feeding under frequently changing flow conditions. Because *E. liliiformis* lived in a dynamic environment (Aigner, 1985; Hagdorn, 1991), it is to be expected that changes in flow conditions occurred within relative short time periods. A rapid reorientation of the complete crown was probably not possible so that the ability to feed by maintaining the filter position while the current changed, was beneficial in shallow water environments.

Studies on feeding in crinoids that differ in their morphology from the typical parabolic filtration fan are scarce, and almost all hydrodynamic studies thus far have focused on Palaeozoic crinoids, and the analysed species differ largely from *E. liliiformis* as far as morphology and thus feeding position is concerned (e.g. Haugh, 1978; Ausich, 1986; Brower, 2007; Bohatý, 2011). The Calceocrinoidea were reconstructed as leeward suspension feeders with the stem lying on the sea floor instead of taking an erect posture (Ausich, 1986), such that the crown was positioned in the benthic boundary layer just above the sea floor. The Palaeozoic crinoid *Ammonicrinus* (Bohatý, 2011) was described as a soft-bottom dweller that obtained nutrients in lowintensity currents by active suspension feeding. A direct comparison of these extinct crinoids with the presented anaylsis is thus not feasible. Examples of recent crinoids that show an exception in the typical body plan of present-day crinoids are the Holopodidae, which cement directly to the substratum, lacking a stalk, and have ten stout arms which are not recurved into the water current, but have a funnel-like appearance (Donovan and Pawson, 2008). The species *Holopus rangii* was hypothesized to be an active raptorial feeder catching benthonic plankton and preferring habitats with only moderate unidirectional flow (Grimmer and Holland, 1990). The cyrtocrinid genus *Cyathidium*, which is described as part of a "living-fossil community" (Wisshak et al., 2009), was suggested to be both a suspension as well as a raptorial feeder (Heinzeller and Fechter, 1995). Unfortunately, due to the lack of observations there has been no direct evidence for such feeding behavior until now, and no comparative data exist for the presented study.

An aboral inflow resulted in the formation of a recirculation current that was strong enough to transport plankton particles back onto the oral surface. Inside the crown, the flow was

decelerated, thus increasing the residence time of the particles. The decelerated particles could then be caught by the extended tube feet covering the pinnules. Because the arms were not tightly closed and due to naturally occurring slight irregularities in flowing water, there was a constant exchange of water between the outside and the inside of the crown, preventing the formation of stationary circulation. The catchment area of particles reaching this recirculating current, however, is relatively small and particles have to pass the crinoid crown closely to be redirected onto the oral surface. Particles passing directly between the arms thus represent an additional food source and feeding through recirculation probably was not the only food catching mechanism involved. Thus, even if spreading of the pinnules did not have a strong effect on the overal flow pattern, it did increase the area for direct catchment in between the arms, while the recirculation current was slowed down slightly. Future studies could include the application of a different solver (Fluent instead of CFX) to implement an erosion model and calculate the number of particles that actually touch the filtering surface.

Higher inflow velocities resulted in increased velocity gradients inside the crown, allowing particles to pass through the boundary layer around the filtering structures, thus increasing the particle capture probability. In addition, the recirculation zone was enlarged towards the inside of the crown. Particles could thus be transported deeper into the crown and thus closer to the mouth into an area where the pinnule spacing was denser compared to the distal parts of the arms. Besides the dependance on the freestream flow, the velocity inside the crown could also be influenced actively by the crinoid by adjusting the opening angle of the arms. A wider opening resulted in an increased number of backwards transported particles, which reached higher recirculation velocities and performed a larger number of turns inside the crown thus increasing the particle capture probability. This mechanism of recirculation requires, however, an adequate velocity of the surrounding water to transport the particles back to the crinoid and accelerate them to such an extant as to enable the penetration of the boundary layer.

The effect of predation or loss of parts of the arms due to autotomy, does not prevent the formation of a water recirculation zone, but it does change the behaviour of the particles considerably. While particles are still transported back to the crinoid, most of them leave the inside of the crown through the gap caused by the missing part without reaching the oral surface. Thus it can be concluded that already a loss of parts of three arms decreased the amount of nutritive particles caught by recirculation substantially.

The analysed posture of *E. liliiformis* with flow coming from the aboral side resembles the survival posture of present-day forms in high or turbulent currents (Haugh, 1978; Roux, 1987). This tear shape reduces drag forces on the crown, but results in the cessation of

feeding due to the closure of the arms. The tear shape of *E. liliiformis* in combination with an aboral inflow represents a streamlined shape possibly offering the ability to tolerate higher flow velocities without being torn from the substrate. Assuming that fossil crinoids also possessed mutable collagenous tissue, they also were able to hold their feeding position by stiffening this specialized tissue, without expending any more energy (Baumiller, 2008) so that a constant feeding position was energetically benefical. The pressure distributions on the surface of *E. liliiformis* for an oral as well as a lateral inflow show that the highest pressure values occurred on the stalk and the calyx. The morphology of these two features thus is a crucial parameter influencing the pressure the crinoid had to withstand.

The topology of the arms is an additional feature to be considered in the investigation of the fluid dynamic performance of *E. liliiformis*. Based on crown morphology, two different ecophenotypes have been identified (Dynowski and Nebelsick, 2011), one living in shallow water with frequently changing flow conditions, the other inhabiting deeper water settings with rather constant flow conditions. One parameter differentiating these ecophenotypes is an arm ornamentation which is more pronounced in the population originating from a deeper water setting and may have been beneficial in avoiding flow separation and thus high drag forces in unidirectional flow. Assumptions concerning developing lift forces are difficult to make without experimental data, but it is assumed that in comparison with the parabolic filtration fan, the more compact form of *E. liliiformis* increased lift, whereas the higher weight of the crown counteracted the upward facing force. As known from different standardized objects such as air foils, lift is strongly dependant on the angle of attack (Vogel, 1996). By slightly altering the bending of the proximal part of the column (near the crown) *E. liliiformis* was probably able to adjust the angle of attack in order to benefit from the maximum lift.

A lateral inflow, in the presented study simulated by a rotation of the crown by 45°, leads to direct through flow of the particles through the pinnules, which could then be caught by the tube feet. In this orientation, no recirculation occurred, but the number of particles passing directly through the filtering surface was considerably higher compared to an aboral inflow direction, where the main amount of particles approaching the filtering surface was transported by backward oriented water movement. With a lateral inflow, some of the particles approached the filter structures two times thus increasing the catchment probability. Inflow coming from the oral side, however, increased the drag experienced by the crinoid significantly such that the animal probably had to compromise by adjusting the opening angle of the arms and pinnules, dependent on the flow velocity. With increasing flow velocity, the pressure acting on the filtering surface also increases, so that this position was likely to be beneficial in lower flow velocities than a position where the inflow came from an aboral direction.

In general, there is a lack of knowledge on the composition of plankton particles, their concentrations and thus volume flux in ancient environments and the metabolic needs of *E. liliiformis*. Thus statements on particle capture rates and sufficiency of the recirculation mechanism to fullfill the metabolic needs of *E. liliiformis* are difficult to make. Assumptions about the fluid flux through filters of living crinoids are based on simplified orthogonal arrays of fibres including the finer morphological structures of tube feet, and metabolic rates assumed for living crinoids are thus averaged at 1.5 x 10^{-5} ml O_2 per gram wet weight per second (Baumiller, 1993b), a value which was probably higher for *E. liliiformis* due to the larger body mass of the crown. There is an upper limit of particle number for unproblematic feeding because the gathered particles have to be removed from the filtering surface before new ones can be caught. Otherwise, the filter would get clogged und stop functioning.

It has been suggested that *E. liliiformis* was a specialized feeder, being able not only to obtain nutrients by passive, but also by active suspension feeding (Jefferies, 1989), a feeding strategy that is not known from living crinoids. This conclusion was based on the occurrence of distinctive grooves on the pinnules forming channels with diameters of up to 50 micrometers, which were reconstructed as being ciliated and thus enabled the crinoid to produce an active feeding current. Following this suggestion, active filter feeding could have been used in the proximal parts of the crinoid's arms, and concurrent passive suspension feeding in the distal parts of the arms (Jefferies, 1989). Because, however, in this reconstruction, no gaps are left between the pinnules (otherwise the interpinnular channels would not exist) it is hard to imagine how water could have penetrated through the pinnules regardless of how strong the beating of the cilia was. This feeding position with a relatively tightly closed crown, would have represented a very compact shape, evoking a water flow past the crinoid, without any or at most a very poor water exchange with the internal space of the crown.

A co-occurrence of active and passive filter feeding seems unlikely, and instead, a switch from active to passive filter feeding, which was observed in a porcelain crab at particular flow velocities (Trager and Genin, 1993), might have been possible for *E. liliiformis*. Active filter feeding is more advantageous in low flow velocities, whereas passive filter feeding only works effectively in higher flow velocities (Trager and Genin, 1993). *E. liliiformis* may have had the ability to switch between these feeding modes as a reaction to changing flow conditions to very low velocities. From the results of the presented study, it is concluded that passive suspension feeding was, however, the main strategy used by *E. liliiformis*, also because it is energetically more favourable (Gili and Coma, 1998). An aboral inflow of water with varying opening angles of the arms and pinnules enabled this crinoid to feed on a recirculating current, while lateral or oral inflow led to direct capture of plankton particles.

6 Conclusions and outlook

PIV and CFD

The presented study demonstrates that both applied methods, the flow tank experiments using PIV, as well as the computer simulations with CFD, provide suitable tools to investigate the flow field developing around biological inspired filter architectures. The PIV experiments give insights into global flow patterns, while the computer simulations additionally enable the analysis of small scale structures and of additional parameters like pressure distributions.

For the comparison of PIV with CFD results, however, it would be beneficial to use 3D-prints of previously created computer models for the flow tank experiments to avoid the observed deviations. With the present development of this technique, it should by now be possible and affordable to produce water resistant models with great detail as to print the delicate pinnules. For the computer simulations, high quality meshes are important prerequisites for reliable results of the numerical calculations. With the availability of computer clusters and high performance computing, the computational resources become sufficient to resolve the complicated geometries involved. Thus, in future work meshes can be generated that suffice the prerequisites for calculating the flow field in the boundary layer, and thus the derivation of lift and drag coefficients.

Living crinoids

In the analysed global models, showing the typical feeding position of living stalked crinoids, food capture generally functions by catching plankton out of the trough flowing water, without a main contribution of recirculation currents. Particles that pass the pinnules, are deviated through the small gaps between the tube feet and are thus likely to be captured. Local recirculation flows develop behind the tube feet, but in the analysed setup, almost no particles are transported backwards onto the oral surface.

For further interpretations, however, the role of the tube feet has to be investigated in detail, with a systematic study including variations of morphological features of the crinoid as well as of the injected plankton particles. Important morphological parameters include: the width, length and distance of the tube feet, as well as the distance of the pinnules and thus of two adjacent rows of tube feet, which are in addition dependent on the rotation angle of the tube feet. The size of the gap between the rows of tube feet seems to be a crucial parameter controlling the occurrence or absence of recirculation, because it influences the Reynolds number and thus the local flow regime. Including the tube feet into the global crinoid model requires high computational needs, which now become available through high performance computing. It is to be expected that a global model including the finer filtering structures will have an apparently stronger baffling effect on the water flow.

Fossil crinoids

For fossil crinoids with an alternate morphology, where the arms form a tear shape, and habitats quite different in flow regime compared to today's deep sea, recirculation of plankton into the crown is likely to have represented the dominant feeding mechanism, when the inflow came from an aboral direction. The shape and surface of the calyx and arms, as well as the opening angle of the crown here are important parameters controlling the path and thus the number of particles that are caught in the recirculation current. Below a specific water velocity, the recirculation did not suffice for satisfying the nutritional needs of the crinoid, so that in low velocities, an inflow from oral would have been beneficial. Because flow reversions naturally occur in shallow water regimes, which are supposed for many fossil crinoid deposits, these crinoids did not necessarily had to actively reorient themselves, but could feed under various inflow directions, including lateral inflow during transition times of current reversal.

Future investigations should focus on the surface structure of the calyx and arms, as well as investigate whole populations of crinoids, where the local flow field of one specimen is influenced by the presence of the other individuals. Furthermore, the sea floor should be included to analyse a most complete representation of the environment as possible.

References

AIGNER, T. (1985). Storm depositional systems. Dynamic stratigraphy in modern and ancient shallow-marine sequences. Lecture Notes in Earth Sciences 3.

AIGNER, T. AND BACHMANN, G. H. (1992). Sequence-stratigraphic framework of the German Triassic. Sedimentary Geology 80, 115-135.

ANDERSON, J. D. JR. (2011). Fundamentals of Aerodynamics (SI Edition). New York: McGraw-Hill.

AUSICH, W. (1986). Palaeoecology and history of the Calceocrinidae (Palaeozoic Crinoidea). Palaeontology 29, 85-99.

AUSICH, W. (1997). Regional encrinites: a vanished lithofacies. In: Paleontological Events: Stratigraphic, Ecological, and Evolutionary Implications (eds. C. E. Brett and G. C. Baird), pp. 509-519. New York: Columbia University Press.

BAUMILLER, T. K. (1992). Importance of hydrodynamic lift to crinoid autecology, or, could crinoids function as kites? Journal of Paleontology 66, 658-665.

BAUMILLER, T. K. (1993). Crinoid stalks as cantilever beams and the nature of stalk ligament. Neues Jahrbuch für Geologie und Paläontologie Abhandlungen 190, 279-297.

BAUMILLER, T. K. (1993b). Survivorship analysis of Paleozoic Crinoidea: effect of filter morphology on evolutionary rates. Paleobiology 19, 304-321.

BAUMILLER, T. K. (2008). Crinoid Ecological Morphology. Annual Reviews of Earth and Planetary Sciences 36, 221-249.

BAUMILLER, T. K. AND MESSING, C. G. (2007). Stalked Crinoid Locomotion, and its Ecological and Evolutionary Implications. Palaeontologia Electronica 1, 10.11.12A.

BAUMILLER, T. K., LABARBERA, M. AND WOODLEY, J. D. (1991). Ecology and Functional Morphology of the Isocrinid *Cenocrinus asterius* (Linnaeus) (Echinodermata: Crinoidea): In situ and Laboratory Experiments and Observations. Bulletin of Marine Science 48, 731-748.

BAUMILLER, T. K., SALAMON, M. A., GORZELAK, P., MOOI, R., MESSING, C. G. AND GAHN, F. J. (2010). Post-Paleozoic crinoid radiation in response to benthic predation preceded the Mesozoic marine revolution. Proceedings of the National Academy of Sciences 107, 5893-5896.

BOHATÝ, J. (2011). Revision of the flexible crinoid genus *Ammonicrinus* and a new hypothesis on its life mode. Acta Palaeontologica Polonica 56, 615-639.

BREIMER, A. (1978). Recent crinoids. In: Treatise on Invertebrate Paleontology. Part T, Echinodermata 2, Crinoidea, vol. 1 (eds. R. C. Moore and C. Teichert), pp. 9-57. Boulder, Colorado: Geological Society of America and University of Kansas.

BROWER, J. C. (2007). The application of filtration theory to food gathering in Ordovician crinoids. Journal of Paleontology 81, 1284-1300.

CONAN, G., ROUX, M. AND SIBUET, M. (1981). A photographic survey of a population of the stalked crinoid *Diplocrinus (Annacrinus) wyvillethomsoni* (Echinodermata) from the bathyal slope of the Bay of Biscay. Deep Sea Research 28A, 441-453.

D'ANS, J. AND LAX, E. (1992). Taschenbuch für Chemiker und Physiker. Band I: Physikalisch-chemische Daten (ed. M. D. Lechner). Berlin: Springer.

DONOVAN, S. K. AND PAWSON, D. L. (2008). A new species of the sessile crinoid *Holopus* d'Orbigny from the tropical western Atlantic, with comments on holopodid ecology (Echinodermata: Crinoidae: Holopoidiae). Zootaxa 1717, 31-38.

DYNOWSKI, J. F. AND NEBELSICK, J. H. (2011). Ecophenotypic variations of *Encrinus liliiformis* (Echinodermata: Crinoidea) from the middle Triassic Muschelkalk of Southwest Germany. Swiss Journal of Palaeontology 130, 53-67.

FEIST-BURKHARDT, S., GÖTZ, A. E., SZULC, J., BORKHATARIA, R., GELUK, M., HAAS, J., HORNUNG, J., JORDAN, P., KEMPF, O., MICHALÍK, J., NAWROCKI, J., REINHARDT, L., RICKEN, W., RÖHLING, H.-G., RÜFFER, T., TÖRÖK, Á. AND ZÜHLKE, R. (2008). Triassic. In: The Geology of Central Europe, Volume 2: Mesozoic and Cenozoic (ed. T. McCann), 749-821. London: The Geological Society.

GEYER, M., NITSCH, E. AND SIMON, T. (2011). Geologie von Baden-Württemberg. Stuttgart: Schweizerbart.

GILI, J.-M. AND COMA, R. (1998). Benthic suspension feeders: their paramount role in littoral marine food webs. TREE 13, 316-321.

GRIMMER, J. C. AND HOLLAND, N. D. (1990). The Structure of a Sessile, Stalkless Crinoid (*Holopus rangii*). Acta Zoologica 71, 61-67.

HAGDORN, H. (1991). The Muschelkalk in Germany - An Introduction. In: Muschelkalk - A Field Guide (ed. H. Hagdorn), pp. 7-21. Korb: Goldschneck-Verlag.

HAGDORN, H. (1999). Triassic Muschelkalk of Central Europe. In: Fossil Crinoids (eds. H. Hess, W. I. Ausich, C. E. Brett and M. J. Simms), 164-176. Cambridge: Cambridge University Press.

HAUGH, B. N. (1978). Biodynamic and phyletic paradigms for sensory organs in camerate crinoids. Lethaia 11, 145-173.

HEINZELLER, T. AND FECHTER, H. (1995). Microscopical Anatomy of the Cyrtocrinid *Cyathidium meteorensis* (sive *foresti*) (Echinodermata, Crinoidea). Acta Zoologica 76, 25-34.

HEINZELLER, T. AND WELSCH, U. (1994). Crinoidea. In: Microscopic Anatomy of Invertebrates (eds. F. W. Harrison and F.-S. Chia), Vol 14, 9-148. New York: Wiley-Liss Inc.

HESS, H. (2011). Encrinida. In: Treatise on Invertebrate Paleontology. Part T, Echinodermata 2, Revised, Crinoidea, vol. 3 (ed. P. A. Seldon), 28-41. Lawrence, Kansas: The University of Kansas Paleontological Institute.

HOLLAND, N. D., STRICKLER, J. R. AND LEONARD, A. B. (1986). Particle interception, transport and rejection by the feather star *Oligometra serripinna* (Echinodermata: Crinoidea), studied by frame analysis videotapes. Marine Biology 93, 111-126.

HOLTERHOFF, P. F. (1997). Filtration models, guilds, and biofacies: Crinoid paleoecology of the Stanton Formation (Upper Pennsylvanian), midcontinent, North America. Palaeogeography Palaeoclimatology Palaeoecology 130, 177-208.

HUCHO, W.-H. (2011). Aerodynamik der stumpfen Körper. Wiesbaden: Vieweg+Teubner Verlag / Springer-Verlag.

ITTC FRESH WATER AND SEAWATER PROPERTIES (2011). Table provided by the International Towing Tank Conference at http://ittc.sname.org/CD

JEFFERIES, R. P. S. (1989). The arm structure and mode of feeding of the Triassic crinoid *Encrinus liliiformis*. Palaeontology 32, 483-497.

JØRGENSEN, C. B. (1983). Fluid mechanical aspects of suspension feeding. Marine Ecology Progress Series 11, 89-103.

KAMMER, T. W. AND AUSICH, W. I. (1987). Aerosol suspension feeding and current velocities: distributional controls for late Osagean crinoids. Paleobiology 13, 379-395.

KITAZAWA, K., OJI, T. AND SUNAMURA, M. (2007). Food composition of crinoids (Crinoidea: Echinodermata) in relation to stalk length and fan density: their paleoecological implications. Marine Biology 152, 959-968.

KITAZAWA, K. AND OJI, T. (2010). Particle selection by the sea lily *Metacrinus rotundus* Carpenter 1884 (Echinodermata, Crinoidea). Journal of Experimental Marine Biology and Ecology 395, 80-84.

LABARBERA, M. (1984). Feeding Currents and Particle Capture Mechanisms in Suspension Feeding Animals. American Zoologist 24, 71-84.

LAWRENCE, J. (1987). Acquisition of Nutrients. In: A Functional Biology of Echinoderms (ed. P. Calow), pp. 17-31. London, Sidney: Croom Helm Ltd. Publishers.

LEVERSEE, G. J. (1976). Flow and feeding in fan-shaped colonies of the gorgonian coral, *Leptogorgia*. Biological Bulletin 151, 344-356.

LOUDON, C. (1990). Empirical test of filtering theory: Particle capture by rectangular-mesh nets. Limnology and Oceanography 35, 143-148.

LINCK, O. (1954). Die Muschelkalk-Seelilie *Encrinus liliiformis* - Ergebnisse einer Grabung. Naturwissenschaftliche Monatsschrift, Aus der Heimat 62, 225-235.

LINCK, O. (1965). Stratigraphische, stratinomische und ökologische Betrachtungen zu *Encrinus liliiformis* Lamarck. Jahreshefte des geologischen Landesamtes in Baden-Württemberg 7, 123-148.

MACURDA, D. B. AND MEYER, D. L. (1974). Feeding Posture of Modern Stalked Crinoids. Nature 247, 394-396.

MESSING, C. G. (1985). Submersible observations of deep-water crinoid assemblages in the tropical western Atlantic Ocean. In: Proceedings of the 5th International Echinoderm Conference in Galway (eds. B. F. Keegan and B. D. S. O'Connor), 185-193. Rotterdam: A. A. Balkema.

MEYER, D. L. (1973). Feeding behavior and ecology of shallow-water unstalked crinoids (Echinodermata) in the Caribbean Sea. Marine Biology 22 105-129.

MEYER, D. L. (1979). Length and spacing of the tube feet in crinoids (Echinodermata) and their role in suspension-feeding. Marine Biology 51, 361-369.

MEYER, D. L. (1982). Food and Feeding Mechanisms: Crinozoa. In: Echinoderm Nutrition (eds. M. Jangoux and J. M. Lawrence), pp. 25-42. Rotterdam: A. A. Balkema.

MEYER, D. L., MILLER, A. I., HOLLAND, S. M. AND DATTILO, B. F. (2002). Crinoid distribution and feeding morphology through a depositional sequence: Kope and Fairview Formations, Upper Ordovician, Cincinnati Arch Region. Journal of Paleontology 76, 725-732.

NEBELSICK, J. H. AND KROH, A. (2002). The Stormy Path from Life to Death Assemblages: The Formation and Preservation of Mass Accumulations of Fossil Sand Dollars. Palaios 17, 378-394.

NICHOLS, D. (1960). The Histology and Activities of the Tube-feet of *Antedon bifida*. Quarterly Journal of Microscopical Science 101, 105-117.

PAWSON, D. L. (2007). Phylum Echinodermata. Zootaxa 1668, 749-764.

RADWAŃSKI, A. (2002). Triassic brittlestar beds of Poland: a case of *Aspiduriella ludeni* (v. Hagenow, 1846) and *Arenorbis squamosus* (E. Picard, 1858). Acta Geologica Polonica 52, 395-410.

RIISGARD, H. U. AND LARSEN, P. S. (2010). Particle capture mechanisms in suspension-feeding invertebrates. Marine Ecology Progress Series 418, 255-293.

ROUX, M. (1978). Ontogenèse, variabilité et évolution morphofonctionelle du pédoncule et du calice chez les Millericrinida (Echinodermes, Crinoides). Géobios 11, 213-241.

ROUX, M. (1979). Un example de relation étroite entre la géodynamique des océans et l'evolution des faunes benthiques bathyales et abyssales: l'histoire des Crinoides pédonculés du Mésozoique à l'Actuel. Bulletin de la Societé géologique France 7, 613-618.

ROUX, M. (1987). Evolutionary ecology and biogeography of recent stalked crinoids as a model for the fossil record. Echinoderm Studies 2, 1-53.

RUBENSTEIN, D. I. AND KOEHL, M. A. R. (1977). The Mechanisms of filter feeding: some theoretical considerations. The American Naturalist 111, 981-994.

SCHLICHTING, H. AND GERSTEN, K. (2006). Grenzschicht-Theorie. Berlin Heidelberg: Springer-Verlag.

SHIMETA, J. AND JUMARS, P. A. (1991). Physical mechanisms and rates of particle capture by suspension-feeders. Oceanography and Marine Biology: An Annual Review 29, 191-257.

SPURK, J. H. AND AKSEL, N. (2007). Strömungslehre: Einführung in die Theorie der Strömungen. Berlin Heidelberg: Springer-Verlag.

TRAGER, G. AND GENIN, A. (1993). Flow Velocity Induces a Switch From Active to Passive Suspension Feeding in the Porcelain Crab *Petrolisthes leptocheles* (Heller). Biological Bulletin 185, 20-27.

VOGEL, S. (1996). Life in Moving Fluids: The Physical Biology of Flow. Princeton, New Jersey: Princeton University Press.

VOLLRATH, A. (1957). Zur Entwicklung des Trochitenkalkes zwischen Rheintal und Hohenloher Ebene. Jahreshefte des geologischen Landesamtes Baden-Württemberg 2, 119-134.

WAGNER, W. AND KRETZSCHMAR, H.-J. (2008). International Steam Tables. Berlin, Heidelberg: Springer-Verlag.

WARNER, G. F. (1977). On the shape of passive suspension feeders. In: Biology of Benthic Organisms (eds. B. F. Keegan, P. O. Ceideigh and P. J. S. Boaden), pp. 567-576. Oxford: Pergamon.

WELCH, J. R. (1978). Flume study of simulated feeding and hydrodynamics of a Paleozoic stalked crinoid. Paleobiology 4, 89-95.

WILLIAMSON, C. H. K. AND GOVARDHAN, R. (2004). Vortex-Induced-Vibrations. Annual Review of Fluid Mechanics 36, 413-455.

WISSHAK, M., NEUMANN, C., JAKOBSEN, J. AND FREIWALD, A. (2009). The 'living-fossil communitiy' of the cyrtocrinid *Cyathidium foresti* and the deep-sea oyster *Neopycnodonte zibrowii* (Azores Archipelago). Palaeogeography, Palaeoclimatology, Palaeoecology 271, 77-83.

ZIEGLER, B. (1998). Einführung in die Paläobiologie Teil 3 - Spezielle Paläontologie: Würmer, Arthropoden, Lophophoraten, Echinodermen. Stuttgart: E. Schweizerbart'sche Verlagsbuchhandlung (Nägele u. Obermiller).

ZIEREP, J. AND BÜHLER, K. (2010). Grundzüge der Strömungslehre. Wiesbaden: Vieweg+Teubner Verlag / Springer-Verlag.

Appendix

A: ANSYS version 13 vs. version 15

B: CFD mesh comparison

C: RMS values of PIV of *Hyocrinus* sp.

D: Additional PIV measurement planes of *Hyocrinus* sp.

E: RMS values of PIV of *E. liliiformis*

F: Transient CFD results of *E. liliiformis*

G: Additional PIV measurement planes of *E. liliiformis*

A - ANSYS version 13 vs. version 15

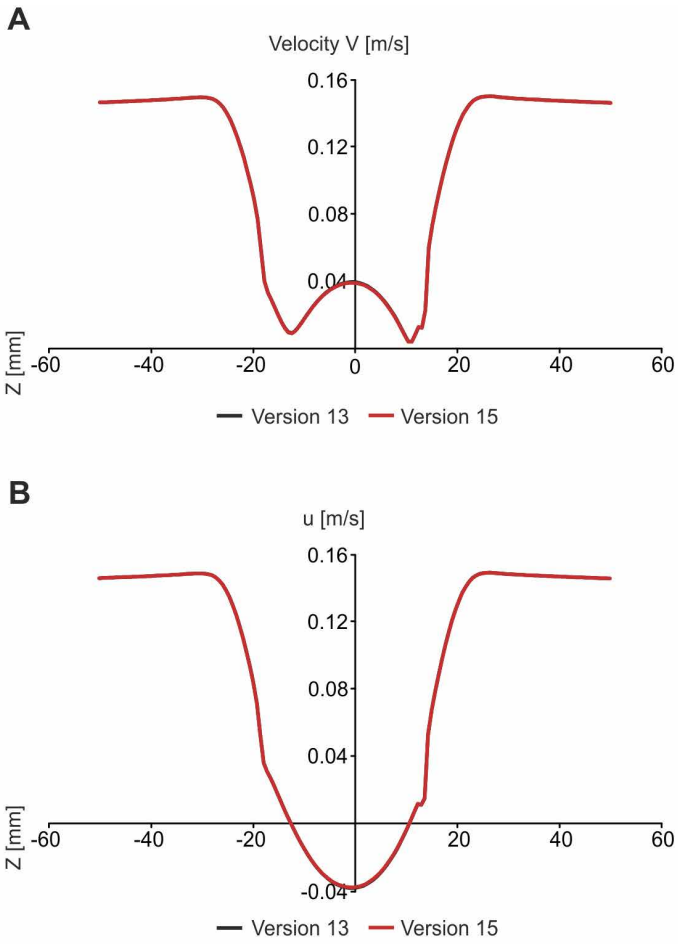

Figures illustrating the comparison of ANSYS version 13 with version 15 for *E. liliiformis* (model used for the PIV/CFD comparison) for V_{init} = 0.14 m/s, depicted as linegraph plots along Line 3 (directly behind the end of the arms). A: Total Velocity V; B: velocity component u.

B - CFD mesh comparison

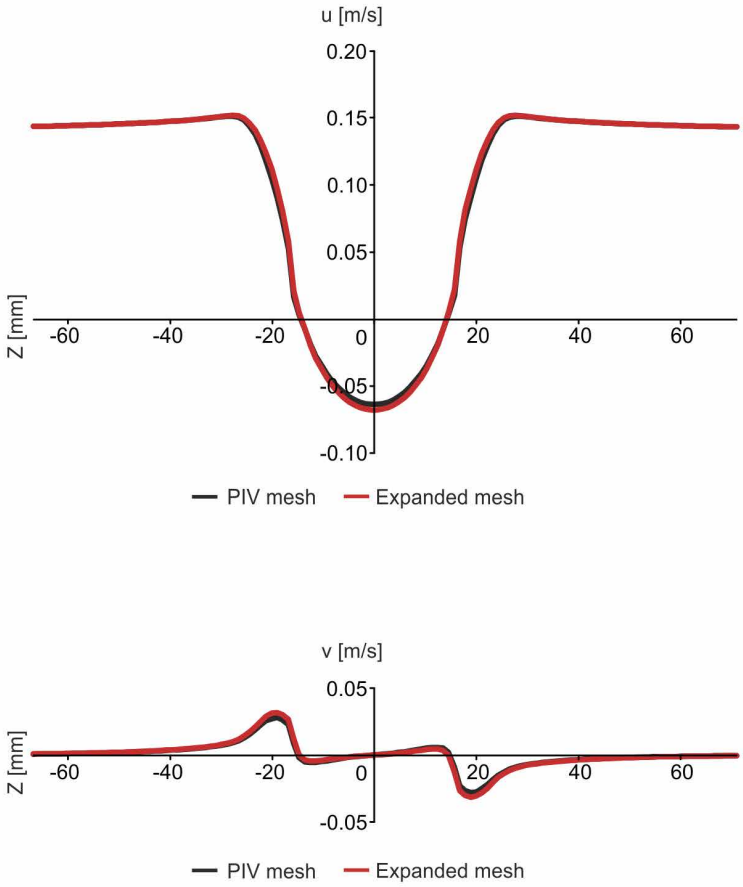

Linegraph plots of velocity of the expanded *E. liliiformis* model (10AP) with a mesh generated using the settings of the PIV/CFD comparison (black graph), and modified inflation layer settings (red graph) to illustrate the differences in results caused by the mesh modification, which makes a difference of 1.1 % in the maximum occurring recirculation velocity and thus was interpreted to be negligible.

C - RMS values of PIV of *Hyocrinus* sp.

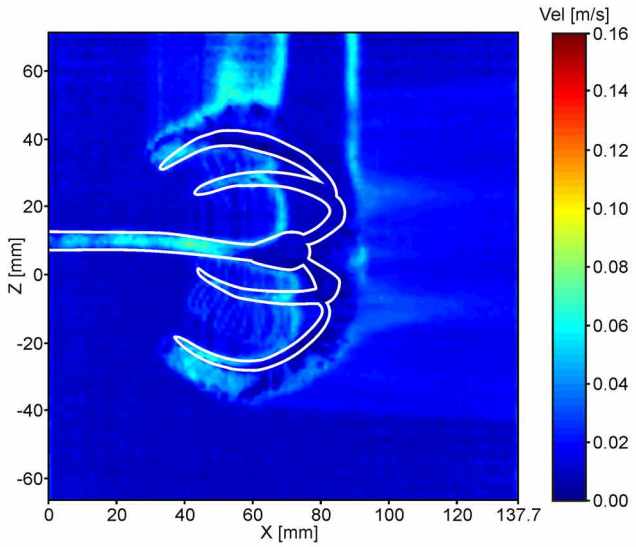

Contour plot of the RMS values of the PIV experiments of *Hyocrinus* sp. for plane Y0, illustrating the variations in flow velocities occurring over the complete measurement time for V_{init} = 0.142 m/s.

D - Additional measurement planes of PIV of *Hyocrinus* sp.

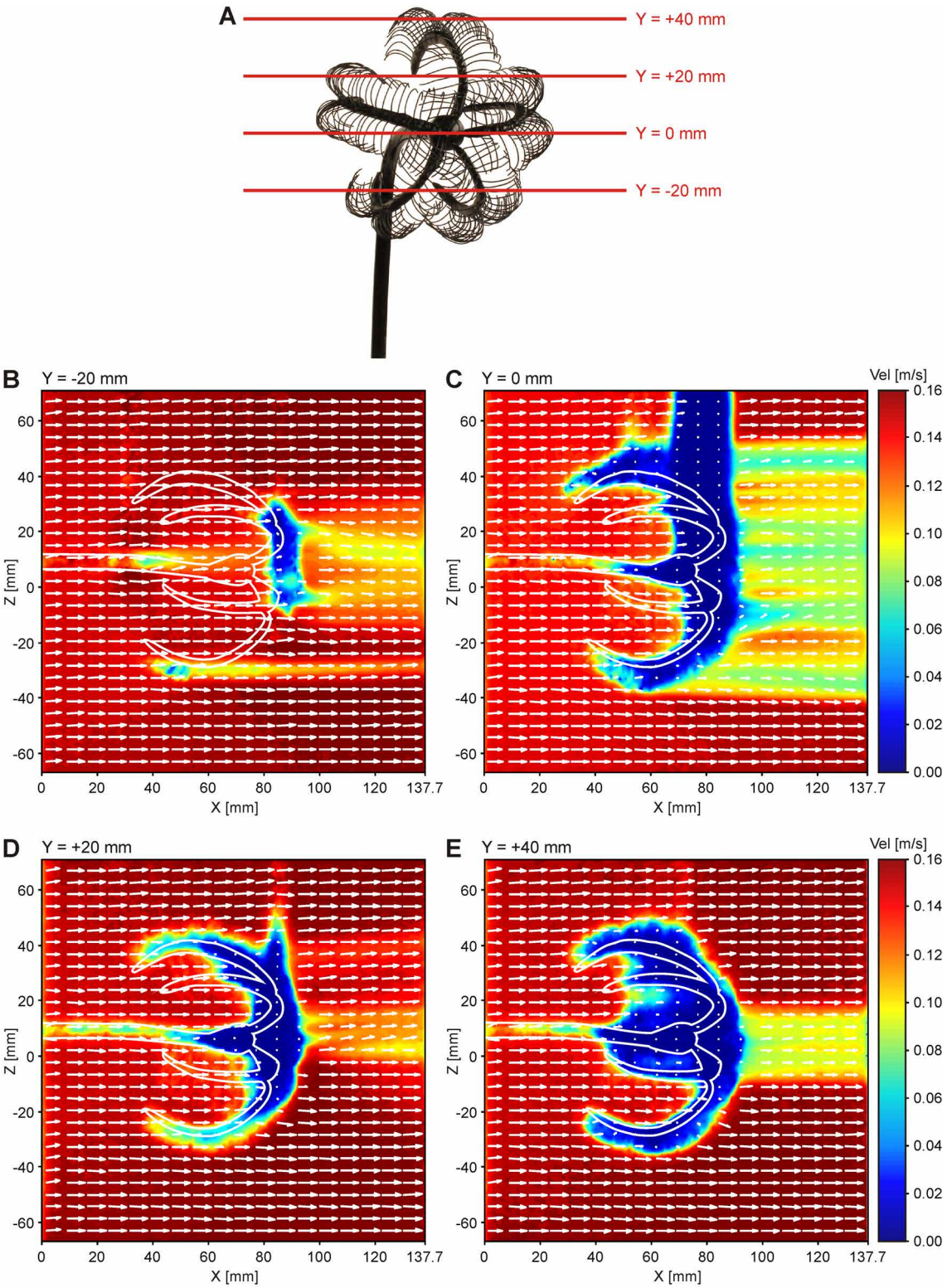

Figures presenting the flow field for *Hyocrinus* sp. for V_{init} = 0.142 m/s at the additional measurement planes of the PIV experiments, illustrated as combined contour-vector plots. A: Overview of measurement plane positions; B: results at Y = -20 mm; C: results at Y = 0 mm; D: results at Y = +20 mm; E: results at Y = +40 mm.

E - RMS values of PIV of *E. liliiformis*

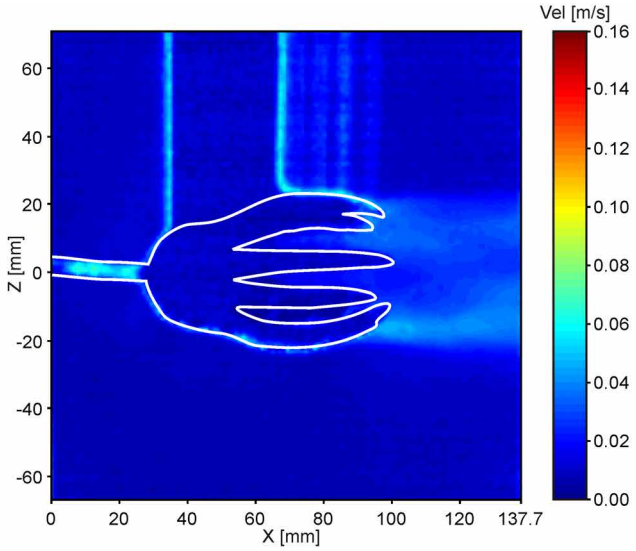

Contour plot of the RMS values of the PIV experiments of *E. liliiformis* for plane Y0, illustrating the variations in flow velocities occurring over the complete measurement time for V_{init} = 0.14 m/s.

F - Transient values of CFD of *E. liliiformis*

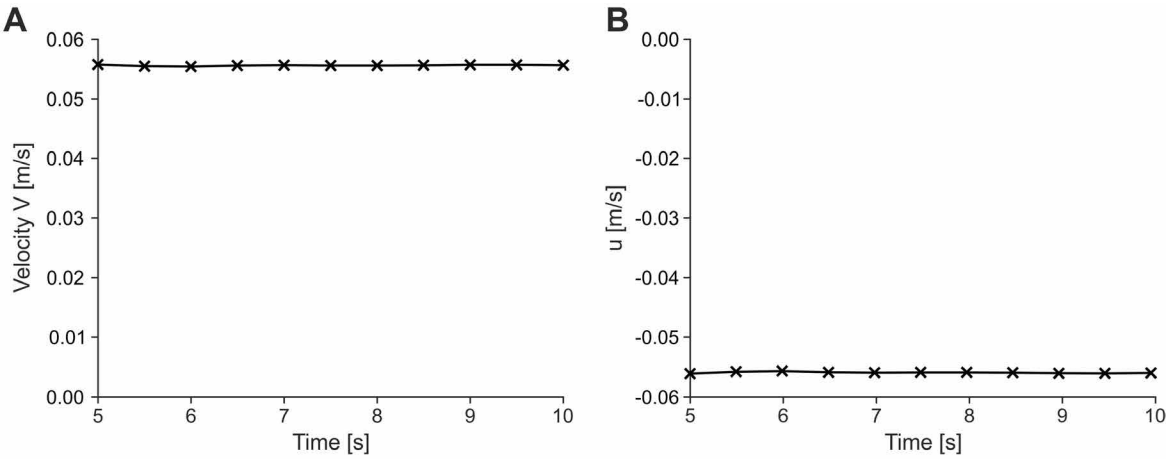

Figures illustrating transient velocity variation as linegraph plots over a time period of 5 seconds of *E. liliiformis* for V_{init} = 0.14 m/s. A: total velocity V; B: velocity component u.

Table of transient velocity variation of CFD simulations of *E. liliiformis* for V_{init} = 0.14 m/s.

Time [s]	Velocity V [m/s]	u [m/s]
5.0	0.0561	-0.0561
5.5	0.0558	-0.0558
6.0	0.0557	-0.0557
6.5	0.0559	-0.0559
7.0	0.0560	-0.0559
7.5	0.0559	-0.0559
8.0	0.0559	-0.0559
8.5	0.0560	-0.0559
9.0	0.0561	-0.0560
9.5	0.0561	-0.0560
10.0	0.0560	-0.0560

G - Additional measurement planes of PIV of *E. liliiformis*

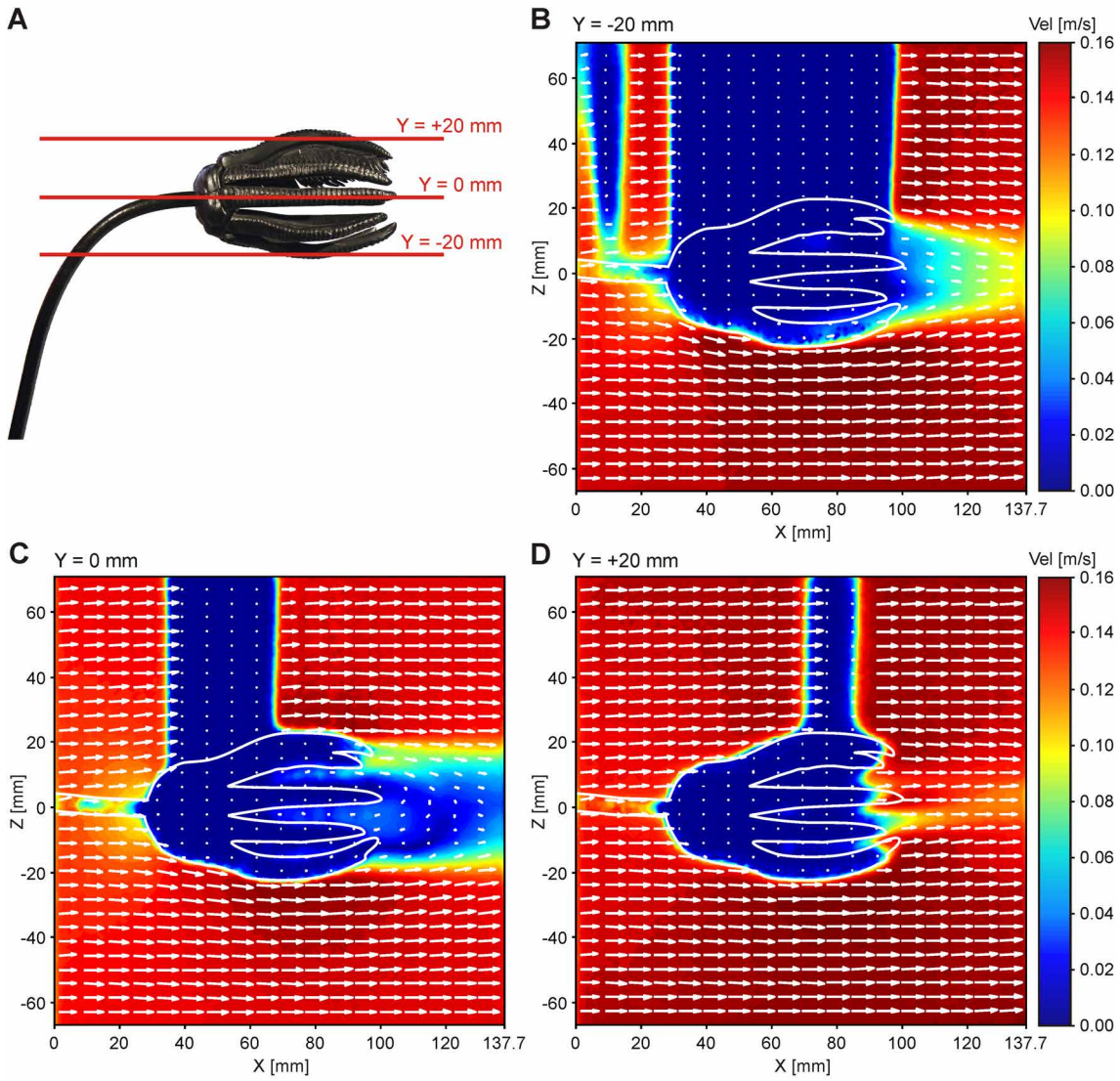

Figures presenting the flow field for *E. liliiformis* for V_{init} = 0.14 m/s at the additional measurement planes of the PIV experiments, illustrated as combined contour-vector plots. A: Overview of measurement plane positions; B: results at Y = -20 mm; C: results at Y = 0 mm; D: results at Y = +20 mm. Note: because the resin-wire model possesses flexible stalk and arms, the position of these structures shown in A does not match the exact position during PIV experiments; the purpose of Figure A is to provide an idea of the approximate locations of the measurement planes.